

Process Understanding and Weldability of Laser-Powder Bed Fusion Manufactured Alloy 718

Tahira Raza



Process Understanding and Weldability of Laser-Powder Bed Fusion Manufactured Alloy 718

Tahira Raza

University West
SE-46186 Trollhättan
Sweden
+46 52022 30 00
www.hv.se

© Tahira Raza, 2020
ISBN 978-91-88847-53-9 (Electronic version)
ISBN 978-91-88847-54-6 (Printed version)

Dedication

شروع اس پاک ذات کے نام سے جو بڑا مہربان نہایت رحم کرنے والا ہے

اے میرے رب میرا سب کچھ تیرے نام

کیونکہ---

تجھ پر ہی میرا بھروسہ ہے، تو ہی میری طاقت ہے اور تو ہی میرا علم !

Acknowledgements

I would like to express my sincere gratitude to my supervisors, Joel Andersson and Lars-Erik Svensson, for their support in my journey toward a Ph.D. Thank you Joel and Lars-Erik for always listening to me, supporting me, and encouraging me at every step of this journey.

My special thanks to Kjell Hurtig for his help in performing welding experiments and for the valuable discussions. A very special thanks to Kenneth Andersson for teaching me how to use different lab equipment and microscopes.

I would like to express my deepest appreciation to all my Ph.D. companions and colleagues at PTC who have always been there to support me. Thank you all for your generous support, help, and discussions. I would also like to extend my warmest thanks to Josefine Svenungsson, Eva Bränneby, and Victoria Sjöstedt for sharing friendship, laughter, tears, and memories with me.

I also want to acknowledge the support and industrial input from GKN Aerospace Sweden AB. A heartfelt thank you to GKN for honouring me with the GKN Aerospace Award for my research work. In addition, I am grateful for the financial support from The Swedish National Space Board and VINNOVA (National Space Research Program and National Aerospace Research Program).

I am very much thankful to Prof. Olanrewaju Ojo and his group for giving me the great opportunity to visit University of Manitoba, Canada, and accessing their facilities. It was a wonderful experience to get to know you, and I appreciate all the help and kindness I received from you. Thanks to the financial support from the corporate research school SiCoMaP for funding my visit to Canada.

Finally, I want to express my love to my wonderful family; Zaineb, Ghazanfar, Askari, Masuma, Mohsin, and Mariam, and my grandkids Hozaifah, Ibrahim, Azlaan, and Wali. You all are my life, and your unconditional love for me is my life's greatest blessing.

Tahira Raza

22nd of January 2020

Sammanfattning

Nyckelord: Laser-pulverbäddmetoden; Legering 718; Processparametrar; Värmebehandlingar; Svetsbarhet; Varmsprickor; Varestraintprovning

Den laserbaserade pulverbäddmetoden (L-PBF) är en av de vanligaste additiv tillverkningsmetoder, där komponenter byggs upp genom att smälta metallpulver med hjälp av laser. Det finns ingen universell uppsättning av parametrarna som kan användas för alla olika material och geometrier. Forskningen som här utförts beträffande processparametrar visade att lasereffekten, skanningshastighet, exponeringstid för laser och dess avstånd mellan två laser punkter var väsentliga för att minska antalet bindfel i materialet. Gasporositet var dessvärre oundvikligt då det primärt härstammar från antingen pulverframställningen eller gasinneslutning under L-PBF processen.

För att kunna utnyttja L-PBF-tekniken fullt ut som en kommersiell produktionsprocess kan sammanfogning av små L-PBF-delar för att bygga större eller mer komplexa komponenter, till exempel komponenter för jetmotorer, vara en lösning. Mikrostrukturen hos L-PBF tillverkad superlegering 718, som undersökts i detta projekt, har kristallkorn som mestadels är utsträckta i komponentens byggriktning. Kristallkornen i den tillverkade komponenten har en mycket fin cellulär till dendritisk struktur. Legeringens mikrostruktur innehåller dessutom utskiljningar som niobkarbid, titannitrid och den lågsmltande lavesfasen i de interdendritiska områdena samt långa korngränserna. Det genomfördes olika värmebehandlingar för att studera dess inverkan på varmsprickor. Varm Isostatisk Pressning (HIP), upplösningsbehandling och åldring utfördes på L-PBF-tillverkat material före svetsning för att jämföra med L-PBF-718-material utan värmebehandling samt även för att jämföra med 718 i plåtform. Resultaten visade att L-PBF-718 var känsligt för sprickbildning i HAZ under svetsning efter alla de typer av värmebehandlingar som undersöktes. Orsaken till varmsprickorna var relaterat till återuppsmältning av sekundära faser. L-PBF-718 som utsatts för HIP-behandling visade sig vara mer benägen för sprickbildning och var dessutom mindre duktil. Svetsriktningen i förhållande till riktningen för korntillväxt visade sig också ha en betydande inverkan på känsligheten för varmsprickor. Sprickor i HAZ observerades dessutom vara markant mindre i de prover som var svetsade parallellt med tillväxriktningen än i prover där svetsningen utfördes vinkelrätt mot den.

Abstract

Title: ***Process Understanding and Weldability of Laser-Powder Bed Fusion Manufactured Alloy 718***

Keywords: Laser-Powder Bed Fusion; Alloy 718; Process Parameters; Heat Treatments; Weldability; Hot Cracking; Vareststraint Testing

ISBN 978-91-88847-53-9 (Electronic version)

ISBN 978-91-88847-54-6 (Printed version)

Laser-powder bed fusion (L-PBF) is an additive manufacturing (AM) process that involves building components by fusing fine metal powders using laser. There is no universal set of process parameters that can yield optimum results for all the different materials, geometries, and L-PBF machines. The research performed at hand regarding the process parameters showed that laser power, scanning speed, laser exposure time, and laser point distance are the most influential process parameters to decrease the amount of lack of fusion. In contrast, gas porosities are unavoidable in the L-PBF material because they can occur either because of powder particles containing inherent gas pores from the powder atomisation process or entrapped shielding gas during the L-PBF process.

To fully utilise the L-PBF technique as a commercial production process, joining of small parts to build large-sized or complex shaped components, such as structural components for jet engines, can be a solution. The as-built microstructure of L-PBF-manufactured superalloy Alloy 718, which is the material in focus in the present research, has grains mostly oriented in the building direction of the part with a very fine cellular-dendritic structure within them. The microstructure of the alloy also contains NbC, TiN and low melting Laves phase in the interdendritic regions and along the grain boundaries. The specimens in this study were subjected to different heat treatments, such as hot isostatic pressing (HIP), solution heat treatment, and solution and ageing heat treatment, prior to welding, to study the effect of these heat treatments on the microstructure of the L-PBF-718 with regard to the susceptibility towards heat-affected zone (HAZ) liquation cracking during welding. Results showed that L-PBF-718 was susceptible to HAZ cracking during welding in all material conditions. L-PBF-718 subjected to HIP was more prone to HAZ cracking while welding and revealed a lower ductility behaviour in comparison to L-PBF-718 in the as-built

condition and wrought Alloy 718. The welding direction with respect to the grain growth direction in L-PBF-718 was also found to have a significant influence on hot cracking susceptibility. The extent of HAZ cracking was observed to be smaller in samples welded parallel to the elongated grain orientation than in samples where the welding was performed perpendicular to it.

Appended Publications

Paper A. A review of the effect of selective laser melting process parameters and its influence on microstructure, defects and strength in the Ni-base superalloy Alloy 718. 7th International Swedish Production Symposium Paper ID: 67, **2016**, Lund, Sweden. Authors: Tahira Raza, Joel Andersson, Lars-Erik Svensson.

As the main author, Tahira Raza, planned and wrote the literature survey. Co-authors contributed by editing the paper.

Paper B. Vareststraint weldability testing of additive manufactured alloy 718. Science and Technology of Welding and Joining, **2018**, vol. 23:7, pp. 606-611. Authors: Tahira Raza, Joel Andersson, Lars-Erik Svensson.

As the main author, Tahira Raza, performed the characterization, analyzed the results, structured and wrote the article. Co-authors contributed by planning the experiments, discussing the results and editing the article.

Paper C. Microstructure of selective laser melted Alloy 718 in as-manufactured and post heat treated condition. 8th International Swedish Production Symposium, Stockholm, Sweden. Procedia Manufacturing, **2018**, vol. 25, pp. 450-458. Authors: Tahira Raza, Joel Andersson, Lars-Erik Svensson.

As the main author, Tahira Raza, planned the experiments, performed the characterization, analyzed the results, structured and wrote the article. Co-authors contributed by discussing the results and editing the article.

Paper D. Influence of Heat Treatments on Heat Affected Zone Cracking of Gas Tungsten Arc Welded Additive Manufactured Alloy 718. Metals, 248 9, 881, **2019**. Authors: Tahira Raza, Kjell Hurtig, Gbenga Asala, Joel Andersson, Lars-Erik Svensson and Olanrewaju Akanbi Ojo.

As the main author, Tahira Raza, planned the experiments, performed the characterization, analyzed the results, structured and wrote the article. Co-authors contributed by performing the welding, discussing the results and editing the article.

Paper E. Vareststraint Testing of Selective Laser Additive Manufactured Alloy 718 - Influence of Grain Orientation. Metals, 9, 1113, **2019**. Authors: Tahira Raza, Joel Andersson, Lars-Erik Svensson.

As the main author, Tahira Raza, planned the experiments, performed the characterization, analyzed the results, structured and wrote the article. Co-authors contributed by discussing the results and editing the article.

Other publication by the author

Influence of laser exposure time and point distance on 75 μm thick layer of selective laser melted Alloy 718. International Journal of Advance manufacturing Technology, 94: 2199, 2018. Authors: Paria Karimi, Tahira Raza, Joel Andersson, Lars-Erik Svensson.

Table of Contents

Dedication	iii
Acknowledgements.....	v
Sammanfattning	vii
Abstract	viii
Appended Publications	x
Table of Contents	xii
Abbreviations/Nomenclature	xiv
1 Background.....	17
1.1 Objective and research questions	18
2 Introduction.....	19
2.1 Laser-Powder Bed Fusion (L-PBF)	19
2.1.1 Defects	22
2.2 L-PBF of Alloy 718	24
2.3 Welding and weldability testing of Alloy 718.....	28
3 Experimental methods	30
3.1 L-PBF process parameters	31
3.1.1 Process optimisation for samples with powder layer thickness of 60 µm.....	32
3.2 Manufacturing of specimen for weldability testing	34
3.3 Heat treatments	34
3.4 Bead-on-plate weld testing.....	35
3.5 Temperature distribution measurement during welding	36
3.6 Varestraint testing	37
3.6.1 Comparison between different material conditions	38
3.6.2 Comparison of grain orientation.....	38

3.7	Gleeble hot ductility testing	39
3.8	Characterisation methods	43
4	Results.....	45
4.1	Introduction	45
4.2	Effect of process parameters on defect occurrence	45
4.3	Microstructure of as-built L-PBF-718.....	47
4.4	Heat treatment of L-PBF-718	49
4.5	Hot cracking during welding of L-PBF-718	52
4.6	Gleeble hot ductility test	61
5	Discussion.....	63
5.1	Process development	63
5.2	Influence of heat treatments on L-PBF-718.....	65
5.3	Welding and weldability testing of L-PBF-718	68
6	Responses to research questions.....	75
6.1	Concluding remarks	76
7	Recommendations for future work.....	77
8	References	78

Abbreviations/Nomenclature

AM	Additive manufacturing
ASTM	American Society for Testing and Materials
BD	Building direction
BF	Bright field
BTR	Brittle temperature range
CAD	Computer aided design
CW	Continuous wave
Cr ₂₃ C ₆	Chromium carbide
DF	Dark field
DOE	Design of Experiments
DMLS	Direct metal laser sintering
DRT	Ductility recovery temperature
DS	Directionally solidified
EBM	Electron beam melting
EBS	Electron backscattered diffraction
EDS	Energy dispersive spectroscopy
FZ	Fusion zone
GA	Gas atomization
GTAW	Gas tungsten arc welding
HAZ	Heat-affected zone
HAADF	High-angle-annual dark-field
HIP	Hot isostatic pressing
IPF	Inverse pole figure
L-PBF	Laser-powder bed fusion
L-PBF-718	L-PBF-manufactured Alloy 718
MCL	Maximum crack length
mm ³	Cubic micrometer
MPa	Mega pascal
Nb	Niobium
NbC	Niobium carbide
NDT	Nil ductility temperature
NST	Nil strength temperature
PMZ	Partial melted zone
ppm	Parts per million
PREP	Plasma rotating electrode process
PW	Pulsed wave
SEM	Scanning electron microscope
SIMS	Secondary-ion mass spectrometry
SHT	Solution heat treatment
SHT+AGE	Solution heat treatment followed by ageing heat treatment
SLM	Selective laser melting

STL	STereoLithography
TiC	Titanium carbide
TiN	Titanium nitride
T _L	Liquidus temperature
T _P	Peak temperature
TCL	Total crack length
TEM	Transmission electron microscopy
TWI	The Welding Institute Ltd
UTS	Ultimate tensile strength
W	Watt
WD	Welding direction
Wt.%	Weight percent
YS	Yield strength
3D	Three dimensional
μm	Micrometer
μs	Microsecond
γ'	Gamma prime (Ni ₃ (Al, Ti)
γ''	Gamma double prime (Ni ₃ Nb)
δ-phase	Delta phase (Ni ₃ Nb)

1 Background

Additive manufacturing (AM) is a process of joining materials to fabricate physical objects from 3D model data, usually layer upon layer, in contrast to subtractive (e.g. milling) and formative (e.g. forging) manufacturing technologies [1]. This definition is generally applicable to all classes of materials including polymers, composites, ceramics, and metals [1]. Several AM techniques are utilised for processing metal, among which direct energy deposition (DED) and powder-bed fusion (PBF) technologies are most common. These technologies differ with respect of feed stock material, energy source, and processing method [2]. In DED technologies, the added material (wire or powder) is directly fed into the substrate's melt pool. A focused heat source (laser, electron beam or plasma arc) melts the material being deposited [2, 3]. In PBF technologies, layers of powder are applied on the baseplate, and a heat source (electron beam or laser) melts the applied powder. The baseplate then moves downwards, and a new powder layer is applied. The process continues until the part being built is completed. Materials such as stainless steel, tool steel, aluminium alloys, titanium and its alloys, and nickel-based alloys can be manufactured using PBF technologies. It is this latter technology that is the subject of this thesis.

AM in general and PBF techniques in particular are the topic of increasing interest to researchers and industries nowadays. An example is the ongoing research at GKN Aerospace to upgrade the Vulcain 2.1 engine for Ariane 6 to reduce the cost and to improve the architecture of the turbine by utilising PBF technologies [4]. However, the components of interest in this work are the hot structures of jet engines where Alloy 718 is one of the main superalloys that are used today. Alloy 718 is an iron-nickel-based superalloy widely used in high temperature applications for aircraft and land-based gas turbine engines.

Within PBF, electron beam melting (EBM) and laser-powder bed fusion (L-PBF) are commonly used techniques for metal AM [5]. Other terms for L-PBF processes used by machine manufacturers are selective laser melting (SLM), laser sintering and direct metal laser sintering (DMLS) [2]. Like all AM methods, L-PBF was also developed because of the need to produce near-net-shape and full-dense objects with mechanical properties equivalent to objects manufactured by conventional methods and to avoid post processing of the built part [6]. However,

L-PBF is not an entirely problem-free process, and high amount of residual stresses, cracking, porosities and lack of fusion defects are commonly encountered [7]. Because of these defects, application of different post heat treatments becomes mandatory and is recommended by ASTM [8]. Another issue with the L-PBF process is the lower production rate than conventional methods. Therefore, L-PBF is mainly suitable for manufacturing customer specific parts with complex geometries and for repair of worn out parts. Additionally, the quality of the final part is highly dependent on the process parameters, and there is no universal set of parameters that can yield optimum results for all the different materials, geometries, and L-PBF machines. Therefore, it is important to investigate the influence of different process parameters on the specific material and part geometry.

Another important aspect of L-PBF-manufactured parts is that the size of the L-PBF-manufactured objects is often quite limited because of the nature of the process and size of the production chamber. To fully utilise the L-PBF process as a commercial production process, joining of small parts to build larger-sized or complex shaped components, such as structural components for jet engines, is an issue. Because welding is the main joining technique for metallic materials, the behaviour of L-PBF-manufactured materials during welding is an important concern that needs to be studied.

L-PBF manufacturing of metallic materials and welding share many resemblances in their physical processes and the appearance of the microstructure [9]. This is also true for L-PBF-manufactured Alloy 718 (abbreviated as L-PBF-718), whose microstructure is similar to the fusion zone (FZ) of welded materials with grains mostly oriented in the building direction of the part and having a very fine cellular-dendritic structure within them [10]. The microstructure of the alloy also contains NbC carbides, TiN nitrides, and low melting Laves phase in the interdendritic regions and along the grain boundaries. It has been known for a long time that the presence of NbC and the Laves phase in Alloy 718 can contribute to hot cracking in the HAZ during welding [11-13].

1.1 Objective and research questions

The overall microstructure of a material, including existing phases, their morphology, and distribution, is directly related to the manufacturing process and subsequent post-processing treatments. Usually, Alloy 718 is used in either the cast or wrought form followed by post-processing heat treatments to generate a

suitable microstructure for specific uses. Earlier studies concerning the weldability of Alloy 718 in cast and wrought forms showed that the extent of HAZ liquation cracking can be influenced by the pre-weld heat treatment. Thus, the objective was to study the effect of different heat treatments on the microstructure of the L-PBF-718 with respect to the susceptibility toward HAZ liquation cracking during welding.

To utilise L-PBF as a production process in industry, an increased understanding of how the L-PBF process parameters and post-process heat treatments influence the material characteristics is important. As mentioned before, because of the limited size of the L-PBF-manufactured parts, it is important to understand how L-PBF-718 behaves in welding. The main objective of this thesis is to address the following three research questions:

What types of defects appear in L-PBF-manufactured parts and how are they affected by specific process parameters?

What is the influence of post-process heat treatments on the L-PBF-718 microstructure?

What is the susceptibility towards cracking in L-PBF-718 during welding?

2 Introduction

In this thesis, L-PBF was used as the production method. In the following subchapters, the L-PBF process will be described along with its associated process-induced defects and L-PBF-manufacturing of Alloy 718. Furthermore, a general background of welding and weldability testing of Alloy 718 is presented.

2.1 Laser-Powder Bed Fusion (L-PBF)

L-PBF was developed by Dr. M. Fockele and Dr. D. Schwarze of F & S Stereolithographie-technik GmbH, together with Dr. W. Meiners, Dr. K. Wissenbach, and Dr. G. Andres of Fraunhofer ILT. The aim was to produce metal components from metallic powders. In 1997, the patent for the technology was first submitted to the German Patent and Trademark Office and was published in 1998 [14].

In this technique, the powder particles are melted by a laser and fused together to build a part. Melting is performed according to computer aided design (CAD) data, and thus, only selected parts of the powder layer are melted, forming the manufactured part. The process takes place in a protective gas environment inside a chamber to prevent undesirable reactions and oxidation. After completion of the build-up part, it is separated from the baseplate.

The L-PBF process chain contains a series of steps from CAD data preparation to removal of the manufactured part from the substrate. Before the CAD data are uploaded to the L-PBF machine for production of parts, STereoLithography (STL) files have to be processed by a software, such as MAGICS [2], to add support structures for any overhanging features in the part and to generate slice data for laser scanning of individual layers. The building chamber is filled with a shielding gas, such as argon or nitrogen, to prevent oxidation of the metal during fusion. The building process begins with spreading of a thin layer (usually between 20 and 60 μm) of metal powder on a baseplate. Then, a laser scans the powder to melt and fuse selected areas according to the CAD data. Once the laser scanning is completed, the baseplate is lowered, the next layer of powder is distributed on top of the solidified material and the laser scans this new layer. This process is repeated for successive layers of powder until the part is completely built. Once the laser scanning process is completed, loose powders are removed from the building chamber, and the part can be separated from the baseplate by conventional machining, sawing, or electrode discharge machining.

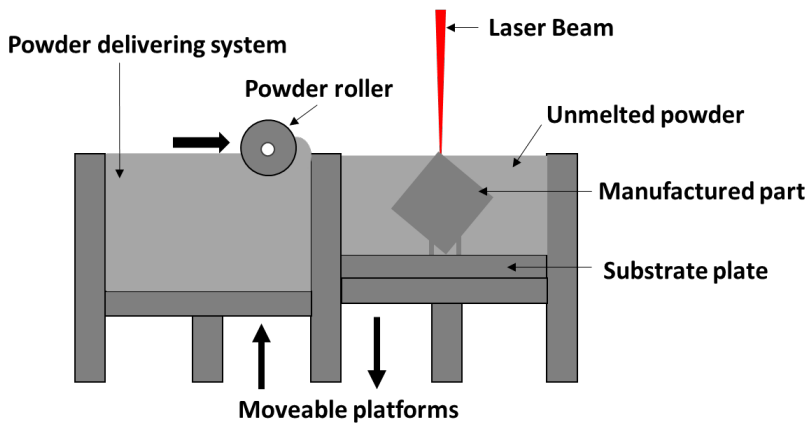


Figure 1. Schematic diagram of the L-PBF process.

Selecting the appropriate process parameters in the L-PBF process is essential for production of satisfactory parts. The response to process parameters can be seen in either the geometry or the mechanical properties of the part produced [15]. Although the L-PBF process has been used for about two decades, optimisation of the process parameters for a specific material and deposition equipment is still achieved by trial and error. Some important factors influencing the quality of the parts produced by the L-PBF technique are discussed below.

The final quality of the L-PBF-manufactured part is significantly influenced by the characteristics of the powder. Powder particle shape, size distribution, surface morphology, flowability, and chemical composition are the most important characteristics [16-19]. Chemical composition can be an issue in the case of recycled powder in which powder properties may change because of repeated exposure in a build chamber environment [16]. Spherical or near to spherical powder shape is one of the main requirements for usage of metal powder in PBF techniques. Some powder production processes allow the production of a spherical powder shape, such as plasma rotating electrode process (PREP) and gas atomisation (GA) [20]. Powders produced by PREP have a more spherical shape, a higher density, and less satellites. However, because of the limitations in the production process, relatively coarse particle size (50-150 μm), and low productivity, the production cost is high [20]. Powders produced by GA usually have a mean particle size in the range of 10-300 μm , and they may contain small amounts of atomising gas within the particles that can cause gas porosity in the final produced parts [20]. Furthermore, the surfaces of bigger size GA powder particles have “satellites” (Figure 2a) of finer particles that can aggravate the spreading of powder during the L-PBF process [20]. Nevertheless, generally, GA powders are used in L-PBF because of the lower powder production cost and a particle size distribution that is preferred for this process. To maintain the surface finish quality in the L-PBF process, the powder size distributions should fall into the range of 10-45 μm . The maximum size of the particles should not exceed the thickness of the distributed powder layer thickness because particles with sizes more than the defined layer thickness will be thrown off [21].

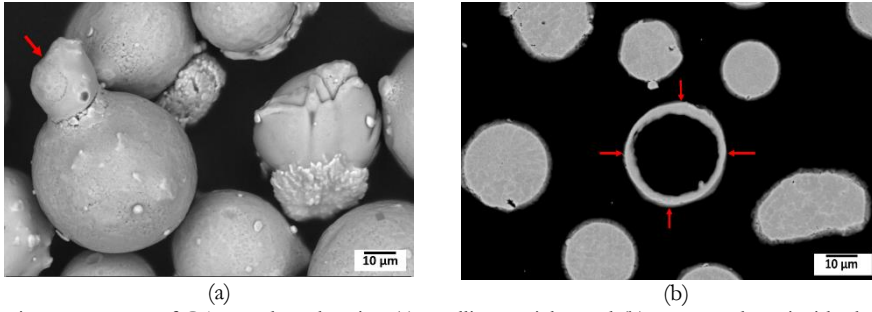


Figure 2. Image of GA powders showing (a) satellite particles and (b) entrapped gas inside the powder particle from the powder atomisation process.

2.1.1 Defects

Lack of fusion and porosity are common defects in L-PBF-manufactured parts. Lack of fusion is associated with issues such as powder packing density or the spaces in between powder particles that occurs during the spreading of layers. Insufficient heat input to the material and inadequate melting results in poorly fused layers. These regions may contain unfused or partially fused powder particles inside them. Previous studies have shown that lack of fusion can worsen the fatigue performance [15], and cracks during tensile loads are initiated at pre-existing voids [22] in the L-PBF-manufactured specimens. In addition, the lack of fusion voids can raise the concentration of stress under service and have greater tendency to lead to failure [19].

Spherical porosities are yet another type of defect in L-PBF-manufactured parts that can occur either because of powder particles containing inherent gas pores (Figure 2b) from the powder atomisation process [23] or entrapped shielding gas during the L-PBF process [24]. The spherical pores are less critical for the strength of the parts due to their spherical morphology and smaller size, although large amounts of gas pores can still have a negative effect on fatigue performance of the final part. Voids and pores located on the surface can hold moisture and worsen staining and corrosion [19].

Cracking in L-PBF-manufactured parts is one of the more serious defects because a small crack initiation site can result in catastrophic failure in service [25]. During the L-PBF process, the material experiences rapid melting and high cooling rates, which consequently creates a considerable temperature gradient. This creates a residual thermal stress in the manufactured part. The combination of high temperature gradient and residual stress can cause micron-sized cracks in the part.

Different types of cracks and reasons for their occurrence are described thoroughly in the literature [19, 26]. These cracks can be backfilled with the last to solidify material and are hard to detect. During service conditions, such as cyclic loading, these weak positions in the material may lead to crack propagation. This has been shown in studies regarding tensile testing of L-PBF-materials in which cracking is usually initiated from the micro cracks already found in the specimens [27, 28]. Proper process parameter selection, preheating of baseplate and substrate, and post processing by HIP treatment can reduce the cracking and bonding defects in crack sensitive materials [19]. However, HIP is only effective in closing internal cracks in the part, and the surface connected cracks remain unaffected [24]. Therefore, it is desirable to reduce the defects during L-PBF processing by controlling process parameters such as laser power, scanning speed, and layer thickness.

The part designer and, material and manufacture engineer need to consider all possible defects that can occur during production to assure that the requirements of the final part are met and to decide what level of porosity or flaw content is acceptable for the end customer.

Various processing parameters such as powder layer thickness, laser spot size, laser power, scanning speed, scanning strategy, hatch distance, and temperature of baseplate define the L-PBF process. All these process parameters have an influence on the track formation in a single layer, the interaction between the previous layer and the newly melted layer, and the finally produced part [29]. According to previous studies [19, 26, 30], the identified key parameters that ensure full melting of a given powder layer are laser power, hatch distance, and scanning speed. Hatch distance, also known as the scan spacing, is the distance between two laser scans (Figure 3). Scanning speed in pulsed laser systems comprises two parameters: laser point distance divided by laser exposure time [31]. Point distance (Figure 3) is the distance between two laser pulses, and exposure time is the duration for which the laser emits at one point. The above-mentioned parameters, together with energy absorption by the powder, affect the laser energy input available to heat up and melt the powder [2, 32, 33]. Insufficient energy, i.e., a combination of low laser power, high scanning speed, and high powder layer thickness, often results in balling [34]. This balling phenomenon can disrupt the formation of continuous melts and increase surface roughness [34]. In contrast, a high laser power and low scanning speed may result in extensive metal evaporation and collapse of the vapour cavity caused by this evaporation [35, 36]. This phenomenon can cause voids inside the solidified metal that consist of

entrapped vapor [36]. In addition, a very wide hatch distance can result in lack of fusion between two layers [37]. Hence, an appropriate combination of powder layer thickness, laser power, scanning speed, and hatch distance is vital for L-PBF processing of near-to-full density parts.

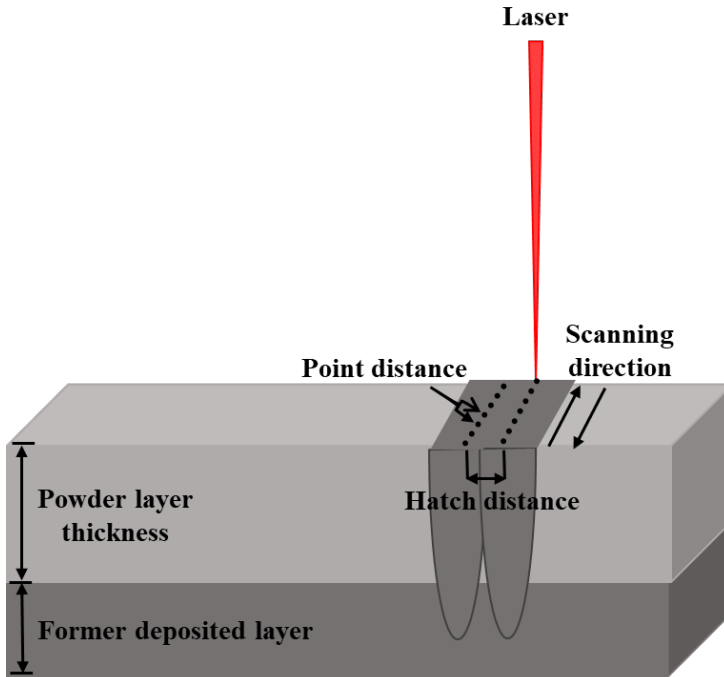


Figure 3. Schematic diagram of the L-PBF process parameters: powder layer thickness, point distance, hatch distance, and scanning direction.

2.2 L-PBF of Alloy 718

After titanium alloys and steel, nickel-based superalloys are the most studied group of metals for the L-PBF technique. Alloy 718 has been a prime focus of research regarding AM-processing of high temperature alloys because of its widespread usage within the aerospace industry [38]. In the following section, a literature review regarding L-PBF-manufacturing of Alloy 718 will be presented.

Alloy 718 is the most widely used iron-nickel-based superalloy in high temperature applications for aircraft and land-based gas turbine engines. Conventional manufacturing routes for the alloy include wrought, metal injection

moulding and powder metallurgical processing. This alloy has a Nb content of ~5wt.% and is strengthened mainly by γ'' (Ni_3Nb) and slightly by γ' ($\text{Ni}_3(\text{Al}, \text{Ti})$) phases [39]. Interdendritic segregation of Nb is very common in conventionally cast [39], welded [39], and L-PBF manufactured Alloy 718 [40, 41], which in turn results in the formation of the brittle Laves phase $[(\text{Ni}, \text{Fe}, \text{Cr})_2(\text{Nb}, \text{Mo}, \text{Ti})]$. Other phases occurring in the alloy include δ -phase (Ni_3Nb), and various metal carbides and nitrides, such as NbC, TiC, Cr_{23}C_6 , and TiN.

To reduce the high residual stresses [42], to homogenise the microstructure, and to precipitate the strengthening phases in L-PBF-718 [28], post-process stress-relieving heat treatments, solution heat treatment, and ageing are required. HIP is an additional step to heal process-induced porosities [24, 28]. These heat treatments are a combination of standard heat treatments used for cast and wrought Alloy 718 [8].

Several investigations regarding L-PBF-manufacturing of Alloy 718 have been carried out in recent years, with focus on the effect of different process parameters to achieve fully dense bulk material. Many of the studies regarding L-PBF-manufacturing of Alloy 718 focus on the process parameters for formation of a stable and continuous melt track because it is a prerequisite for producing fully dense components. Because of the different processing circumstances in each study, the results were different. It is now a well-known fact that changing one condition in the L-PBF process would change the result. Therefore, processing parameters need to be optimised with every change that occurs. L-PBF machine suppliers usually validate powder because they develop processing parameters on their machines for each specific material. So far, even with optimised process parameters for Alloy 718, the L-PBF process faces challenges regarding part quality that need to be solved. One of the main disadvantages of the L-PBF process, as described previously, is that, completely dense parts cannot be obtained by this process [24, 25].

In the L-PBF technique, there is a possibility of recycling and reuse of non-consumed powder for the next batch of production. The cost affordability of the L-PBF technique depends on the usage of the recycled powders to produce parts with consistent chemistries. It has been claimed by Ardila et al. [43] that Alloy 718 powder can be reused several times for production of parts without degradation of mechanical and metallurgical properties of the material. Strondl et al. [44] studied the effect of powder recycling on mechanical properties of L-PBF-manufactured Alloy 718 parts by producing parts with only virgin powder and

recycled blended virgin powder. They concluded that there was a porosity increase in parts because of a decrease in fine powder particles after every recycle. Furthermore, they reported that yield strength and ultimate tensile strength were comparable for parts made by both types of powder, but ductility and impact toughness values decreased when parts were produced by powders that were recycled and blended with virgin powders. Ductility was reported to be changed due to the significant oxygen pickup during the L-PBF process [44, 45].

Oxide formation in L-PBF-718 has been confirmed by several researchers [44, 46, 47], and the origin of the oxygen is reported to be the contaminated raw powder surface during powder handling and oxygen in the L-PBF chamber. It is difficult to remove the oxygen, and it easily reacts with powder to form oxides during the L-PBF process. Residual oxides from the process can have an influence on the microstructure and mechanical properties [44].

The mechanical properties associated with the various possible microstructures in cast and wrought Alloy 718 have long been established, and post-processing heat treatments have been designed for specific component and service conditions [48]. Literature regarding L-PBF-718 is largely incoherent. Despite this situation, a comparison with the performance of the L-PBF-material can be drawn in relation to currently applied industry standards.

Regarding the mechanical properties of L-PBF-718, the published literature includes tensile behaviour both for the as-built condition [27, 28, 41, 49-52], and post-processed condition [27, 28, 50, 52, 53], fatigue life behaviour [53-55] and creep performance [56, 57]. Tensile tests performed on the as-built condition by Wang et al. [27] at room temperature showed an ultimate tensile strength (UTS) of approximately 1150 MPa and a yield strength (YS) of approximately 900 MPa. In contrast, results of similar tests in the study of Aydinöz et al. [28] showed a UTS of approximately 850 MPa and a YS of approximately 600 MPa. These significant differences in results were attributed to the time-temperature path during processing. Differences in processing parameters of the L-PBF-718 cause differences in cooling rates which in turn have a pronounced impact on segregation and final properties of the part [28]. In the same study [28], the ductility of the as-built L-PBF-718 was shown to be limited and was described as a consequence of sub-micron-sized cell structures within grains, high dislocation density, and Laves phase particles. Kuo et al. [52] investigated the material in solution and ageing heat-treated condition. The samples were cut and tensile tested both parallel and perpendicular to the building direction. They reported

that tensile strengths of all the samples were comparable to wrought samples; however, the ductility of the sample tested perpendicular to the building direction was worse because of the presence of the interdendritic δ -phase present perpendicular to the stress axis. Strößner et al. [50] reported that tensile strength was better when samples were tested perpendicular to the building direction. Another study [40] regarding the influence of building direction on the mechanical properties of L-PBF-718 disclosed that the strength perpendicular to the building direction was generally higher than that parallel to the building direction, while ductility showed the opposite behaviour.

Most studies [28, 54, 55] indicate inferior fatigue performance for L-PBF-718 in comparison to wrought, and in some studies, even cast Alloy 718. This was especially more apparent for the lower stress amplitudes where the fatigue crack initiation was affected by stress concentrations caused by the presence of porosities in the L-PBF-718 [54]. Another study [53], investigating the behaviour of L-PBF-718 under strain-controlled fatigue conditions, showed that L-PBF-718 performed similar to wrought Alloy 718 under low strain amplitudes, but at high strain amplitudes, the process-induced porosity negatively influenced the material's life. They also reported a detrimental effect of HIP treatment on the strain-controlled performance of the material. It was reported that HIP caused an equiaxed grain structure with a high content of annealing twins which were attributed to the formation of fatigue cracks at numerous twin boundaries in the material [53].

Regarding the creep behaviour of as-built L-PBF-718, Kuo et al. [56] reported a short rupture duration in comparison to wrought material which was attributed to high dislocation density and interdendritic precipitates that caused inferior creep properties in L-PBF-718. Another study of the same authors [57] reported that solution and ageing heat-treated L-PBF samples failed prematurely compared to wrought Alloy 718 because of the interdendritic needle-shape δ -phase present in the L-PBF material. According to the literature [13], the needle-shape δ -phase is generally undesirable because it contributes to the inferior creep life and poor elongation in Alloy 718.

Although the L-PBF process has potential for use in the aerospace industry as a complement to the conventional processes, the process is still under observation to enhance the efficiency of the process and quality of the parts built. With careful selection of processing parameters, in combination with the use of good quality material powders, it may be possible to use L-PBF parts in the future.

2.3 Welding and weldability testing of Alloy 718

Alloy 718 was developed to overcome issues regarding strain age cracking during post weld heat treatments, which at the time, were faced in other nickel-based superalloys [58]. In contrast, the alloy suffers in terms of hot cracking during welding. These intergranular hot cracks are formed when liquid is present simultaneously with thermal contraction stresses during weld solidification. The source of the liquid in the HAZ of Alloy 718 is the constitutional liquation of NbC carbides in wrought and NbC carbides and Laves phase in cast form of the material. Additionally, the segregation of trace elements like B, P, C, or S in the grain boundaries [11, 58-60] can also cause liquation. Grain boundary segregation of these trace elements influences the formation and stability of the intergranular liquid that may be formed during the welding cycle by reducing the melting point of the grain boundary [59].

Welding of cast Alloy 718 is more difficult than the wrought material because of the inhomogeneous structure due to extensive interdendritic segregation of primarily Nb. In Alloy 718, Nb is added to promote strengthening by gamma double prime (γ'') precipitation. Segregation of Nb leads to the precipitation of Nb carbides and γ /Laves phase eutectic that resides in the interdendritic areas during solidification in processes like casting, welding, and AM [39, 41, 51, 61].

As mentioned previously, dimensions of the manufactured part in L-PBF are limited because of the size of the building chamber. To overcome this limitation, parts made by L-PBF can be joined by welding technologies such as gas tungsten arc welding or laser beam welding. In this way, L-PBF manufactured parts can be joined with other L-PBF parts as well as with conventionally manufactured semi-finished products (i.e. cast and wrought material forms) to manufacture larger-sized components. This approach can widen the use of L-PBF technology in the industry.

When it comes to welding of L-PBF-718, there are several aspects that are interesting to investigate. Some of these aspects are similar to welding of cast and wrought material and others are unique for L-PBF material. One such unique aspect of interest is the orientation of the grains and their influence on the weldability of the material. L-PBF materials have a columnar grain orientation which is mainly oriented in the building direction of the part being built. A scarce number of investigations concerning the influence of grain orientation with regard to hot cracking susceptibility have been carried out in other types of alloys

but not on Alloy 718. Lippold et al. [62] studied the liquation cracking in the partial melted zone (PMZ) of 5083 aluminium alloy plates and found that PMZ cracking was more severe in welds made transverse to the rolling direction than those made parallel to the rolling direction. The authors suggested that in the latter case, the elongated grains produced by the rolling process were parallel to the weld; thus, it was more difficult for cracks to propagate into the base metal. Sidhu et al. [63] investigated the HAZ cracking susceptibility in directionally solidified (DS) IN738 alloy, laser welded in the longitudinal and transverse directions (with regard to grain orientation). In this way, they intersected different numbers of grain boundaries in the two directions while welding. Their results showed a decrease in HAZ cracking with a reduction in the number of high angle grain boundaries that intersected the weld bead. It is known from the literature that the grain boundary energy is inherently high for high angle grain boundaries, and impurity atoms often preferentially segregate along these boundaries because of their higher energy state. Guo et al. [64] studied by Gleeble testing the correlation between grain boundary characteristics and intergranular liquation in Alloy 718 and reported that liquation mostly occurred at high angle grain boundaries when compared to low angle boundaries.

The grain size is another factor to be considered while discussing the weldability of the materials. It is a well-known fact that fine-grained materials are more resistant to HAZ liquation cracking than coarse-grained versions of the same material [65]. Grains in the L-PBF-718 in the as-built condition are elongated and located parallel to the building direction [41, 51, 66], whereas grains in wrought material are equiaxed. Furthermore, a change in grain size and morphology occurs when as-built L-PBF-718 is subjected to post-process heat treatments [24, 41, 66]. For example, HIP changes the grain morphology from elongated to equiaxed grains with a coarse grain size [24].

The microstructure of L-PBF-718 in the as-built condition contains NbC carbides and low melting Laves phase in the interdendritic regions and along the grain boundaries similar to the microstructure of the cast Alloy 718. Baeslack and Nelson [11] studied the HAZ liquation cracking in cast Alloy 718 and concluded that melting of the Laves phase in the interdendritic regions promoted liquation cracking in the HAZ. The Laves phase is formed during the terminal solidification of casting, and simply re-melts in the HAZ during welding. In contrast, NbC is decomposed during rapid heating and promotes constitutional liquation cracking in both wrought and cast Alloy 718 [12, 67]. Because of the high-volume fraction

of Laves phase present in cast Alloy 718, liquation can be extensive, resulting in increased cracking sensitivity relative to the wrought counterparts.

The overall microstructure of a material, including existing phases, their morphology, and distribution, is directly related to the manufacturing process and subsequently to the post-processing conditions. Typically, Alloy 718 is utilised in either wrought or cast conditions followed by post processing to generate the optimised microstructure for the specific use or application. Previous studies regarding the weldability of Alloy 718 in cast and wrought forms have shown that the extent of HAZ liquation cracking can be influenced by the pre-weld heat treatment. Researchers have concluded that solution heat treatment can reduce the cracking susceptibility [68] in Alloy 718 and age hardening can increase it [67]. Thus, the usual procedure within the industry is to weld the alloy in the solution-annealed condition and then subject it to solution and ageing heat treatment after welding [69]. However, in some cases, such as repair welding, the alloy needs to be welded in the aged condition [13]. Heat treatments at the appropriate temperature and time can reduce or eliminate the amount of Laves phase in the L-PBF-718 [24, 27, 41, 52, 70]. Investigating the effect of different heat treatments on weldability of the material can indicate the state in which it is possible to weld the material with less cracking.

There has been only one published study [71], to the best of authors knowledge, regarding the laser welding of L-PBF-718. The mentioned study investigated the feasibility of laser beam welding of L-PBF-718 tubes with respect to residual stresses and defects occurring during welding.

To conclude, the knowledge concerning weldability of cast and wrought Alloy 718 has been significantly developed during the last decades. However, it still remains to be studied to what extent the principals for weldability can be transferred to L-PBF-718.

3 Experimental methods

The L-PBF-718 specimens used in the current research were provided by The Welding Institute Ltd UK (TWI UK) and GKN Aerospace Filton UK. The specifications of specimens and the related experiments are presented in the Table

1. The experimental methods will be thoroughly described in the following subchapters.

Table 1. Specifications of specimens and the related experiments.

Specimen dimensions & supplier	Related experiments and papers (In brackets: related subchapter for thorough description of specimen)
Cubes 10×10×10 mm TWI UK	L-PBF Process optimisation for LT* 50 µm (see chapter 3.1; Study 1 and 2) Paper C
Cubes 10×10×10 mm TWI UK	L-PBF Process optimisation for LT 60 µm (see chapter 3.1.1; Study 3)
Plates 50×3.4×100 mm TWI UK GKN Filton	Varestraint weldability tests Machine 1 specimen, LT 60 µm (see chapter 3.7) Papers B and D Machine 2 specimen, LT 40 µm (see chapter 3.7) Paper E
Cylinders Ø7×112 mm TWI UK GKN Filton	Gleeble hot ductility tests Machine 1 specimen, LT 60 µm (see chapter 3.7) Machine 2 specimen, LT 40 µm (see chapter 3.7)

*LT = Powder layer thickness

3.1 L-PBF process parameters

To understand the effect of two controllable L-PBF process parameters (laser point distance and laser exposure time) on porosity evolution in samples, 25 cubical samples (study 1) with dimensions of $10 \times 10 \times 10 \text{ mm}^3$ were fabricated using a Renishaw AM250 machine with gas atomised (GA) Alloy 718 powder. The powder had a particle size distribution of 15 to 45 µm and was supplied by LPW Technology, UK. The composition of the Alloy 718 powder is given in Table 2. Renishaw AM250 uses a 200 W SPI Ytterbium fibre laser with a spot size diameter of 80 µm to process deposited powder feedstock within a $250 \times 250 \times 300 \text{ mm}^3$ build volume. The thickness of the deposited powder layer was set to 50 µm in this study (see **Paper C**). The fabrication was conducted in a chamber which was filled with argon gas to maintain the oxygen level below 200 ppm. The laser scanned in a pulsed mode, focused at one point for a set time period (exposure time) at a defined laser power, and then, moved to the next point. The distance between two adjacent points is defined as the point distance. The scanning strategy, used for producing the samples in the current study, was alternating with 90° in each layer (Figure 4).

Table 2. Chemical composition of the GA Alloy 718 powder in wt.%.

Element	Ni	Cr	Fe	Nb	Mo	Ti	Al	C	Mn
wt. %	Bal.	18.9	18.2	5.11	3.03	0.90	0.48	0.05	0.04
Element	Co	Si	Cu	P	B	Mg	Ca	S	
wt. %	0.08	0.04	0.02	<0.015	<0.006	< 0.01	< 0.01	< 0.01	

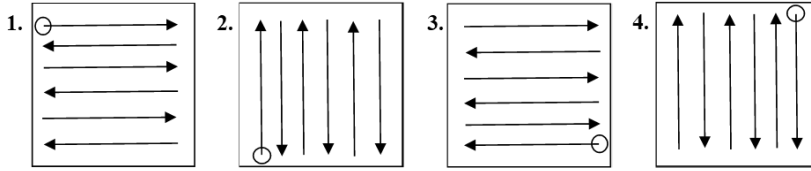


Figure 4. Schematic diagram of the alternating scanning strategy used in L-PBF-manufacturing of samples. (From **Paper C**).

During study 1, the sample manufactured with a point distance of $40\text{ }\mu\text{m}$ and an exposure time of $189\text{ }\mu\text{s}$ showed the least amount of lack of fusion defects and therefore, these two process parameters were kept constant during study 2, whereas laser power was varied. Table 3 presents the processing parameters for both studies, and Figures 1 and 3 illustrate some of the controllable process parameters.

Table 3. L-PBF process parameters used in the study.

Process parameters	Study 1	Study 2
Laser power	115 W	115 - 135 W
Hatch distance	$75\text{ }\mu\text{m}$	$75\text{ }\mu\text{m}$
Powder layer thickness	$50\text{ }\mu\text{m}$	$50\text{ }\mu\text{m}$
Point distance	$40 - 65\text{ }\mu\text{m}$	$40\text{ }\mu\text{m}$
Laser exposure time	$185 - 200\text{ }\mu\text{s}$	$189\text{ }\mu\text{s}$
Scanning strategy	Alternating with 90° (Figure 4)	

3.1.1 Process optimisation for samples with powder layer thickness of $60\text{ }\mu\text{m}$

A process optimisation task (study 3) for $60\text{ }\mu\text{m}$ powder layer thickness was performed by varying the laser power and laser exposure time to produce cubical samples (Figure 5a) with least the number of defects. All other parameters were kept constant (Table 4). Figure 5b shows the changes in defect quantity by changing process parameters. The cubes were manufactured with a Realizer SLM125 system with a build chamber of $125 \times 125 \times 180\text{ mm}^3$ and a 200WSPI

Ytterbium fibre laser with a laser beam spot diameter of 20 μm . The laser scanned in the pulsed mode. A powder with a particle size distribution of 15 to 45 μm , supplied by LPW Technology, UK, was utilised for the processing of the samples. The thickness of the deposited powder layer was set to 60 μm in this study. The fabrication was conducted in a chamber which was filled with argon gas to maintain the oxygen level below <1000 ppm.

Table 4. L-PBF process parameters used in the process optimization task.

Process parameters	Study 3
Laser power	170 - 200 W
Hatch distance	140 μm
Powder layer thickness	60 μm
Point distance	60 μm
Laser exposure time	90 – 120 μs
Scanning strategy	Alternating with 90° (Figure 4)

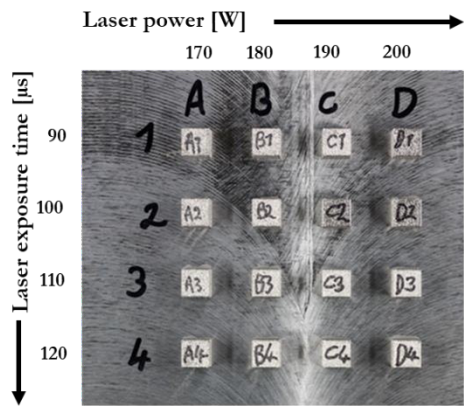


Figure 5a. Cubical samples produced by L-PBF on the baseplate.

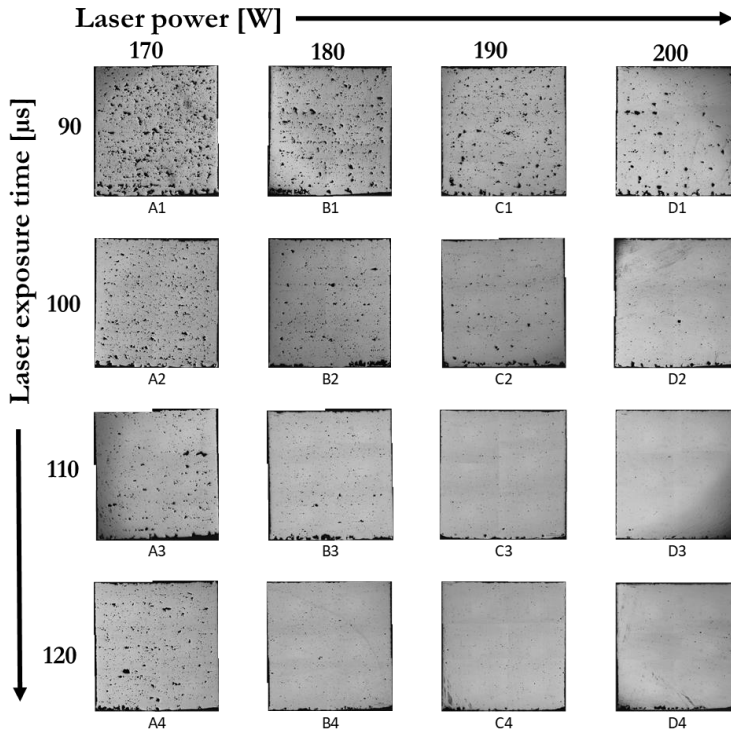


Figure 5b. OM images of cubical samples showing changes in defect quantity by changing the process parameters.

3.2 Manufacturing of specimen for weldability testing

The L-PBF-manufactured plates and cylinders for weldability tests were manufactured with a Realizer SLM125 system with optimised process parameters used for producing cube D4 (Table 3, Figures 5a and b) in the previous study. Test plates were 3.4 mm thick, 50 mm wide, and 100 mm long. Cylinders were 112 mm in length and 7 mm in diameter.

3.3 Heat treatments

To understand the effect of different heat treatments on the microstructure of L-PBF-718 and the cracking susceptibility of the material, the following heat

treatments (Table 5) were conducted on the specimen produced by Realizer SLM125 system with optimised process parameters (see Table 4 and **Paper D**).

Table 5. Heat treatments conducted on L-PBF-718.

Condition	Heat treatment / Specification
As-built	L-PBF manufactured without any heat treatment
Solution heat treatment (SHT)	954°C - 1h (AC)
Solution + Ageing heat treatment (SHT+AGE)	954°C - 1h (AC) + 760°C - 5h (FC to 649°C) + 649°C - 1h (AC)
Hot isostatic pressing (HIP)	1160°C – 105MPa – 3h (cool to 650°C in autoclave)

AC: air cooling. FC: furnace cooling

3.4 Bead-on-plate weld testing

In this study (see **Paper D**), a comparison between as-built, HIP, solution heat treatment (SHT), solution and ageing treatment (SHT+AGED), and Wrought Alloy 718 was performed. The chemical compositions of the powder and wrought Alloy 718 are presented in Table 2 and Table 6, respectively. Images of specimens produced are shown in Figure 6. Bead-on-plate welding was performed on the materials using an automatic gas tungsten arc welding (GTAW) process. Argon was used as the shielding gas, with a flow rate of 15 L/min. The welding parameters used were arc voltage of 10 V, welding current of 70 A, and welding speed of 1 mm/s. The welding parameters are based on a design of experiments (DOE) study which produced the lowest average total crack length and lowest standard deviation among different settings [72]. Five cross sections from each condition of the welded plates were excised for the measurement of the total crack length (TCL), maximum crack length (MCL), total number of cracks, and in-depth microscopic investigations. Samples from weld cross sections were mounted, ground, polished and etched. The procedure of sample preparation is described in detail in chapter 3.9. TCL was measured by first taking images of all the cracks in the cross-sections with a Hitachi TM3000 tabletop scanning electron microscope (SEM) and then by measuring the cracks with a Lumenera Infinity Analyze 6.5 software.

Table 6. Chemical composition of the wrought Alloy 718 in wt.%.

Element	Ni	Cr	Fe	Nb	Mo	Ti	Al	Mn
wt. %	Bal.	18.4	20.4	5.18	2.92	1.04	0.38	0.05
Element	Co	Si	Cu	P	B	S	C	
wt. %	0.06	0.07	0.01	0.008	0.003	0.0004	0.05	

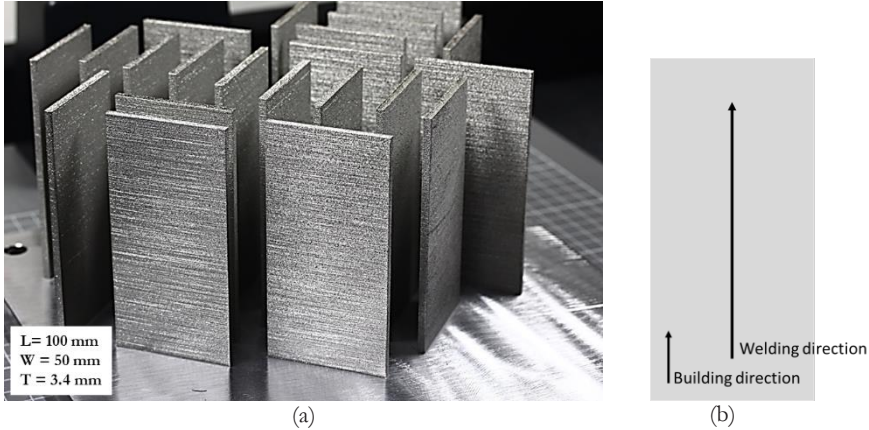


Figure 6. (a) Substrate plate with weldability test specimens after the L-PBF-process, and (b) the building direction and welding direction on the specimen.

3.5 Temperature distribution measurement during welding

The temperature distribution measurement during welding (see **Paper D**) was performed using K-type thermocouples with a 0.2 mm wire diameter. Type-K thermocouples have a measuring range from -200°C to 1250°C [73]. They have an accuracy of $\pm 0.75\%$ which translates to approximately $\pm 9.5^{\circ}\text{C}$ at 1250°C . However, the melting temperature of the thermocouple is 1300°C , which is close to the melting temperature of Alloy 718 which is $\sim 1335^{\circ}\text{C}$ [69].

The weld piece, a wrought Alloy 718 plate, had a thickness of 3.2 mm, width of 60 mm, and length of 150 mm. Thermocouples were positioned and affixed by electrical spot welding. Figure 7 shows the thermocouple locations on the test piece. The GTAW method was used for welding one bead-on-plate pass. Temperatures were measured at different distances from both sides of the weld line. To record the measured temperatures, the collected signals were transferred to a data logger and a computer. LabVIEW 2015 32 bit was used to display the thermal curves.

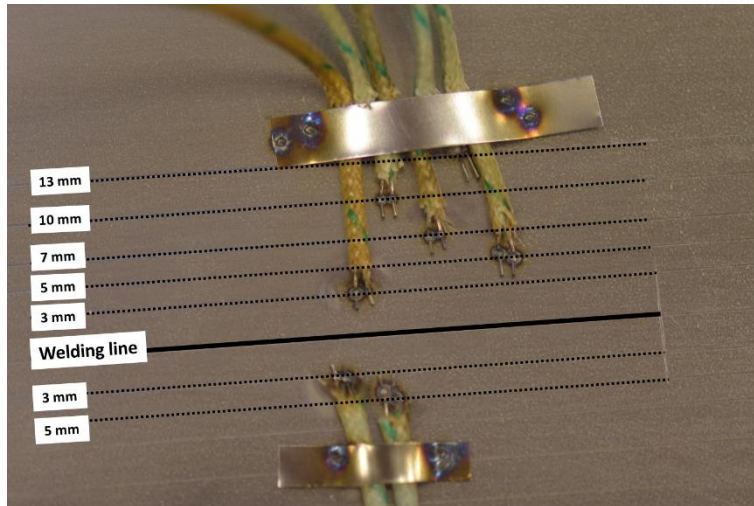


Figure 7. Position of thermocouples with respect to the distance from the weld bead. Thermocouples were spot welded on the sample at distances of 3, 5, 7, 10, and 13 mm from the weld line. (From **Paper D**).

3.6 Varestraint testing

Varestraint testing is a method of determining susceptibility to solidification and liquation cracking of the materials. The Varestraint test setup is shown in Figure 8. The Varestraint test uses a controlled, externally applied bending strain to produce cracking during actual welding of the alloy. By varying the amount of strain, a threshold strain, i.e. the applied augmented strain above which cracking occurs, and a saturated strain, i.e. the applied augmented strain level above which the crack length does not increase any further, can be determined. After testing, the total and maximum crack lengths can be measured. These crack lengths and the threshold and saturated strains are essential in determining the weldability of an alloy [72].

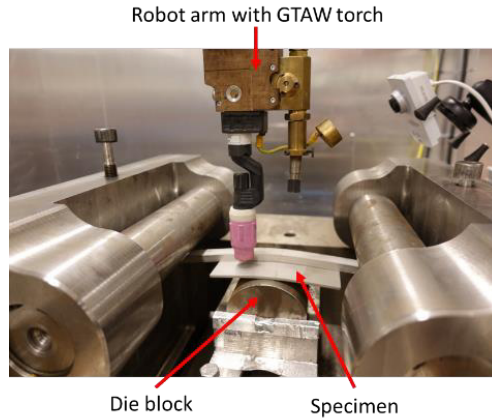


Figure 8. Vareststraint testing setup showing robot arm with GTAW torch, specimen mounted on the machine and die block.

3.6.1 Comparison between different material conditions

The Vareststraint tests were conducted using the GTAW process with an arc voltage of 10 V, welding current of 70 A, arc length of 2 mm and welding speed of 1 mm/s. The plates were bent with a stroke rate of 10 mm/s. The die mandrel radii used were 40, 60, 100, 200, and 300 mm, which led to augmented strains between 0.5 and 4%. Three repetitions were performed at each strain level for each material condition. The material used in the study were L-PBF-718 in as-built and HIPed conditions and wrought Alloy 718 (see **Paper B**).

The TCL, the length of all visible cracks in both HAZ and FZ of the welded samples, was measured using a stereomicroscope. Cracks were not easily visible because of the oxidation after welding, and therefore manual polishing (3 μ m diamond suspension) was needed, followed by electrolytic etching with oxalic acid according to standard methods. TCL was measured by following the crack path.

3.6.2 Comparison of grain orientation

The test plates manufactured by the L-PBF process were 3.4 mm thick, with dimensions 50 mm of width and 100 mm of length. Because of the proprietary rights of the process parameters, only some values can be disclosed. The samples were manufactured using a powder layer thickness of 40 μ m, a beam power of 285 W, a scan line speed of 960 mm/s, and a hatch spacing of 110 μ m. The L-PBF system used in this study used the continuous wave laser mode. The samples

were built in two different directions, vertical and horizontal (Figure 9), and were tested in the as-built condition (see **Paper E**). The plates had a rough surface and were therefore machined to approximately 3.3 mm of thickness prior to testing. The Varestraint tests and TCL measurements were conducted as described in the previous sections. Welding was performed along the growth direction of grains and perpendicular to that direction. Grain direction and welding direction are shown in Figure 9.

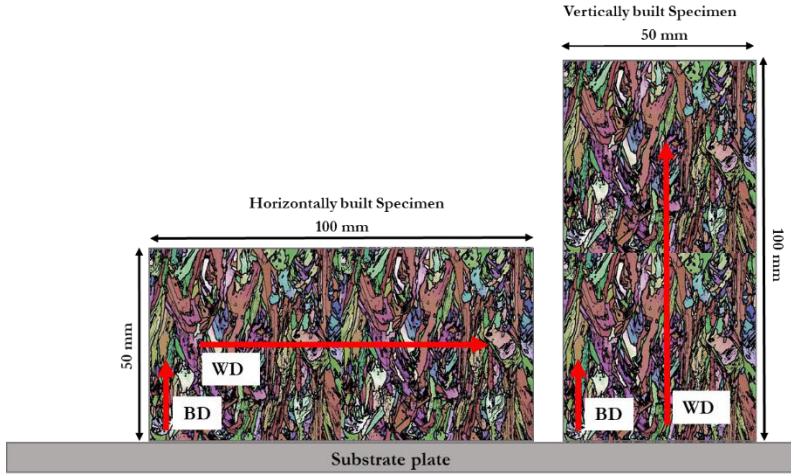


Figure 9. Schematic diagram depicting the geometry and dimensions of the test specimens. Specimen building direction (BD) is shown in relation to welding direction (WD). Grain orientation is illustrated by the EBSD image (From **Paper E**).

3.7 Gleeble hot ductility testing

A comparison between cylindrical specimens made by two different L-PBF-systems was performed by a Gleeble hot ductility test in the present study. The L-PBF-system used was Renishaw AM250 (M1) and another machine (M2). The name of the second machine supplier will not be revealed here because it is classified information; instead, it will be named machine two (M2). For M1, experimentally optimised process parameters were used (Table 4), whereas for M2, the machine supplier's optimised process parameters were used (Table 7). The total energy input for the specimens manufactured in both machines was estimated by a simplified equation, as shown below [2].

$$E = \frac{P}{v \times t \times h} \text{ J/mm}^3$$

The equation includes the major affecting process parameters, i.e. laser power (P), scanning speed (v), powder layer thickness (t), and hatch spacing (h), in a combined parameter called volumetric energy density (E) to characterise energy input during the L-PBF process. The calculated energy input was approximately 42 J/mm³ for M1 samples and 67 J/mm³ for M2 samples.

Cylindrical test specimens, 7 mm in diameter and 112 mm in length, were built perpendicular to the substrate (Figure 10a). Half of both the batches of L-PBF samples were subjected to HIP treatment (1160 °C – 105 MPa – 3 h), as per specifications in Table 5, prior to testing.

Table 7. Process parameter comparison between the two different L-PBF-machines

Process parameters	M1	M2
Laser type	Ytterbium fibre laser	
Laser spot size diameter	80 µm	75 µm
Laser mode	Pulsed wave	Continuous wave
Powder layer thickness	60 µm	40 µm
Laser power	115 W	285 W
Point distance	65 µm	-
Exposure time	200 µs	-
Scanning speed	325 mm/s	960 mm/s
Hatch spacing	140 µm	110 µm

Both batches of samples were tested in the Gleeble 3800D System with similar testing parameters. Figure 10a shows the L-PBF baseplate with specimens after the L-PBF-process, and Figure 10b illustrates the tensile test direction of the Gleeble test, which was parallel to the building direction (BD).

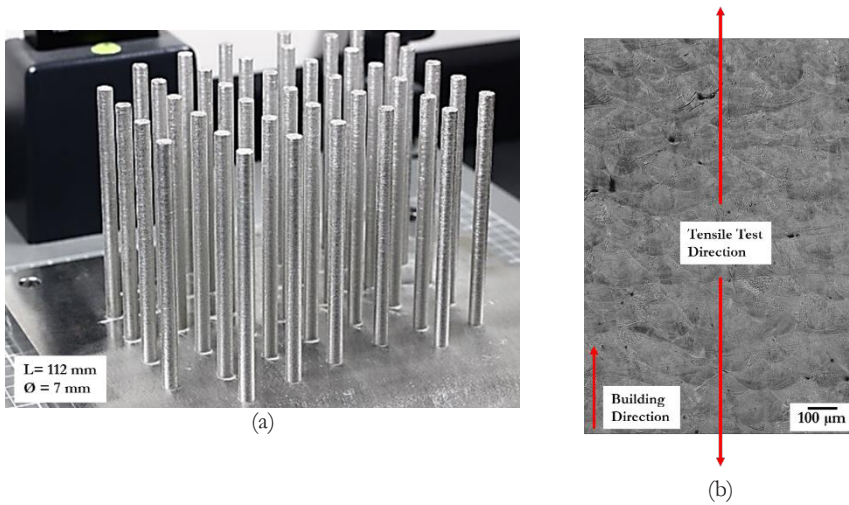


Figure 10. (a) L-PBF baseplate with specimens after the L-PBF-process, and (b) the tensile test direction in Gleeble test, which was parallel to the building direction.

Alloy 718 wrought material with a thickness of 3.2 mm was used as the reference material. The chemical composition of the material is shown in Table 8. The sheet material was in the SHT condition (954 °C – 1 h (AC)).

Table 8. Chemical composition of wrought Alloy 718 in wt. %.

Element	Ni	Cr	Fe	Nb	Mo	Ti	Mn	C
wt. %	52.18	18.29	19.75	4.98	2.88	1.02	0.11	0.05
Element	Al	Co	Si	Cu	B	P	S	Ta
wt. %	0.58	0.09	0.06	0.03	0.004	0.01	0.0002	0.01

A hot ductility test was performed using a Gleeble 3800D system. The testing parameters are given in Table 9 and are similar to those previously used by other researchers for wrought Alloy 718 [74].

The Gleeble hot ductility test is a common simulation technique to evaluate hot ductility, microstructural changes, and weld HAZ properties of alloys. The concept of the hot ductility test is to characterise the ductility of the material at elevated temperatures and relate this ductility data to cracking susceptibility. The Gleeble test setup is presented in Figure 11a. In this test, tensile samples are rapidly fractured at specific temperatures during either on-heating or on-cooling processes of a duplicated weld thermal cycle. The transverse reduction in area (RA) of the fractured sample is measured and plotted as a function of test

temperatures to represent the hot ductility “signature” of the material. This signature will exhibit several features, such as Nil strength temperature (NST), nil ductility temperature (NDT), and ductility recovery temperature (DRT), of the material tested (Figure 11b).

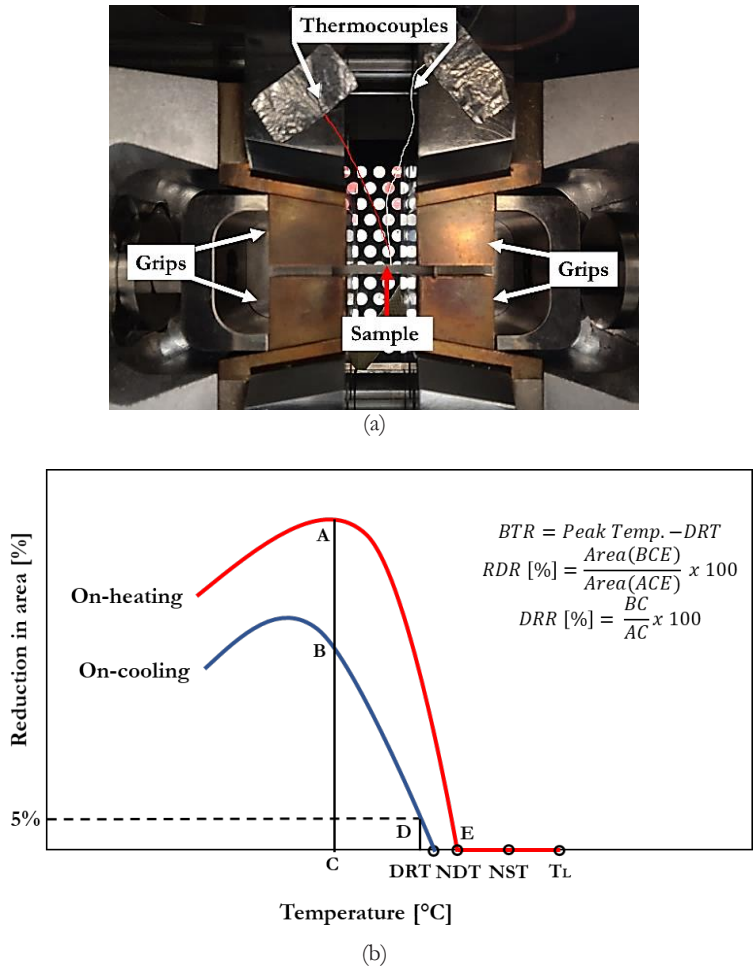


Figure 11. (a) Overview of the Gleeble test setup (b) Schematic illustration of a hot ductility signature showing on-heating and on-cooling ductility curves and different weldability parameters [13].

NDT is the point where the ductility drops to zero measured during on-heating cycle. T_L is the liquidus temperature, and NST is the nil strength temperature at which the strength of the material drops to zero. In on-cooling hot ductility

testing, the specimen is heated to a peak temperature (T_P), cooled to a test temperature, and pulled until failure. The point at which the measurable ductility is observed is termed the ductility recovery temperature (DRT) and it is normally considered at a 5% reduction in the area on-cooling. The temperature span from T_P to DRT is considered as the brittle temperature range (BTR) of the material. According to the literature [13], the BTR, also known as nil ductility range, is a range between two temperature values where hot cracking occurs in the material when a critical strain is reached. Furthermore, ductility recovery rate (DRR) is determined at a specific temperature from the on-heating and the on-cooling hot ductility curves as the ratio of RA%. Finally, the ratio of ductility recovery (RDR) is measured by taking the maximum of ductility from the on-heating curve as the reference point for this measurement. The representative areas below the on-heating and on-cooling curves are compared.

Table 9. Parameters used for Gleeble hot ductility tests.

Heating rate	111 °C/s
Cooling rate	50 °C/s
Peak temperature	1195 °C
Stroke rate	55 mm/s
Holding time at peak temperature	0.03 s
Holding time at test temperature	0.03 s
Thermocouple and diameter	K-type, NiCr-Ni, Ø 0.25 mm

3.8 Characterisation methods

Characterisation of the samples was performed as follows: sample preparation, microstructure characterisation, hardness measurements, TCL measurements, temperature distribution measurement during welding, and fracture surface measurements of hot ductility test samples.

The sectioned samples were hot mounted in a Bakelite holder. The mounted samples were then gradually ground using SiC papers up to 1200 grit. The ground samples were polished using a 0.05 μm SiC suspension to get a scratch-free surface. After polishing, the samples were electrolytically etched using oxalic acid diluted with distilled water in a 1:10 ratio. The electro-etching was performed at 3V for 1–5 s.

The TCLs in the Vareststraint tests were measured using a stereomicroscope Olympus-SZX9. Cracks were not easily visible because of the oxidation after welding, so manual polishing (3- μ m diamond suspension) was conducted, followed by electrolytic etching with oxalic acid.

The optical microscope used for light microscopy was Olympus-BX60M.

For the scanning electron microscope (SEM) examination of the material, a Zeiss SEM EVO 50 and a FEI Nova NanoSEM 450 equipped with a high-resolution field emission gun were used. To observe the precipitation hardening phases in the base metal, particularly in the SHT + AGE condition, the samples were electrolytically etched with phosphoric acid. Semi-quantitative energy dispersive spectroscopy (EDS) analyses were also performed to obtain approximate elemental compositions and concentrations. Another SEM used for sample characterization and TCL measurements was Hitachi TM3000 tabletop SEM.

Transmission electron microscopy (TEM) was performed using a FEI Talos F200X TEM equipped with a Super-X EDS system. Thin foils of the base metal for TEM study were ground, polished to a thickness of approximately 100 μ m, and punched out in 3 mm coupons before being subjected to dimpling and electro-polishing. The electro-polishing was performed using a Struers TenuPol-2 Twin-jet polisher in a solution of 10% perchloric acid and 90% methyl alcohol, at a temperature of approximately -40 °C, a voltage of 1.5V, and 1.0A DC current. A higher magnification observation of the dispersed particles was carried out with TEM. Based on high-angle-annual dark-field (HADDF) TEM and bright-field (BF) TEM imaging modes and the corresponding EDS maps, the morphology and elemental compositions of the particles could be identified.

For electron backscattered diffraction (EBSD) analysis, a Tescan GAIA3 FEG SEM with Channel 5 software from Oxford Instruments was used.

Microhardness, HV1 (9.807 N) 15 s, was measured using a Shimadzu HMV-2 microhardness test. Ten readings were recorded for each sample, and the average was determined as the hardness value.

4 Results

4.1 Introduction

The aims of the present research are as follows: to study the influence of L-PBF process parameters on building of samples and occurrence of defects; to investigate the influence of heat treatments on defects and the microstructure of L-PBF-718; and to investigate the influence of pre-weld heat treatments and grain orientation on the susceptibility toward hot cracking during welding of the material.

4.2 Effect of process parameters on defect occurrence

Manufacturing of Alloy 718 using the L-PBF process faces several challenges. One of the major challenges is the process-induced defects in the L-PBF-manufactured parts. Several types of defects were observed in the material, such as gas porosities, lack of fusion defects, and cracks initiating from the lack of fusion (Figure 12). Gas pores were spherical, whereas lack of fusion defects were large, irregular cavities usually filled with un-melted powder particles (Figure 13). Pores mainly occurred within melted beads while lack of fusion naturally was found in between two layers. In the present work, a parametric study was performed to understand the effect of laser related parameters, such as laser power, point distance, and exposure time, on the generation of defects. The results suggested that proper selection of L-PBF process parameters produces nearly to fully dense parts. However, gas porosity was unavoidable. The lack of fusion could be decreased using sufficient amount of laser power and exposure time and using the minimal distance between laser point distances. The lack of fusion defects in the samples were characterised by large cavities filled with un-melted powder which also served as crack initiation sites.

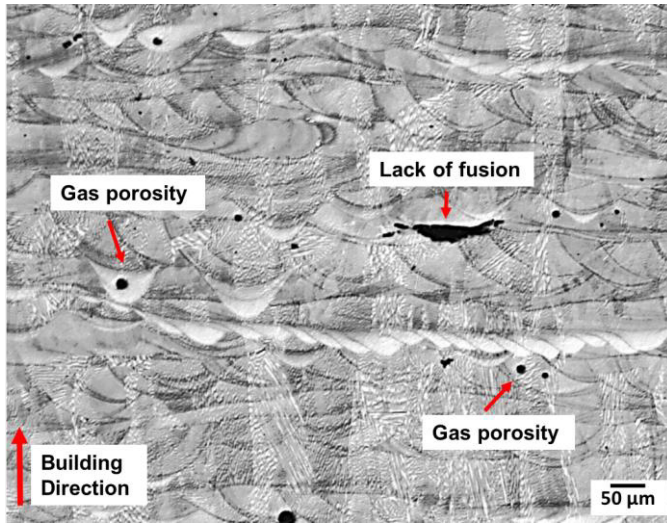


Figure 12. OM image of L-PBF as-built Alloy 718 (vertical cross section), showing building direction perpendicular to the substrate, gas porosity, and lack of fusion.

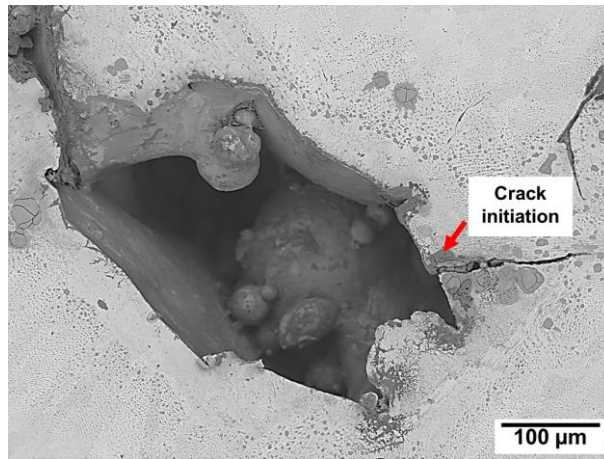


Figure 13. SEM image of lack of fusion with un-melted powder particles present (From **Paper C**).

4.3 Microstructure of as-built L-PBF-718

In the present study, the L-PBF-manufactured samples were mainly compared to wrought Alloy 718, but some comparisons with cast Alloy 718 samples were also made. The microstructure of the different manufacturing techniques were compared (Figure 14), and L-PBF-718 in the as-built condition (Figure 14a) was found to be very different from the wrought and cast forms (Figures 14b and c); however, it was somewhat more similar to the FZ of the welded Alloy 718 but on a much finer scale. The fine scale of the L-PBF microstructure was due to the rapid solidification of the molten pool during the L-PBF process.

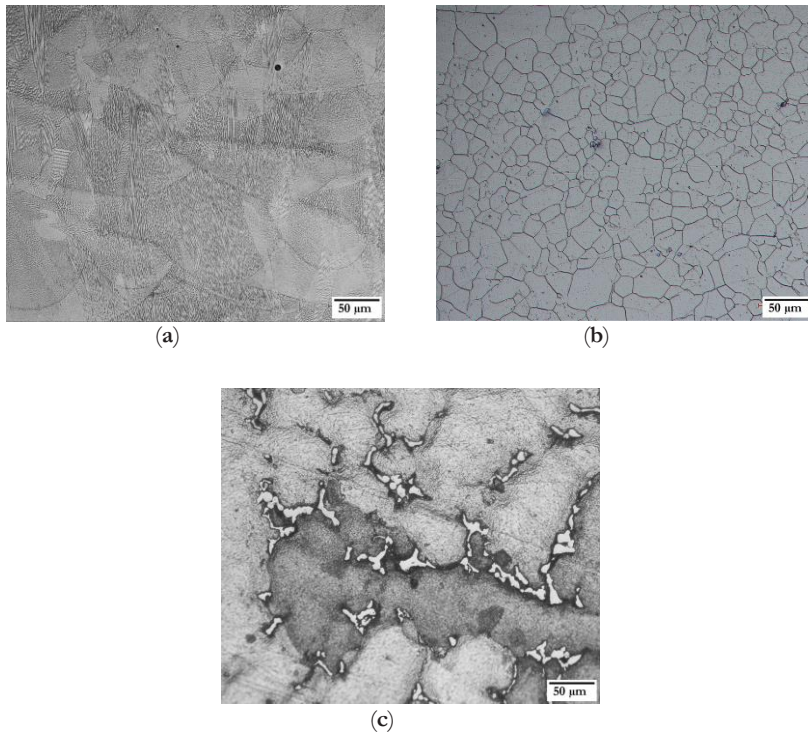


Figure 14. OM images of microstructure of (a) L-PBF as-built, (b) wrought, and (c) cast Alloy 718.

Significant segregation in the microstructure is another challenge faced during L-PBF-manufacturing of Alloy 718. The microstructure resembles the FZ of welded

Alloy 718. The grains are mostly oriented in the BD of the component having a very fine cellular-dendritic structure within them (Figures 15a and b).

EBSD mapping was used to determine the grain structure and texture of the parts. These maps reveal, inter alia, grain shape and crystallographic texture of the material. Figure 15a is an SEM image of the unetched microstructure showing grain orientation parallel to the building direction (BD). Figure 15b is an EBSD inverse pole figure (IPF) colouring mapping of the same image as that in Figure 15a. The colour key representing the crystal orientation and IPF is given on the right side of Figure 15b. The IPF colour map was plotted with respect to the Y(BD) direction. The thick black lines represent high angle grain boundaries with a $\theta > 15^\circ$ misorientation, whereas the thin black lines represent low angle grain boundaries with a 5° - 15° misorientation. The microstructure observed in the sample consisted of a columnar grain structure with a preferential grain growth in the $\langle 001 \rangle$ orientation parallel to the BD.

The microstructure of L-PBF-718 in the as-built condition contains NbC carbides and low melting Laves phase in the interdendritic regions and along the grain boundaries (Figures 15c - e). A small amount of TiN was also detected in the material.

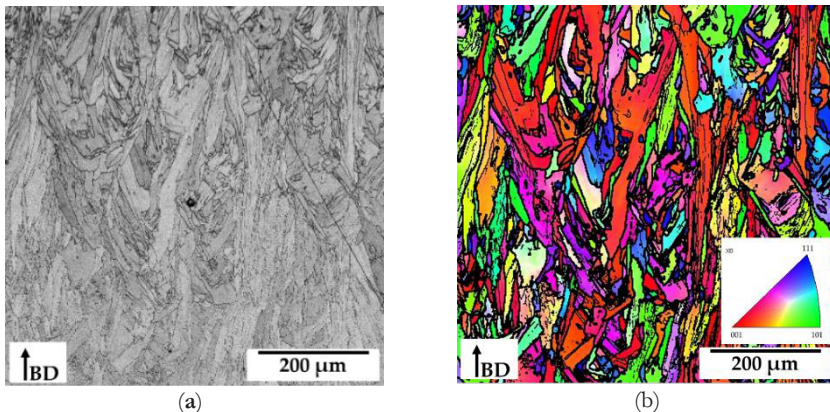


Figure 15. (a) SEM micrograph showing the unetched microstructure of the L-PBF-718. Specimen cross section parallel to the building direction is shown (From **Paper E**). (b) EBSD IPF coloured and grain boundary map of the same image as (a). The colour key representing the crystal orientation is given in the lower right corner of image b.

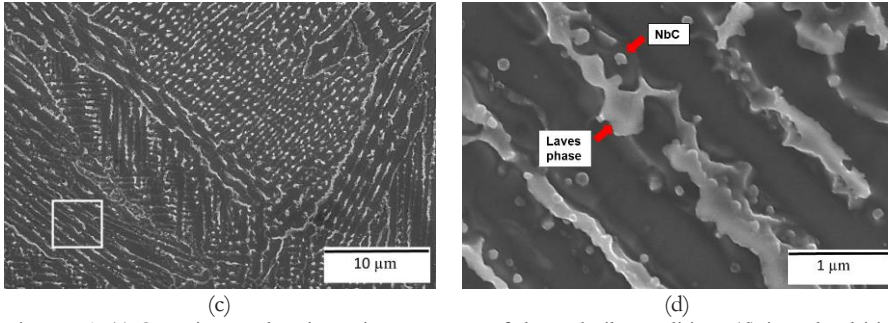


Figure 15. (c) SEM image showing microstructure of the as-built condition; (d) interdentritic regions in the as-built condition showing Laves phase and NbC carbide. (From **Paper D**).

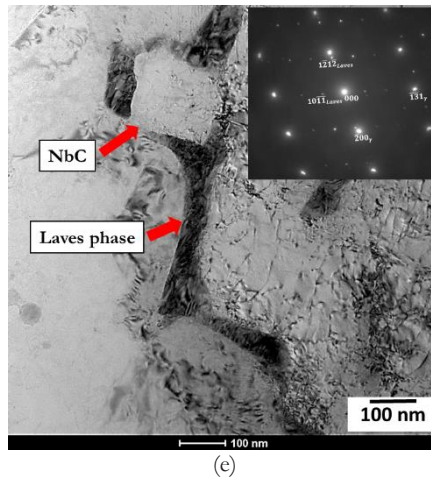


Figure 15. (e) TEM bright field image showing Laves phase and NbC carbide in interdentritic region. The inset shows the diffraction pattern of Laves phase in the γ -matrix. (From **Paper D**).

4.4 Heat treatment of L-PBF-718

In the as-built material that was subjected to SHT at 954 °C for 1 h, the cellular-dendritic structures within the grains were still present (Figure 16a), along with NbC carbides, TiN, remnants of the Laves phase, and the plate-like δ -phase (Ni_3Nb) (Figure 16b).

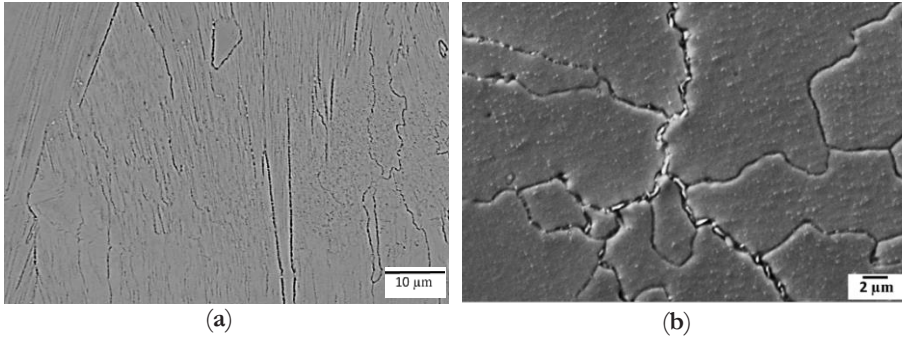


Figure 16. (a) Microstructure of SHT condition, showing (b) precipitates residing in the grain boundaries and matrix. (From **Paper D**)

After the solution heat treatment followed by a two-step ageing treatment (SHT+AGE) for 5 h at 760 °C and 1 h at 649 °C, the δ -phase, carbides, and nitrides still remained in the microstructure (Figures 17a, b, and f), along with the precipitation strengthening phases of γ' and γ'' in the matrix (Figures 17c and d). Some remnants of the Laves phase were also present in the material (Figure 17e).

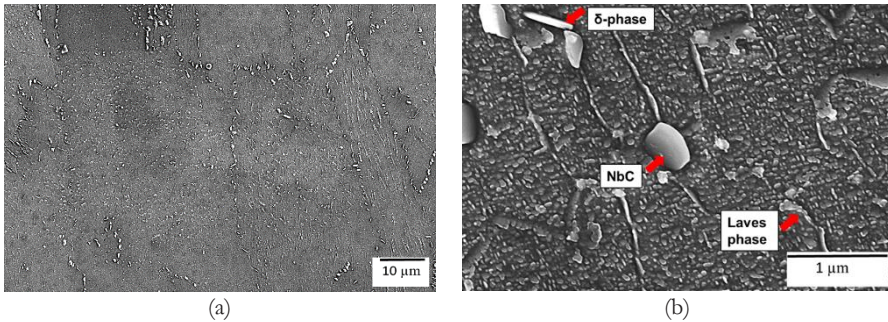


Figure 17. (a) Microstructure of the SHT + AGE samples and (b) δ -phase, NbC carbide, and Laves phase in the microstructure.

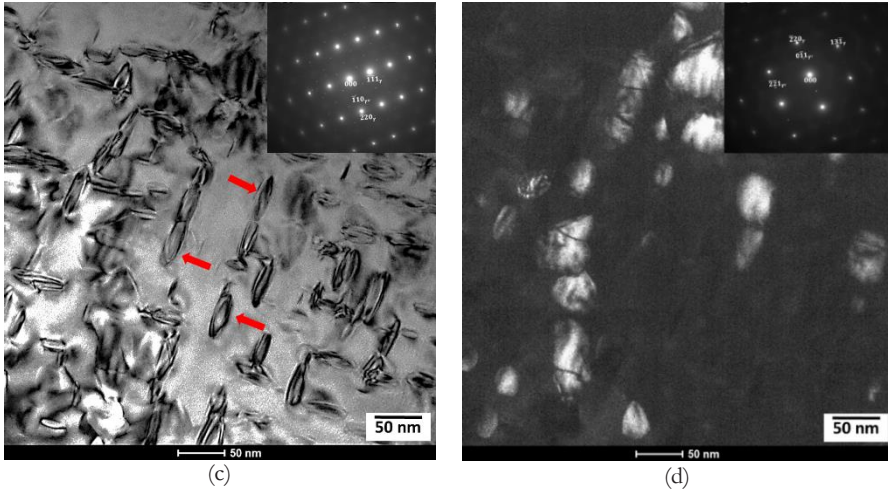


Figure 17. (c) TEM bright-field image of γ'' (marked with arrows); the inset shows the diffraction pattern of γ'' in the γ -matrix; (d) dark-field image of same area as (c), showing γ' (white particles); the inset shows the diffraction pattern of γ' in the γ -matrix.

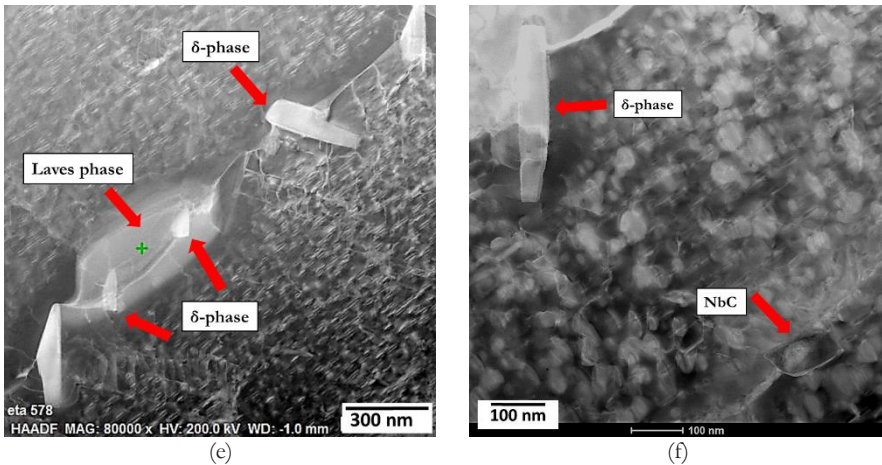


Figure 17. (e) TEM HAADF image showing the δ -phase residing on the grain boundary, Laves phase, and δ -phase forming from the Laves phase; and (f) TEM HAADF image of NbC and δ -phase residing in the grain boundary.

After HIP treatment (1160 °C at 105 MPa for 3 h) of the as-built specimens, the grains grew into a coarser and equiaxed grain structure (Figure 18a). The Laves phase was completely dissolved, but residual NbC carbides and small amounts of TiN remained in the microstructure (Figure 18b). Furthermore, notably, the HIP

treatment did not close all the porosities inherited from the L-PBF process (Figure 18a).

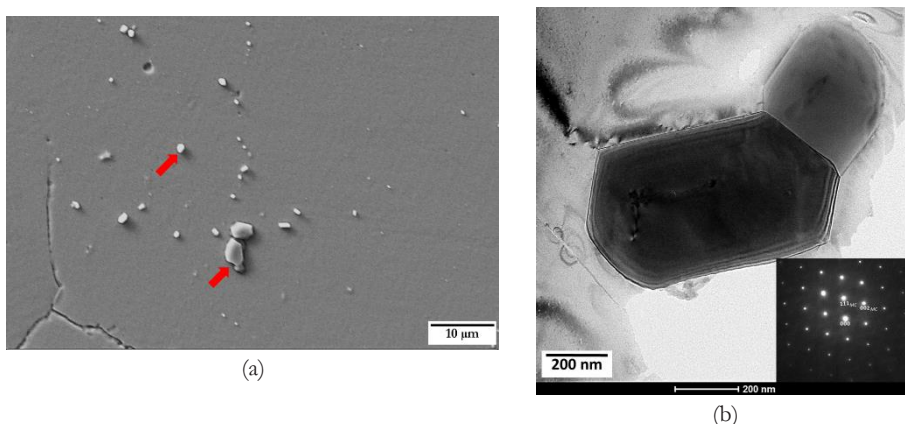
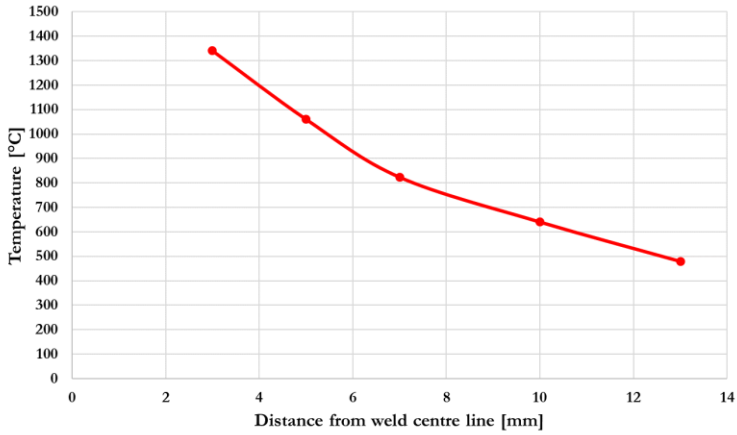
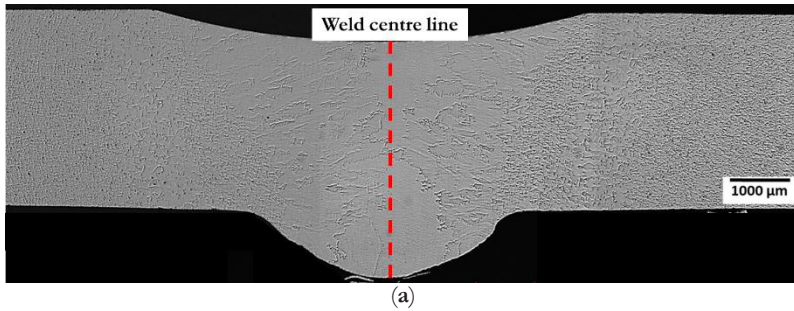


Figure 18. (a) Microstructure of HIP condition showing NbC carbides marked with arrows and (b) bright-field TEM image of carbide in HIP condition; the inset shows the diffraction pattern of carbide (From **Paper D**).

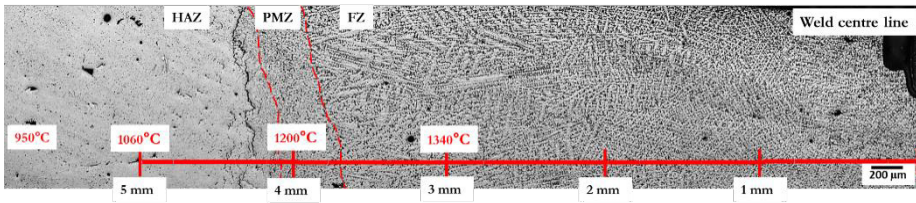
4.5 Hot cracking during welding of L-PBF-718

The susceptibility toward hot cracking during gas tungsten arc welding (GTAW) of L-PBF-718 was investigated under the aforementioned heat-treated conditions and compared with wrought Alloy 718 (see **Paper D**). Bead-on-plate experiments were conducted for the purpose. The temperature distribution in the HAZ was also measured to obtain increased insights into the type of cracking occurring in the material.

Figure 19a shows a weld cross section of the welded sample, and Figure 19b presents the peak temperatures recorded from the respective thermocouples in the material during the welding process as a function of distance from the weld centre line. Figure 19c shows the FZ, PMZ, and HAZ of the welded sample, the distance of these zones from the weld centre line, and the related peak temperatures within these zones during welding.



(b)



(c)

Figure 19. (a) Cross section of the welded sample; (b) peak temperatures as a function of distance from weld centre line; and (c) FZ, PMZ, and HAZ of the welded sample, the distance of these zones from the weld centre line and the related peak temperatures within these zones. (From **Paper D**).

After welding, the variation in TCL, MCL, and the total number of cracks in the HAZ were used as criteria for the cracking susceptibility of each material condition (Figure 20). The concept of weldability in this study was considered as the ability to resist HAZ cracking during GTAW. Results indicated that L-PBF-

718 was susceptible to HAZ cracking during welding in all material conditions. Cracks seen in the HAZ of the welded material were of two types: those with eutectic products surrounding the cracks and “clean” cracks without any apparent liquation products. Example of these two types of cracks can be seen in Figure 21. Liquation cracks were due to the liquation of secondary constituents present in the L-PBF-manufactured material. The solidification structure of the weld FZ of the material revealed γ /Laves phase eutectic and NbC carbides, as shown in Figures 22 a and b.

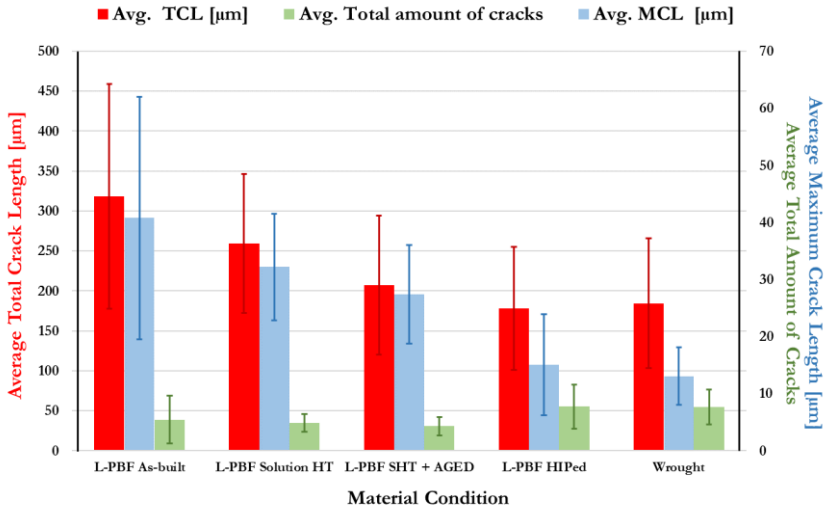


Figure 20. Graph showing HAZ cracking susceptibility of L-PBF-718 in comparison with wrought Alloy 718, presented as the average of the total crack length measurements, average of maximum crack length, and average of the total number of cracks (for five observations, with standard deviations).

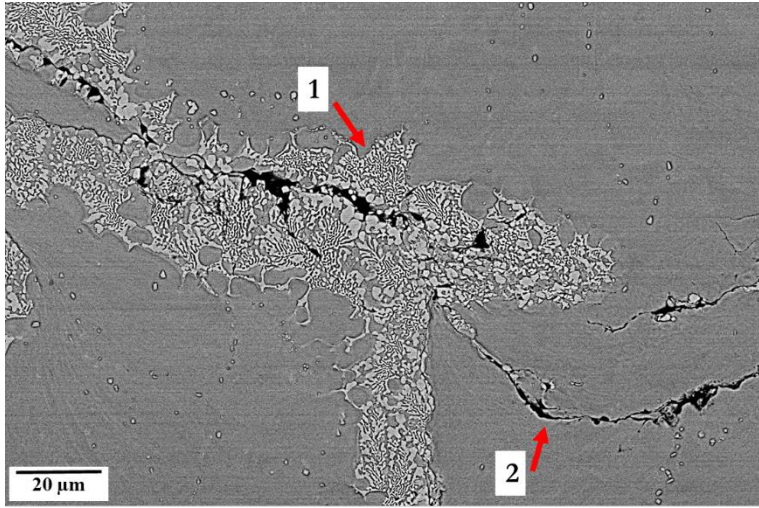


Figure 21. Example image of HAZ of a welded sample showing (1) crack surrounded by eutectics and (2) “clean” crack without any eutectic formation.

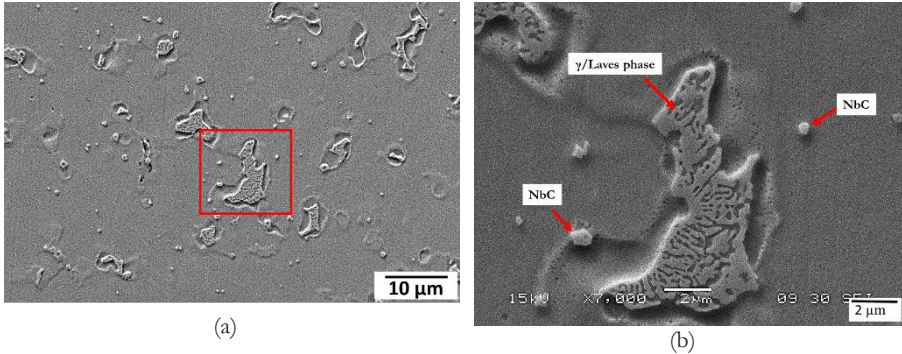


Figure 22. SEM image of (a) weld FZ with inset showing (b) NbC carbide and γ /Laves phase eutectic.

L-PBF-718, in the as-built condition, was the most susceptible to HAZ cracking. Cracking susceptibility, however, decreased in samples that had been subjected to SHT and decreased further in the SHT+AGE samples. In samples subjected to HIP directly after the L-PBF process, the cracking susceptibility was similar to that of wrought Alloy 718. However, if the standard error bars are compared, no statistically significant difference in TCL was observed between all these five conditions.

The average MCL was the highest in the L-PBF as-built condition and decreased for SHT samples. A further decrease was observed in the SHT+AGE condition. In the L-PBF-HIP condition, the MCL was similar to that of the MCL in the wrought condition. The total number of cracks was the highest in the HIP and wrought conditions because there was a higher number of smaller cracks in these two conditions.

Results of Varestraint testing (see **Paper B**) carried out on L-PBF as-built, L-PBF HIPed and wrought Alloy 718 (Figure 23) showed that the L-PBF HIPed condition had a higher susceptibility toward cracking at all strain levels. The L-PBF as-built condition showed almost the same degree of cracking as the wrought material. Furthermore, Figures 24 and 25 show that the width of the cracks in general was larger in the HIPed condition than those of the as-built condition.

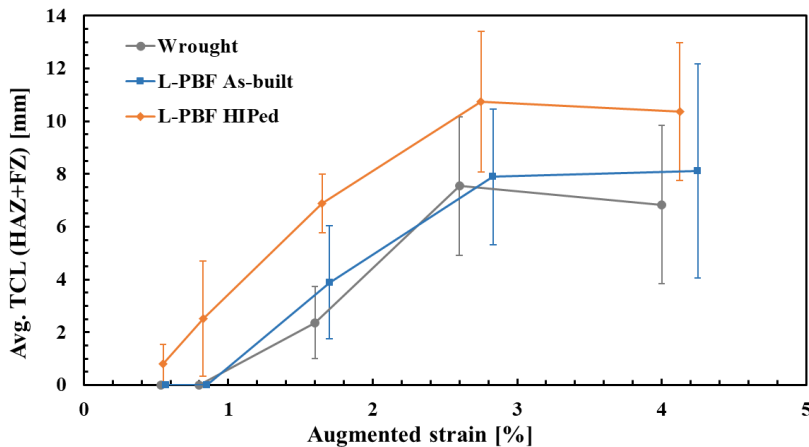


Figure 23. Graph showing the average of the total crack length (TCL) in HAZ and FZ versus augmented strain in the Varestraint tested Alloy 718 specimen. Note the significantly higher cracking susceptibility of the L-PBF-718 in the HIPed condition.

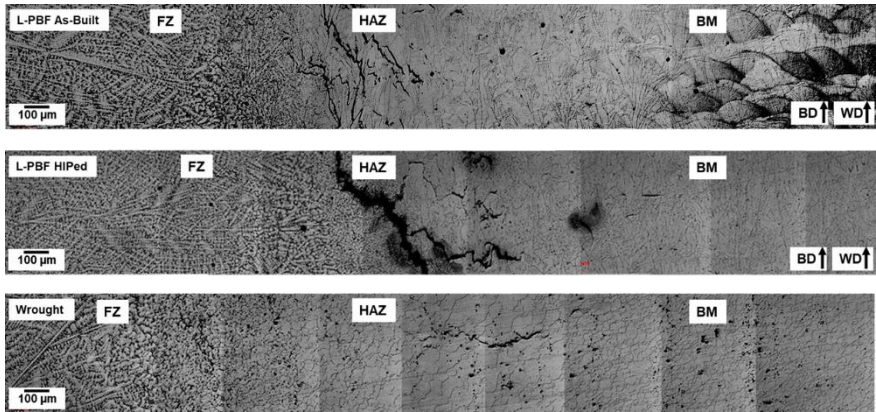


Figure 24. OM images of FZ, HAZ, and base metal microstructure of L-PBF as-built and L-PBF HIPed, showing the building direction (BD) of the samples and the welding direction (WD) during Varestraint tests (two upper images). The bottom image shows welded wrought Alloy 718.

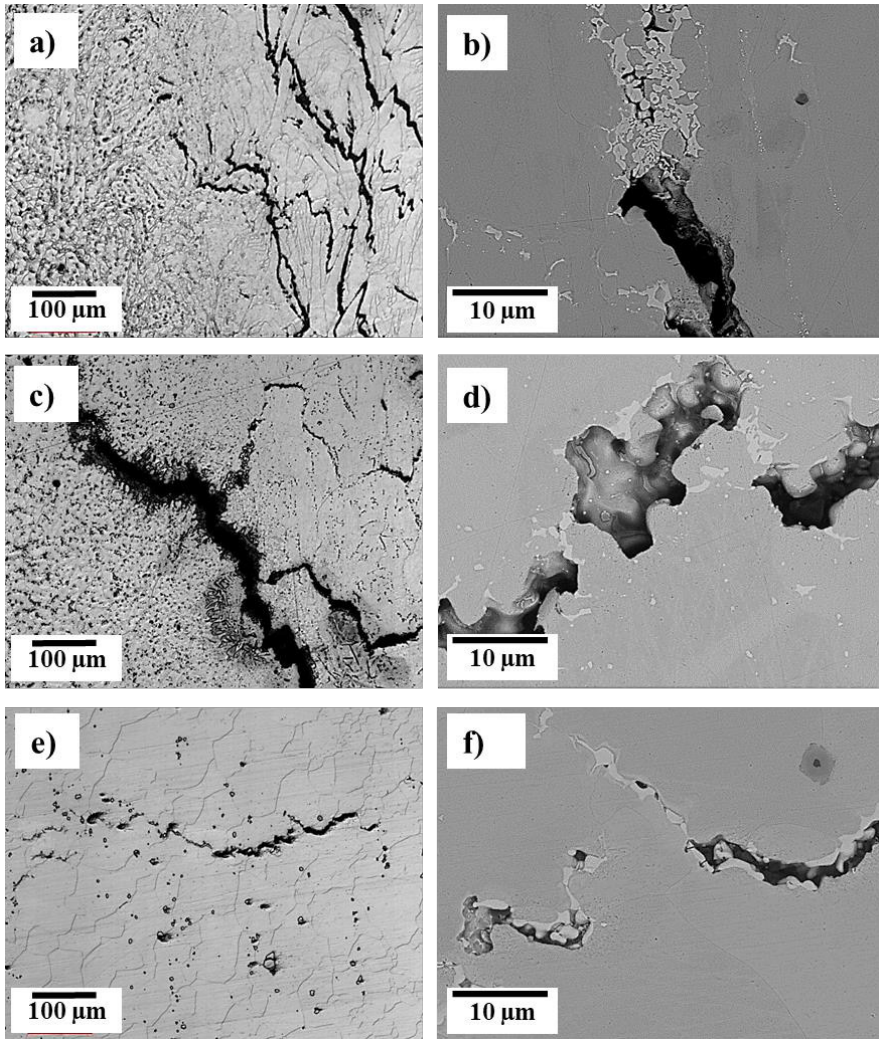


Figure 25. HAZ cracking in the Varestraint tested specimens at 4 % augmented strain; (a and b) L-PBF as-built, (c and d) L-PBF HIPed, and (e and f) wrought Alloy 718.

Welding either along the growth direction of the grains or perpendicular to that direction in L-PBF-718 also has a significant influence on the hot cracking susceptibility during the welding process (see **Paper E**). The hot cracking susceptibility of the welds was evaluated by crack measurements on each welded sample after the Varestraint test. Figure 26a shows the result of TCL measurements in both FZ and HAZ. The graph shows the average of TCL versus augmented strain of the samples welded parallel and transverse to the elongated

grain orientation. The results of the Varestraint test showed that the extent of HAZ cracking was smaller in samples tested parallel to the elongated grain orientation and larger in samples tested transverse to the elongated grain orientation (Figure 26 b). However, for solidification cracking in the FZ, no significant difference with respect to grain orientation in the base metal was found (Figure 26 c). EBSD analyses showed that cracks in HAZ of the welded samples occurred in high angle grain boundaries (Figures 27 and 28).

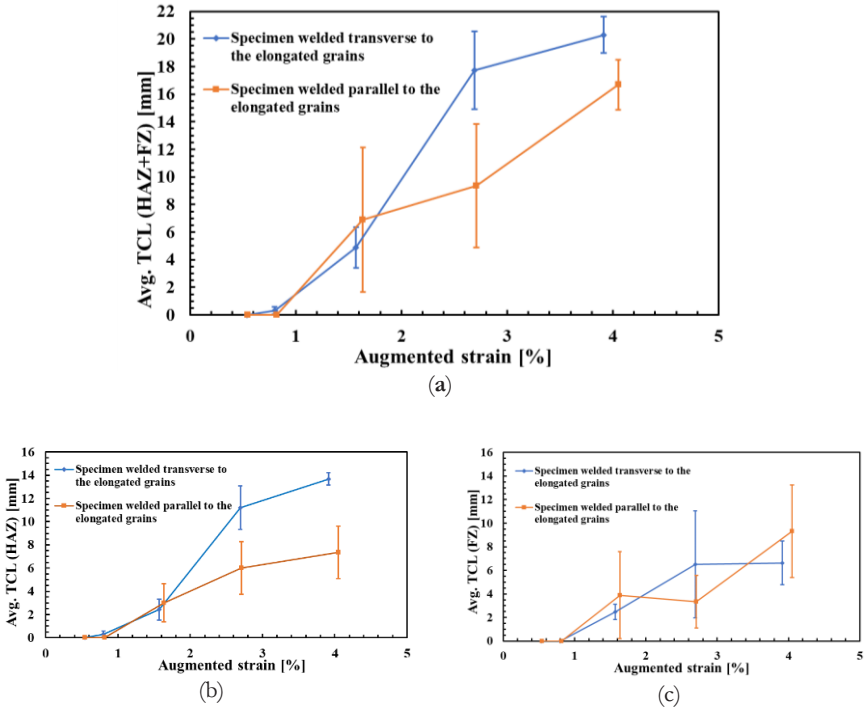
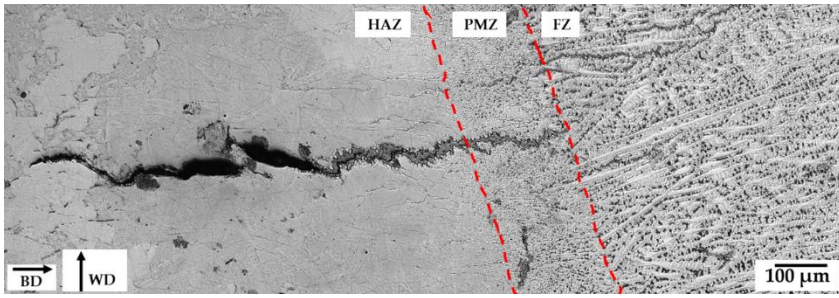
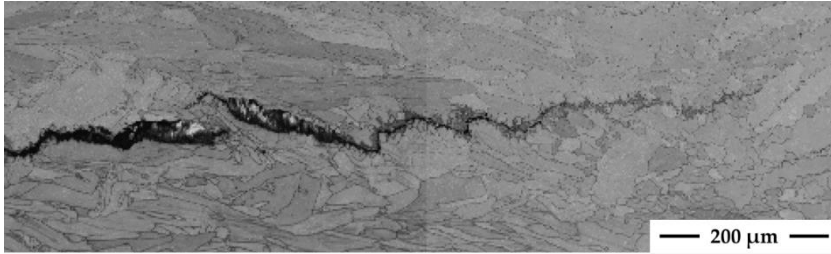


Figure 26. (a) Graphs showing the average of the total crack length (TCL) in both HAZ and FZ, (b) in only HAZ, and (c) in only FZ, versus augmented strain, in the specimen welded parallel and transverse to the elongated grains. (From Paper E)

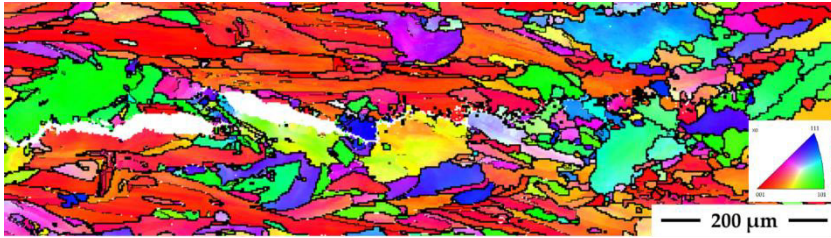
Most cracks in the samples were initiated in the PMZ (Figures 27 and 28) and were extended away from the fusion line into the HAZ along the grain boundary paths. PMZ is shown in the Figures 27a and 28a and highlighted with red dashed lines. Some cracks were initiated in HAZ too. The EBSD analysis of the specimens demonstrated that crack propagation in PMZ and HAZ always occurred along high angle grain boundaries (Figures 27c and 28c). This cracking behaviour was similar in both types of welded samples.



(a)



(b)



(c)

Figure 27. (a) Optical micrograph showing base metal (BM), heat affected zone (HAZ), partially melted zone (PMZ), and fusion zone (FZ) of the specimen welded transverse to the sample building direction (BD) (Note: the welding direction (WD) is transverse to the grain orientation). (b) SEM micrograph showing the unetched microstructure of the welded sample. (c) EBSD inverse pole figure (IPF) colour mapping of the same image as (b). (From **Paper E**)

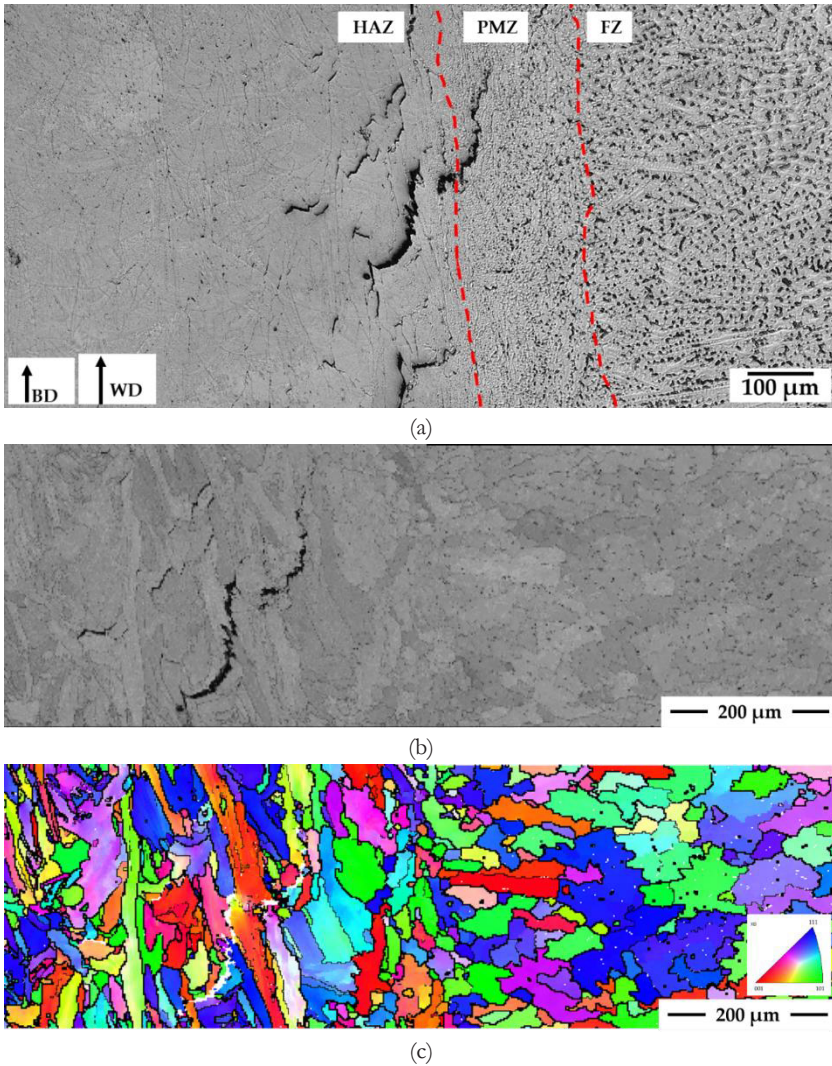


Figure 28. (a) Optical micrograph showing base metal (BM), heat affected zone (HAZ), partially melted zone (PMZ), and fusion zone (FZ) of the specimen welded parallel to the sample building direction (BD) (Note: the welding direction (WD) is parallel to the grain orientation). (b) SEM micrograph showing the unetched microstructure of the welded sample. (c) EBSD inverse pole figure (IPF) colour mapping of the same image as (b). (From **Paper E**)

4.6 Gleeble hot ductility test

The aim of this study was first to investigate the hot ductility behaviour of L-PBF-718 in the as-built and HIP samples, and to compare samples produced by two

different L-PBF-systems to understand the effect of process-induced defects on hot ductility of the material. Hot ductility tests were performed using a Gleeble 3800D system. The on-heating and on-cooling hot ductility for samples produced by M1 and M2 in the as-built condition is shown in Figure 29. A comparison of the hot ductility for L-PBF as-built (M1 and M2), L-PBF HIPed (M2), and wrought conditions is shown in Figure 30. The samples produced by M1 that were subjected to HIP treatment were brittle and broke while clamping in the Gleeble machine making it impossible to run the test on these samples.

The hot ductility signatures in Figure 29 show that samples made by M2 showed better maximum ductility both for the on-heating and on-cooling ductility. Figure 30 reveals that the L-PBF material made by M2 in HIPed condition had a lower maximum ductility in comparison to the as-built samples made by the same process and machine. Furthermore, it can be seen that the ductility of L-PBF material in any condition, was not as good as that of wrought Alloy 718.

Weldability parameters NDT, DRT, BTR, DRR, and RDR were estimated from the data plots in Figure 30 and are shown in Table 10.

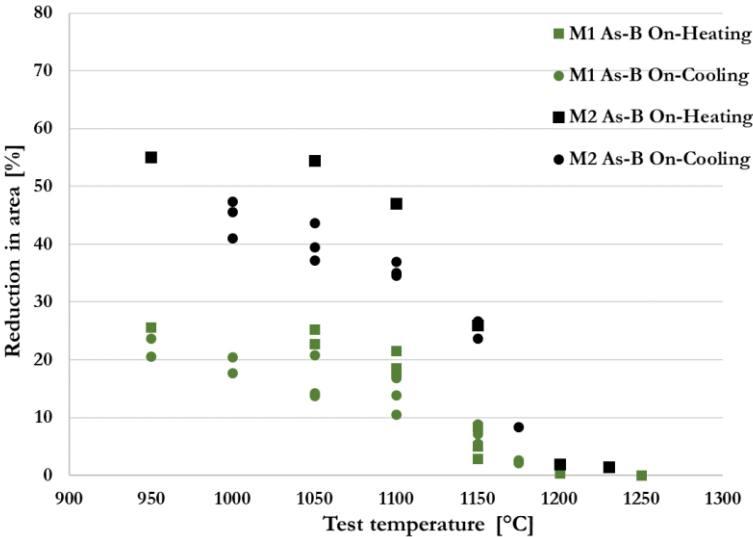


Figure 29. Hot ductility signatures for the L-PBF as-built samples produced in Machine 1 and Machine 2 systems. The graph illustrates material ductility (reduction in area) plotted as a function of the test temperature.

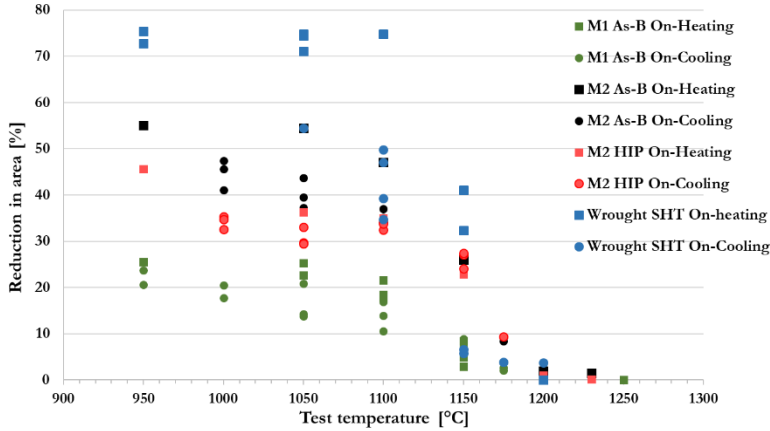


Figure 30. Hot ductility signatures for the L-PBF as-built and HIPed samples produced in M1 and M2 systems. Wrought Alloy 718 is used as reference material. The graph illustrates material ductility (reduction in area) plotted as a function of the test temperature.

Table 10. Estimated weldability parameters obtained from the hot ductility plots in Figure 30.

Hot ductility parameters	M1 As-built	M2 As-built	M2 HIP	Wrought
NDT [°C]	1200	1230	1230	1200
DRT [°C]	1150	1175	1175	1150
BTR [°C]	45	20	20	45
DRR [%]	68	74	85	74
RDR [%]	75	81	98	53

5 Discussion

This chapter aims to discuss the process parameters, general solidification features, and typical microstructures seen in L-PBF-718, in as-built and heat-treated conditions. Furthermore, different aspects of weldability of L-PBF-718 will be discussed and compared with wrought and cast Alloy 718. Finally, the chapter will be completed by some concluding remarks.

5.1 Process development

Several studies (see **Paper A**) have examined various combination of process parameters to obtain near to fully dense Alloy 718 by the L-PBF process [75-77].

Research studies have shown that the process parameters that have a significant impact on the final part quality are those that affect the volume of liquid phase created during the melting process, i.e. laser power and scanning speed [26, 75-78]. The overall quality of the L-PBF-manufactured part is governed by the number of process-induced defects. In the present work, a parametric study was performed to understand the effect of laser related parameters, such as laser power, point distance, and exposure time, on the generation of defects. Thus, minor changes in any processing parameter can have large effects on the final material quality regarding defects.

Porosity formation, according to most studies performed on L-PBF-manufactured parts, is dominated by the processing procedure (see **Paper A**). Process parameters need to be properly adjusted to avoid mechanisms that can create porosities. To produce parts with low or no porosity, optimisation of process parameters for a specific material is the first stage. Furthermore, to identify the process window for a specific material, a typical process optimisation is usually performed in several steps. Generally, process optimisation steps include the stable formation of (i) single tracks, (ii) thin walls, and finally, (iii) simple geometries like cubes or cylinders. This process is performed until a satisfactory process parameter window is identified. These studies were performed by varying two or three process parameters at a time and many other parameters are neglected. The typical experimental method is a trial and error approach. An optimised process parameter set needs to be obtained for each combination of materials, machines and geometries to produce a 100% dense and void-free material. In addition, this existing process optimisation method is both time consuming and expensive.

One of the important characteristics for laser material interaction is the laser beam emission type, i.e. pulsed wave (PW) or continuous wave (CW) [79]. In the present study, a comparison between specimens made by two different L-PBF-machines, one using PW and other using CW, was performed to investigate the effect of their laser emission modes on porosity formation. Results showed that samples made with CW had almost no lack of fusion between the layers. Because the running mechanism of these two laser modes are different, they create different thermal histories during manufacturing [80]. Demir et al. [81] studied the effect of exposure time and pulse overlapping on a maraging steel and concluded that a CW laser is preferable for manufacturing large fully dense parts because it yields a lower porosity because of the bigger melt pool depth (almost double than that in the PW). In contrast, PW is more suitable for fine and precise structures

because of its controllability in pulse overlap percentages. The overlap mechanism is related to the scanning speed and the hatch spacing. Hence, the overlap percentage is one of the factors determining the part building speed. If the hatch spacing is large or the scan speed is too high, the overlap percentages decrease, and the building speed becomes faster. However, this strategy will build parts with higher porosity as the interlayer bonding is weaker in the small overlap percentage [37]. This shows an example of how the process parameters in the L-PBF process are interconnected with each other and why it is important to select a proper parameter set to produce good quality parts.

Although mechanical properties of L-PBF-manufactured parts in several studies have been shown to be comparable with their conventionally produced counterparts, properties can be different because of different processing parameters and local fluctuation within a part [25] (see **Paper A**). To control the mechanical properties of parts, both aspects need to be understood, the process and the evolution of microstructures under complex thermal cycles during the process. The task of industry acceptance requires standardisation and certification of the process. Research is currently ongoing regarding the technical issues within both academy and industry. L-PBF machine suppliers nowadays, optimise process parameters according to their own machines and for their own supplied powder, but their operation of machine and process parameters is proprietary. This makes the final cost of a produced part high and makes the product less affordable.

5.2 Influence of heat treatments on L-PBF-718

The solidification structure of the L-PBF-material, similar to the fusion weld, is mainly influenced by the combination of two key parameters: the temperature gradient GL and solidification growth rate R . As the cooling rate increases, the product of $G \times R$ increases, and a finer structure is formed [25, 82]. The solidification mode observed in as-built samples is cellular-dendritic. The solidification mode is a combined effect of composition, temperature gradient, and solidification rate [13]. The solidification mode is governed by the degree of constitutional supercooling that exists in the liquid immediately in front of solid-liquid interface. Dendritic modes of solidification are favoured by increasing supercooling [82].

By comparing the microstructure of the different manufacturing techniques, it is obvious that L-PBF-718 in the as-built condition is very different from the wrought form and cast form. The microstructure is more like the FZ of a weld,

but on a much finer scale. Laves phase and NbC carbides were seen in the interdendritic regions of the as-built samples (see **Papers C and D**). The solidification microstructure in the precipitation-strengthening iron-nickel-base superalloy, such as Alloy 718 produced by the L-PBF process, consist of a substantial amount of precipitates [83-85]. This is thought to be due to the rapid cooling in the highly localised melt pool which results in a non-equilibrium solidification condition during the L-PBF. Diffusion in the solid is limited under non-equilibrium solidification conditions. There is insufficient time for solute alloying elements, such as Nb and C, to re-diffuse back into the solid. Near the terminal stage of solidification, the concentration of these alloying elements rises in the remaining liquid and eutectic solidification can occur. Precipitates such as NbC and the Laves phase are then formed in the interdendritic regions and grain boundaries [61]. The oxide films at the grain boundaries can also serve as potential sites for nucleation of these phases [86].

Despite the optimised process parameters that were applied in the present study, imperfections, such as spherical pores, irregular lack of fusion defects with unmelted powder particles inside, and cracks initiating from the lack of fusion, were seen in the samples (see **Paper C**). Several researchers have concluded in their studies that the produced parts have an anisotropy in the microstructure and mechanical properties [66, 87, 88]. As mentioned before, the produced samples have a substantial amount of precipitates in the as-built condition because of the non-equilibrium solidification conditions. In addition, the process produces parts with a high surface roughness in comparison to parts manufactured by machining, for examples. Therefore, the L-PBF produced parts must be subjected to various post-process treatments in order to reduce residual stresses, porosity, and segregating elements and to enhance mechanical properties. Heat treatments for AM are generally developed from combining various heat treatments for wrought and cast structures with the addition of a stress relief cycle [8].

HIP treatment is increasingly attracting attention as a post process of L-PBF parts to reduce the inherent porosity. HIP is an established technique for closing porosities after casting and to partly achieve homogenisation [89]. Time, temperature, and pressure are the main parameters in the HIP, and they are varied depending on material, initial segregation, and requirements for grain size control [89, 90]. After HIP, the typical L-PBF columnar morphology was eliminated, grains grew into a coarser and equiaxed grain structure, and the Laves phase was totally dissolved, but residual NbC carbides and a small amount of TiN were observed in the microstructure. Furthermore, HIP treatment did not close all the porosities present in the as-built condition. The grain size after HIP became twice

as large as it was in the wrought samples used in the present work. Recrystallisation of grains was observed in the samples (see **Papers C and D**). Some studies have discussed the causes of this recrystallisation in HIP process. According to Aydinöz et al. [28], a high temperature in HIP causes local deformation that consequently leads to high driving forces for recrystallisation. According to Amato et al. and Song et al. [51, 91], the accumulated residual stresses from the L-PBF process provide internal energy to drive recrystallisation during HIP.

As described before, the Laves phase is a brittle non-equilibrium intermetallic phase that is formed in Alloy 718 usually as a result of segregation. It consumes alloying elements required for strengthening precipitates and provides favourable sites for crack initiation [92]. Therefore, a minimum amount of the Laves phase is preferred in the Alloy 718 parts [92]. The standard SHT at 954 °C for 1 h used for casting as well as for wrought Alloy 718 [8] was performed on the L-PBF specimen which resulted in a partially dissolved Laves phase. Because of this partial dissolution of the Laves phase, there was enough amount of Nb to form the δ -phase near the remaining undissolved Laves phase. The solution temperature of 954 °C was not enough to completely dissolve the Laves phase. According to the literature [39], Laves phase in the cast structure can be minimised to develop the required properties by homogenising at 1120 °C or above.

In specimens that underwent SHT followed by a two-step ageing treatment (SHT+AGE) for 5 h at 760 °C and 1 h at 649 °C, the strengthening phases γ' and γ'' were precipitated in the matrix. Some remnants of the Laves phase along with δ -phase, carbides, and nitrides remained in the microstructure. A recent study regarding heat treatment optimisation for L-PBF-manufactured Alloy 718 claimed that a single ageing step could be enough to form both strengthening precipitates because of the observation of fully developed γ' and γ'' phases already after the first step of ageing at 760 °C [91]. Ageing treatments are known to strengthen the alloy by precipitating the γ' and γ'' phases from the supersaturated matrix developed by rapid cooling after solution treatment. The selection of ageing steps, time, and temperature is influenced by the type and number of precipitates, desired precipitate size, desired combination of strength and ductility, and anticipated service temperature [69]. When more than one phase can be precipitated from the alloy matrix, a double-ageing treatment that produces different types and bimodal size distribution of precipitates at different temperatures, is employed. According to an article from the year 1967 written by

R. C. Hall, when two ageing temperatures are used and the second heat treatment temperature is about 110° C below the first one, the alloy strength increases by 10 to 20 Ksi over a single ageing treatment [93].

In summary, nearly all applications of L-PBF-manufactured material require some degree of post processing, heat treatment, and finishing. Previous studies regarding post-process heat treatments of L-PBF-718 have been focused on industry-standard heat treatments of Alloy 718 developed for conventional cast and wrought material. However, the microstructure of L-PBF-718, resulting from the high cooling rate, is different compared to cast and wrought Alloy 718. Consequently, the precipitation behaviour of L-PBF-718 may differ. For example, a recent study regarding optimisation of heat treatments for L-PBF-718 reported that the originally recommended heat treatment process of SHT at 980 °C for cast and wrought materials was not effective for the L-PBF-processed material because of the significant formation of the Nb-rich δ -phase in association with partial dissolution of the Laves phase in the interdendritic regions [52]. Another recent study reported that the precipitation temperatures of γ' and γ'' are about the same for L-PBF-718 and wrought Alloy 718, but the former has a faster ageing response [94]. Another example can be the dissolution temperature of the Laves phase, which is known to be 1120 °C in cast Alloy 718 [39], but heat treatments at 1120 °C of L-PBF-718 have shown to promote an inhomogeneous grain growth in L-PBF-718 which in turn decreased the creep properties of the material [52]. These few examples demonstrated why there is a need of developing specific heat treatments for L-PBF-718.

5.3 Welding and weldability testing of L-PBF-718

The definition of weldability in the present work was the susceptibility toward hot cracking in the HAZ during welding. Regarding weldability, all five material conditions tested, L-PBF as-built, HIP, SHT, SHT+AGE, and wrought, experienced the same process of HAZ liquation cracking. However, the cause of liquation seemed to be different for different conditions (see **Paper D**). In the L-PBF as-built, SHT, and SHT+AGE conditions, incipient melting of the Laves phase was most likely the cause of HAZ liquation cracking. This can be rationalised according to the studies regarding the HAZ liquation cracking in cast Alloy 718 that also contains the Laves phase [92]. In contrast, by direct HIP of the L-PBF-718 at 1160 °C for 3 h, the Laves phase was completely dissolved, but carbides were present in the microstructure. There were fewer cracks in the HAZ of the L-PBF-HIP and wrought material. However, if standard error bars are

compared, the differences in TCL were not shown to be statistically significant between all these five conditions.

The grain size is another factor that needs to be considered while discussing the weldability of materials. It has generally been recognised that fine-grained materials are more resistant to HAZ liquation cracking than coarse-grained versions of the same material [65]. Grains in the L-PBF-manufactured material were fine in one direction and elongated in the perpendicular direction (Figure 14a). Grain size measurements performed in **Paper B** showed that the L-PBF as-built specimen had an average grain length of 80 μm and width of 20 μm . The wrought Alloy 718 had an average grain size of approximately 25 μm . The grain size of the cast material cannot be clearly observed in Figure 14c, but another study [95] regarding hot cracking in cast Alloy 718 (which used the same material as that in the present study), showed that the average grain size of the as-cast base metal (BM) was approximately 1700 μm . Thus, it could be expected that L-PBF-manufactured material in the as-built condition and wrought material had similar cracking sensitivities. However, this was not the case in the present study because the L-PBF-718 in as-built condition had slightly higher number of cracks than the wrought material.

In all L-PBF conditions in the present study, “clean” cracks, i.e., cracks without any eutectic formation, were also observed (for example, Figure 21). These cracks were situated in the part of the HAZ where the temperature range during welding was between 1150 and 1200 $^{\circ}\text{C}$ (Figures 18a and b). The question was whether this occurred because of any other cracking mechanism, for example segregation of elements such as B, P, C, or S in the grain boundaries [13, 39, 96]. According to the literature [58, 60, 97, 98], B causes increased HAZ cracking sensitivity if present much above 0.003 wt. %. B in the powder feedstock used for the manufacturing of Alloy 718 with L-PBF process in the present study was approximately 0.006 wt. % and was 0.003 wt. % in wrought Alloy 718. This could also be a reason for the higher cracking susceptibility of the L-PBF material. This phenomenon requires further study for L-PBF-manufactured Alloy 718. A quantitative analysis performed by secondary ion mass (SIMS) could possibly give a more accurate answer to this question, as shown in reference [98].

Another possible reason for the relatively high cracking susceptibility in the L-PBF material could be that the microcracks were already created during the L-PBF process. Several nickel-base superalloys have been documented as being particularly susceptible to microcracking when processed by the laser additive

manufacturing process [99, 100]. These microcracks can act as crack initiating sites during the cooling process after welding because of the local stresses in the material. Several studies have claimed that HIP can be used to close the cracks [54]; however, surface cracks and open pores remain [24]. Furthermore, HIP can cause grain coarsening in the material which can also be an issue in connection with welding.

The investigation performed by Vareststraint testing showed that the L-PBF-718 in the HIP condition had a higher degree of hot cracking at all the strain levels in comparison to L-PBF in the as-built and wrought conditions (see **Paper B**). This was further supported by the observation that the average crack width was larger in the HIPed material. One of the reasons for this increased sensitivity was the larger grain size of the HIPed material. The grain boundaries of coarse grain size material are more prone to cracking because they must accommodate larger localised strains compared to the material with smaller grain size [13, 65]. Furthermore, less grain boundary area associated with coarse grain size results in more stress concentration applied to the grain boundary triple points in which crack initiation is most likely to occur [13]. However, it should be pointed out that in this study, it was not possible to judge where crack initiation had taken place.

The TCL presented in Figure 23 shows that the L-PBF as-built specimens have the same HAZ cracking sensitivity as the reference wrought material. As mentioned before, grains in the L-PBF-manufactured material had a columnar grain structure, with a preferential grain growth in the $\langle 001 \rangle$ orientation parallel to the BD. However, the wrought material had equiaxed grains. Welding was performed parallel to the L-PBF-sample BD, and consequently, the smaller side of the grains was located perpendicular to the welding direction. Thus, it would be expected that the as-built specimens should show even better crack resistance than the wrought material, but this was not the case in this study. In contrast, Figures 24 and 25a it seems that the cracks to a large extent followed the vertical grain boundaries in the as-built sample. In the HIP material cracks followed both vertical and horizontal grain boundaries (Figure 25c), and in the wrought material, the cracks followed the horizontal grain boundaries (Figure 25e). Cracking in all three conditions occurred because of the liquation mechanism, as was also found by previous studies [11, 12], with irregularly shaped constituents surrounding the cracks. These constituents were Nb-rich and thus could be NbC carbides or γ /Laves phase eutectic [101]. Some cracks without any eutectic formation were also observed in the L-PBF samples (see **Paper D**). The weld FZ of the L-PBF

as-built condition revealed γ /Laves phase eutectic and NbC carbides, similar to that reported in previous studies on weld FZ of wrought Alloy 718 [61, 102].

Severe cracking susceptibility in the L-PBF-HIP Alloy 718 can be associated with grain boundary segregation of minor elements because of the HIPping temperature of 1160 °C. A study by Huang et al. [98] showed that TCL in cast Alloy 718 welded samples was first decreased with pre-weld heat treatment temperature from 1037 °C to 1067 °C and then increased in samples heat treated from 1067 °C to 1163 °C. They performed SIMS analyses to examine the samples and concluded that the weldability of the alloy was directly related to the segregation of B on grain boundaries, being a function of the relative amount of segregation during pre-weld heat treatment. Segregation of the minor elements can reduce the melting point of the grain boundary, making these grain boundaries prone to liquation during the welding process and consequently giving rise to HAZ cracking in welded joints.

In summary, notably HAZ cracking problems are significantly influenced by overall alloy composition, microstructure, and localised chemistry of intergranular regions. The cracking not only occurs by the formation of liquid films from the various sources but also the mechanical stresses emerging from the temperature gradients and the resulting plastic deformation associated with the movement of the liquid metal zone along the weld [13].

Welding direction in relation to the grain growth direction in L-PBF-718 was also found to have a significant influence on the hot cracking susceptibility during the welding process (see **Paper E**). Vastrestraint testing was performed on the as-built condition of the material. The extent of HAZ cracking was observed to be smaller in samples welded parallel to the elongated grain orientation than in samples where welding was performed transverse to it. Cracking in the FZs of both types of the samples showed no significant differences in amount. In contrast, in the HAZ, there was almost twice as much cracking in the samples welded transverse to the elongated grain orientation, compared with samples welded parallel to the elongated grains.

The EBSD analysis of both types of welded specimens demonstrated that crack propagation in PMZ and HAZ always occurred along the high angle grain boundaries (see **Paper E**). According to previous studies [64], the high angle grain boundaries were more susceptible to HAZ cracking during welding because of their ability to accommodate a large number of segregated elements, in comparison with low angle grain boundaries. In addition, Guo et al. [103] and

Ojo et al. [104] reported that grain boundary wetting and liquid penetration are enhanced at high angle grain boundaries in the HAZ of cast superalloys during welding.

In the samples welded transverse to the grain orientation, the cracks were longer, widely opened, and uninterruptedly occurred along the favourably oriented grain boundaries perpendicular to the FZ. In contrast, the cracks in samples welded parallel to the elongated grain orientation were observed to run parallel to the fusion line, and they only occasionally extended farther away into the HAZ. This is probably due to the small number of favourably oriented grain boundaries in the HAZ, making crack propagation into the HAZ difficult.

Cracks in the present study were caused by a combination of two main factors: mechanically induced external strain due to Vareststraint test method and the crack susceptible microstructure. In the welded samples, cracks initiated in the PMZ, which is the region adjacent to the fusion line and where the temperatures are sufficiently high to produce melting along the grain boundaries. During the heating cycle of the welding, liquation of precipitates already existing in L-PBF material occurs in this partially melted region. When a strain was applied during the Vareststraint test, these liquated grain boundaries became susceptible to hot cracking. Furthermore, the columnar grain boundaries served as the path along which damage could easily occur, leading to fracture. In contrast, in the transverse direction, the columnar grains led to high strength [105]. Thus, it is possible to have less HAZ cracking if the L-PBF-manufactured material is welded parallel to the BD and along the elongated grain orientation to avoid high angle grain boundaries favourably oriented transversely in the HAZ.

In the study regarding hot ductility of L-PBF-718, samples produced in two different L-PBF systems were used. The purpose was to investigate the influence of different laser modes, powder layer thickness, and quality of produced parts in terms of defects. Some indication of the material's mechanical properties and weldability could be obtained by comparing the elevated temperature ductility behaviour of the material. L-PBF-718 in general and L-PBF-HIP Alloy 718 in particular exhibited poor material properties in terms of ductility. The factors that can be of concern regarding the results in this study are discussed below.

According to Aydinöz et al. [28], the reasons for the limited ductility results of the L-PBF-718 samples in the as-built condition could be the presence of high dislocation density areas and the significant amount of the Laves phase in the microstructure. Wrought samples used in the study were in the SHT condition

and did not contain any Laves phase. The Laves phase is a brittle non-equilibrium intermetallic phase that is formed in Alloy 718 usually as a result of segregation and which is detrimental for the mechanical performance of the material [92]. Another reason for the lower ductility of the material could be the residual oxides from the L-PBF process [44]. Oxide formation in L-PBF-718 has been confirmed by several researchers [44, 46, 47], and the origin of the oxygen is reported to be the contaminated raw powder surface during powder handling and oxygen in the L-PBF chamber. The oxygen is difficult to remove, and it easily reacts with powder to form oxides during the L-PBF process.

The testing of the L-PBF samples was performed parallel to the BD, i.e. parallel to the elongated grain direction. This could also be a reason for the lower ductility values of the as-built samples. Studies regarding mechanical properties of L-PBF-718 reported that the specimen tested parallel to the BD showed a lower tensile strength than the samples tested perpendicular to the BD [40, 50].

Identical samples that were produced on different machines could exhibit a statistically significant difference in material properties. One reason for this could be the amount of lack of fusion defects which were present in a significant amount in the M1 samples in comparison to the M2 samples which had almost no lack of fusion defects.

As mentioned before, HIP treatment at approximately 1160 °C showed detrimental effects on Alloy 718 weldability because of elemental segregation on the grain boundaries and grain coarsening due to recrystallisation [58, 96]. Previous studies have shown that, coarse-grained materials are more prone to HAZ liquation cracking than fine-grained versions of the same material [65]. Studies have also shown that B in Alloy 718 can segregate to the grain boundaries during cooling from the pre-weld heat treatments that can consequently lower the melting temperature of the grain boundaries [58, 98]. If the segregation of B is sufficiently high, the grain boundaries are likely to liquate in the HAZ during the heating cycle of the welding process [103].

The BTR values determined from the hot ductility curves were in favour of the L-PBF-material produced in M2 compared to specimen produced in M1 and wrought Alloy 718. The specimen produced in M1 and wrought Alloy 718 showed higher BTR than the specimen produced in M2 (Table 10). This was a result opposite from the Varestraint test results where wrought condition was less susceptible to hot cracking. However, the BTR criterion is considerably rough when compared with the different conditions of a specific material. Another

criterion that can be used to relate to both on-heating and on-cooling signature of the material refers to the DRR. The DRR criterion compares the maximum ductility during on-heating with the corresponding ductility during on-cooling at the same temperature [106]. If the ductility recovery on-cooling matches the ductility for on-heating, the material is considered to be crack resistant [107]. DRR at a 1050 °C test temperature showed similar ductility recovery behaviour in all material conditions (Table 10). A third concept in evaluating Gleeble hot ductility results is the RDR which is related to the ductility recovery in the temperature range from NDT to the temperature that is associated with the formation of grain boundary liquation in the HAZ. Since DRR only reflects the ductility recovery for a specific temperature at which it is determined, BTR only refers to the on-cooling ductility signature it is not unreasonable that RDR will be a complimentary criterion for predicting a material's HAZ hot cracking behaviour. RDR reflects the ductility response for both on-heating and on-cooling over the whole temperature span of interest. RDR can be associated with the base metal hot cracking initiation and the propagation temperature range because the temperature at which ductility reduces is considered to represent the onset of liquation [107]. If the BTR for a material is large and RDR or DRR is small, the material will be more sensitive to HAZ liquation cracking. The calculated RDR values are correlated with the BTR values, showing the specimen produced in M1 and Alloy 718 in wrought condition to be more sensitive towards HAZ hot cracking. For a more precise estimation of BTR, RDR, and DRR criteria, more tests need to be performed at the temperatures of interest, but unfortunately the number of samples was not enough to accomplish this in the present study.

According to the estimated RDR, the wrought sample is the most susceptible condition to hot cracking; however, considering the overall results of reduction in area percentage (RA%) that provides the measure of ductility of a material, it could be clearly seen that wrought Alloy 718 had the highest ductility value of all the material conditions (Figure 30). The ductility value for wrought condition at 950 °C was approximately 75%, whereas the ductility value for the M2 specimen, which did not have any lack of fusion, was approximately 55%. The M2 specimen in HIP condition had an even lower ductility value of approximately 45%, and the M1 specimen which contained a large amount of lack of fusion had the lowest ductility value approximately 25%. The conclusion that can be drawn is that L-PBF-manufactured Alloy 718, in any material condition, had an overall lower ductility behaviour in comparison to wrought Alloy 718.

6 Responses to research questions

In the present research, first, the influence of L-PBF process parameters on manufacturing of samples and occurrence of defects was investigated. Second, the effect of different heat treatments on the defects, microstructure, and weldability of L-PBF-718 was investigated. Furthermore, the influence of grain orientation on the susceptibility toward hot cracking during welding of the material was studied. The conclusions are summarised and presented below as responses to the research questions.

RQ 1. What type of defects appear in the L-PBF-manufactured parts and how are they affected by specific process parameters? (*Papers A and C*):

Lack of fusion and gas porosity are common defects in L-PBF-manufactured parts. The research performed at hand regarding the process parameters showed that laser power, scanning speed, laser exposure time, and laser point distance are the most influential process parameters considering the decreasing amount of lack of fusion. In contrast, gas porosities are unavoidable in the L-PBF material because they can occur either due to powder particles containing inherent gas pores from the powder atomisation process or entrapped shielding gas during the L-PBF process.

RQ 2. What is the influence of post-process heat treatments on L-PBF-718 microstructure? (*Papers C and D*):

L-PBF-718 in the as-built condition exhibited a cellular-dendritic structure within the columnar grains with NbC carbides and a low melting Laves phase present in the interdendritic regions and along the grain boundaries. A small amount of TiN was also detected in the material. Hot isostatic pressing (HIP) treatment at 1160 °C for 3 h altered the grain morphology to coarser equiaxed grains. The Laves phase was completely dissolved, but carbides were present in the microstructure. HIP treatment could not close all lack of fusion defects, and gas porosity also remained in the material.

The standard solution heat treatment (SHT) at 954 °C for 1 h, used for casting as well as for wrought Alloy 718, was used on the L-PBF specimen in the present study resulted in partially dissolved Laves phase. Due to this partial dissolution of the Laves phase, there was enough Nb to form the δ -phase near the remaining

undissolved Laves phase. Grain morphology was not changed because this heat treatment.

In specimens heat treated by solution heat treatment followed by a two-step ageing treatment (SHT+AGE) for 5 h at 760 °C and 1 h at 649 °C, the strengthening phases γ' and γ'' were precipitated in the matrix. Some remnants of the Laves phase along with the δ -phase, carbides and nitrides also remained in the microstructure.

RQ 3. What is the susceptibility towards cracking in L-PBF-718 during welding? (*Papers B, D and E*):

L-PBF-718 was susceptible to HAZ cracking in all material conditions, i.e. as-built, HIP, SHT as well as SHT+AGE. However, the HIP treated material had a higher susceptibility toward cracking because of the coarser grain size in comparison with wrought Alloy 718. Furthermore, the HIP treated material showed lower ductility during hot ductility testing which indicated that HIP treatment of L-PBF-718 at 1160 °C for 3 h was not appropriate for the material.

Welding either along the growth direction of the grains or perpendicular to that direction in L-PBF-718 showed a significant influence on hot cracking susceptibility during the welding process. The extent of HAZ cracking was observed to be smaller in samples welded parallel to the elongated grain orientation than when welding was done transverse to the elongated grain orientation.

6.1 Concluding remarks

Despite extensive research on L-PBF-718 over recent years, significant challenges and knowledge gaps that require further investigation still remain. The adoption of L-PBF technology in the aerospace industry faces challenges such as high cost, low production rate, void formation, anisotropic behaviour, and inconsistent quality of the manufactured parts. A variability exists in the reported mechanical properties of L-PBF-718 parts. In some studies, they are shown to be comparable with their conventionally produced counterparts and in other studies they are shown to be inferior. This variability is rooted in the L-PBF method itself, and the properties can be different because of different processing parameters and local fluctuations within a part. The research and development of materials and

methods, within both industry and academy, have helped to overcome some of these challenges. However, few remaining challenges need to be addressed to expand the use of the technology to a broader range of applications and industries. The future of the L-PBF as a production technology to be used in aerospace industry depends on fulfilling the stringent requirements regarding the quality, process reliability, processing time, and cost.

7 Recommendations for future work

Apart from providing answers to the research questions, the present study also showed that further work is needed. It is therefore suggested that future work should be performed in the following areas:

- Investigation of hot ductility of the material should be completed by performing more tests at the temperatures of interest and microstructural characterisation of tested specimens to understand the overall lower ductility behaviour of the L-PBF-718 material.
- Proper heat treatment cycles must be designed to address fabricability challenges for the specific component at stake.
- Experiments regarding HIP treatment at different temperatures, dwell times, and pressures to get better closing of defects without grain coarsening are required.
- Non-destructive methods to efficiently evaluate the quality and dimensional accuracy of the L-PBF-manufactured parts are needed to increase the confidence in production with L-PBF.
- Parts produced by any AM process are naturally anisotropic. Most studies have examined porosity as a function of process parameters, but very few have linked the results to mechanical properties. Mapping porosity to thermo-mechanical properties, both static and cyclic, will be a valuable investigation.
- Since defects are unavoidable, determining a critical defect size will also be valuable to use L-PBF as a commercial production process.

8 References

- [1] ISO/ASTM 52900:2015, Standard Terminology for Additive Manufacturing - General Principles - Terminology, ASTM International, New York, NY, 10036.
- [2] I. Gibson, D. Rosen, and B. Stucker. Additive manufacturing technologies: 3D Printing, Rapid Prototyping, and Direct Digital Manufacturing, Second edition. Ed. New York; London: Springer, 2015.
- [3] Loughborough University, “Direct energy deposition”. Available at: <https://www.lboro.ac.uk/research/amrg/about/the7categoriesofadditivemanufacturing/directedenergydeposition/> [Accessed: 2019-09-12]
- [4] S. Brodin, L. Forsberg, and U. Palmnäs, Turbine design for Ariane 6 vulcain turbopumps upgrades, in 7th International Swedish Production Symposium 2016, Lund, Sweden. AAAF Space Propulsion, May 2-6, 2016.
- [5] D. Herzog, V. Seyda, E. Wycisk, and C. Emmelmann. Additive manufacturing of metals. *Acta Materialia*, 117 (2016), 371-92.
- [6] J.P. Kruth, P. Mercelis, J. Van Vaerenbergh, L. Froyen, R. Marleen, Binding mechanisms in selective laser sintering and selective laser melting. *Rapid Prototyping Journal*, 11:1 (2005), 26-36.
- [7] B. Zhang, Y. Li, and Q. Bai, Defect Formation Mechanisms in Selective Laser Melting: A Review. *Chinese Journal of Mechanical Engineering*, 30 (2017), 515-527.
- [8] ASTM-International Standard Specification for Additive Manufacturing Nickel Alloy (UNS No7718) with powder bed fusion. F3055- 12, ASTM Intl, West Conshohocken, ASTM International. 2014.
- [9] H.L. Wei, H.K.D.H. Bhadeshia, S.A. David and T. DebRoy, Harnessing the scientific synergy of welding and additive manufacturing, *Science and Technology of Welding and Joining*, 24:5 (2019), 361-366.
- [10] H.Y. Wan, Z. J. Zhou, C.P. Li, G.F. Chen and G.P. Zhang, Effect of scanning strategy on grain structure and crystallographic texture of Inconel 718

processed by selective laser melting, *Journal of Materials Science & Technology* 34 (2018) 1799-1804.

[11] W.A. Baeslack and D.E. Nelson, Morphology of Weld Heat-Affected Zone Liquation in Cast Alloy 718. *Metallography*, 19 (1986), 371-379.

[12] B. Radhakrishnan and R.G. Thompson, A phase diagram approach to study liquation cracking in Alloy 718. *Metallurgical and Materials Transactions A* 22 (1991), 887-902.

[13] J.N. DuPont, J.C. Lippold and S.D. Kiser, *Welding Metallurgy and Weldability of Nickel-Base Alloys*, John Wiley and Sons: Hoboken, NJ, USA, 2009.

[14] W. Meiners, K.D. Wissenbach and A.D. Gasser, Shaped body especially prototype or replacement part production, U.S. patent DE19649849C1 (1998).

[15] H. Gong, (2013). Generation and detection of defects in metallic parts fabricated by selective laser melting and electron beam melting and their effects on mechanical properties. Dissertation, Doctor of Philosophy, Department of Industrial Engineering, University of Louisville, Louisville, Kentucky.

[16] L.C. April and J.A. Slotwinski, "Properties of Metal Powders for Additive Manufacturing: A Review of the State of the Art of Metal Powder Property Testing", NIST Interagency/Internal Report (NISTIR) 7873,

http://www.nist.gov/manuscript-publication-search.cfm?pub_id=911339

[Accessed: 2019-10-24]

[17] W.J. Sames, F.A. List, S. Pannala, R.R. Dehoff and S.S. Babu, The metallurgy and processing science of metal additive manufacturing, *International Materials Reviews*, 61:5 (2016), 315-360.

[18] W. Sames, Additive Manufacturing of Inconel 718 using Electron Beam Melting: Processing, Post-Processing, & Mechanical Properties, Doctoral dissertation, Texas A&M University, 2015.

[19] J.O. Milewski. Additive manufacturing of metals: from fundamental technology to rocket nozzles, medical implants, and custom jewellery. *Springer Series in Materials Science* 258 (2017), 2196-2812.

- [20] J.J. Dunkley, Atomization. In ASM Handbook, Vol 7, Powder Metal Technologies and Applications. ASM International Publishers, (1998), 35-52.
- [21] T. Kurzynowski, E. Chlebus, B. Kuźnicka and J. Reiner, Parameters in selective laser melting for processing metallic powders. In: Beyer E, Morris T, editors, (2012), 823-914.
- [22] H.D. Carlton, A. Haboub, G.F. Gallegos, D.Y. Parkinson and A.A. MacDowell, Damage evolution and failure mechanisms in additively manufactured stainless steel. *Material Science and Engineering A* 651 (2016), 406-414.
- [23] J.S. Dunning and R.C. Doan, Microstructural characteristics and gas content of rapidly solidified powders, *Journal of material science* 29 (1994), 4268-4272.
- [24] W. Tillmann, C. Schaak, J. Nellesen, M. Schaper, M.E. Aydinöz and K. P. Hoyer, Hot isostatic pressing of IN718 components manufactured by selective laser melting. *Additive Manufacturing* 13 (2017), 93-102.
- [25] T. DebRoy, H.L. Wei, J.S. Zuback, T. Mukherjee, J.W. Elmer, J.O. Milewski, A.M. Beese A.M., A. Wilson-Heid, A. De and W. Zhang. Additive manufacturing of metallic components - Process, structure and properties. *Progress in Materials Science*, 92 (2018), 112-224.
- [26] L.N. Carter, M.M. Attallah and R.C. Reed. Laser powder bed fabrication of nickel-base superalloys: Influence of parameters; characterisation, quantification and mitigation of cracking, *Superalloys* (2012), 577-86.
- [27] Z. Wang, K. Guan, M. Gao, X. Li, X. Chen and X. Zeng. The microstructure and mechanical properties of deposited-IN718 by selective laser melting, *Journal of Alloys and Compounds*, 513 (2012), 518-523.
- [28] M.E. Aydinöz, F. Brenne, M. Schaper, C. Schaak, W. Tillmann, J. Nellesen and T. Niendorf, On the microstructural and mechanical properties of post-treated additively manufactured Inconel 718 superalloy under quasi-static and cyclic loading. *Materials Science and Engineering: A*, 669 (2016), 246-258.
- [29] C.Y. Yap, C.K. Chua, Z.L. Dong, Z.H. Liu, D.Q. Zhang, L.E. Loh, and S.L. Sing. Review of selective laser melting: Materials and applications. *Applied Physics Reviews* 2:4 (2015), 041101.

- [30] I. Yadroitsev, Selective Laser Melting: Direct Manufacturing of 3D-Objects by Selective Laser Melting of Metal Powders. LAP Lambert Academic Publishing, Saarbrücken. 2009.
- [31] E. Louvis, P. Fox and C.J. Sutcliffe, Selective laser melting of aluminium components, *Journal of Materials Processing Technology*, 211 (2011), 275-284.
- [32] D. Gu and Y. Shen, Effects of processing parameters on consolidation and microstructure of W-Cu components by DMLS, *Journal of Alloys and Compounds*, 473:1-2 (2009), 107-115.
- [33] J.A. Cherry, H.M. Davies, S. Mehmood, N.P. Lavery, S.G.R. Brown and J. Sienz, Investigation into the effect of process parameters on microstructural and physical properties of 316L stainless steel parts by selective laser melting, *The International Journal of Advanced Manufacturing Technology*, 76:5-8 (2014), 869-879.
- [34] R. Li, J. Liu, Y. Shi, L. Wang and W. Jiang, Balling behavior of stainless steel and nickel powder during selective laser melting process, *The International Journal of Advanced Manufacturing Technology*, 59 (2011), 1025-1035.
- [35] R. Fabbro, Melt pool and keyhole behaviour analysis for deep penetration laser welding, *Journal of Physics D: Applied Physics*, 43:44 (2010) IOP Publishing, 445501.
- [36] W.E. King, H.D. Barth, V.M. Castillo, G.F. Gallegos, J.W. Gibbs, D.E. Hahn, C. Kamath and A.M. Rubenchik, Observation of keyhole-mode laser melting in laser powder-bed fusion additive manufacturing. *Journal of Materials Processing Technologies*, 214:12 (2014), 2915-2925.
- [37] N.T. Aboulkhair, N.M. Everitt, I. Ashcroft and C. Tuck, Reducing porosity in AlSi10Mg parts processed by selective laser melting, *Additive Manufacturing*, 1 (2014) 77-86.
- [38] M.M. Kirka, A. Plotkowski, P. Nandwana, A. Chaudhary, S.S. Babu and R. Dehoff, Progress in the Processing and Understanding of Alloy 718 Fabricated Through Powder Bed Additive Manufacturing Processes, *The Minerals, Metals & Materials Society 2018. Proceedings of the 9th International Symposium on Superalloy 718 & Derivatives: Energy, Aerospace, and Industrial Applications*.

- [39] C.T. Sims, N.S. Stoloff, and W.C. Hagel. Superalloys II. John Wiley & Sons, 1987.
- [40] D. Deng, R.L. Peng, H. Brodin and J. Moverare, Microstructure and mechanical properties of Inconel 718 produced by selective laser melting: Sample orientation dependence and effects of post heat treatments. *Materials Science and Engineering: A* 713 (2018), 294-306.
- [41] E. Chlebus, K. Gruber, B. Kuźnicka, J. Kurzac and T. Kurzynowski, Effect of heat treatment on the microstructure and mechanical properties of Inconel 718 processed by selective laser melting, *Material Science and Engineering: A* 639 (2015) 647-655.
- [42] L.M. Sochalski-Kolbus, E.A. Payzant, P.A. Cornwell, T.R. Watkins, S.S. Babu, R.R. Dehoff, M. Lorenz, O. Ovchinnikova, C. Duty, Comparison of residual stresses in Inconel 718 simple parts made by electron beam melting and direct laser metal sintering, *Metallurgical and Materials Transactions A*, 46 (2015), 1419-1431.
- [43] L.C. Ardila, F. Garcíandia, J.B. Gonzalez-Díaz, P. Alvarez, A. Echeverría, M.M. Petite, R. Deffley, and J. Ochoa, Effect of IN718 Recycled Powder Reuse on Properties of Parts Manufactured by Means of Selective Laser Melting, *Physics Procedia* 56 (2014), 99-107.
- [44] A. Strondl, O. Lyckfeldt, H. Brodin and U. Ackelid, Characterization and Control of Powder Properties for Additive Manufacturing, *JOM* 67 (2015), 549-554.
- [45] B.A. Hann, Powder Reuse and Its Effects on Laser Based Powder Fusion Additive Manufactured Alloy 718, *SAE International Journal of Aerospace* 9(2) (2016).
- [46] H. Yu, S. Hayashi, K. Takehi and Y.-L. Kuo, Study of Formed Oxides in IN718 Alloy during the Fabrication by Selective Laser Melting and Electron Beam Melting, *Metals* 9 (2019), 19.
- [47] D. Bourell, J.P. Kruth, M. Leu, G. Levy, D. Rosen, A.M. Beese and A. Clare, Materials for additive manufacturing, *CIRP Annals - Manufacturing Technology*, 66:2 (2017), 659-681.

- [48] F.R. Preli and D. Furrer. Lessons learned from the development, application and advancement of alloy 718. The Minerals, Metals & Materials Society 2014. Proceedings of the 8th International Symposium on Superalloy 718 & Derivatives: Energy, Aerospace, and Industrial Applications.
- [49] D. Zhang, W. Niu, X. Cao and Z. Liu, Effect of standard heat treatment on the microstructure and mechanical properties of Selective Laser Melting manufactured Inconel 718 superalloy, *Material Science and Engineering: A* 644 (2015) 32-40.
- [50] J. Ströbner, M. Terock and U. Glatzel, Mechanical and microstructural investigation of nickel-based superalloy IN718 manufactured by selective laser melting (SLM). *Advanced Engineering Materials* 17:8 (2015), 1099-1105.
- [51] K.N. Amato, S.M. Gaytan, L.E. Murr, E.P.W. Martinez, J. Shindo, J. Hernandez, S. Collins and F. Medina, Microstructures and mechanical behavior of Inconel 718 fabricated by selective laser melting. *Acta Materialia* 60:5 (2012), 2229-2239.
- [52] Y-L. Kuo, T. Nagahari and K. Kakehi, The Effect of Post-Processes on the Microstructure and Creep Properties of Alloy718 Built Up by Selective Laser Melting, *Materials* 11:6 (2018), 996.
- [53] S. Gribbin, J. Bicknell, L. Jorgensen, I. Tsukrov and M. Knezevic, Low cycle fatigue behavior of direct metal laser sintered Inconel alloy 718, *International Journal of Fatigue* 93 (2016) 156-167.
- [54] P.F. Kelley, A. Saigal and A. Carter, Fatigue behaviour of direct metal laser sintered Inconel 718, *International Journal of Precision Technology* 6:3-4 (2016) 277-288.
- [55] R. Konecna, G. Nicoletto, L. Kunz and A. Baca, Microstructure and directional fatigue behavior of Inconel 718 produced by selective laser melting, *Procedia Structural Integrity* 2 (2016) 2381-2388.
- [56] Y-L. Kuo, A. Kamigaichi and K. Kakehi, Characterization of ni-based superalloy built by selective laser melting and electron beam melting, *Metallurgical and Materials Transactions A* 49:9 (2018) 3831-3837.

- [57] Y.-L. Kuo, S. Horikawa, K. Kakehi, Effects of build direction and heat treatment on creep properties of Ni-base superalloy built up by additive manufacturing, *Scripta Materialia* 129 (2017) 74-78.
- [58] T.J. Kelly, Elemental effects on cast 718 weldability, *Welding Journal* 68 (1989): 44-51.
- [59] W.A. Owczarski, D.S. Duvall and C.P. Sullivan, A model for heat affected zone cracking in nickel-base superalloys, *Welding Journal* 45, (1966) 145-155.
- [60] W. Chen, M.C. Chaturvedi and N.L. Richards, Effect of boron segregation at grain boundaries on heat-affected zone cracking in wrought INCONEL 718. *Metallurgical and Materials Transactions A* 32:931 (2001).
- [61] G.A. Knorovsky, M.J. Cieslak, T.J. Headley, A.D. Romig, Jr., and W.F. Hammett, Inconel718: A Solidification Diagram, *Metallurgical Transactions A* 20 (1989) 2149-2158.
- [62] J.C. Lippold, E.F. Nippes, and W.F. Savage, An Investigation of Hot Cracking in 5083-O Aluminum Alloy Weldments, *Welding Journal* 56 /1977), 171.
- [63] R.K. Sidhu, O.A. Ojo and M.C. Chaturvedi, Weld cracking in directionally solidified Inconel 738 superalloy, *Canadian Metallurgical Quarterly*. 46 (2007) 415-424.
- [64] Z. Guo, M.C. Chaturvedi, and N.L. Richards, Effect of nature of grain boundaries on intergranular liquation during weld thermal cycling of nickel base alloy, *Science and Technology of Welding and Joining* 3:5 (1998), 257-259.
- [65] R.G. Thompson, J.J. Cassimus, D.E. Mayo and J.R. Dobbs, The Relationship between grain size and microfissuring in Alloy 718. *Welding Journal* 64 (1985), 91-96.
- [66] A. Mostafa, I. Rubio, V. Brailovski, M. Jahazi and M. Medraj, Structure, Texture and Phases in 3D Printed IN718 Alloy Subjected to Homogenization and HIP Treatments. *Metals*7(6):196 (2017).
- [67] R.G. Thompson, B. Radhakrishnan, and D.E. Mayo, Intergranular liquid formation, distribution, and cracking in the HAZ of alloy 718 welds. *Superalloy 718 - Metallurgy and Applications* (1989), 437-455.

- [68] O.E. Oshobe, Fiber laser welding of nickel-based superalloy Inconel 718, Doctoral dissertation, University of Manitoba, Winnipeg, Canada, June 2012.
- [69] M.J. Donachie and S.J. Donachie, Superalloys: A Technical Guide, 2nd ed.; ASM International: Materials Park, OH, USA, 2002.
- [70] R. Seede, A. Mostafa, V. Brailovski, M. Jahazi and M. Medraj, Microstructural and Microhardness Evolution from Homogenization and Hot Isostatic Pressing on Selective Laser Melted Inconel 718: Structure, Texture, and Phases. *Journal of Manufacturing and Materials Processing* 2 (2018), 30.
- [71] T. Jokisch, A. Marko, S. Gook, Ö. Üstündag, A. Gumenyuk and M. Rethmeier, Laser Welding of SLM-Manufactured Tubes Made of IN625 and IN718. *Materials* 12(2019), 2967.
- [72] J. Andersson, J. Jacobsson and C.A. Lundin, A historical perspective on Varestraint testing and the importance of testing parameters. In *Cracking Phenomena in Welds IV*; Springer International Publishing: Basel, Switzerland, (2016), 3-23.
- [73] American National Standard Institute. ANSI Class 2 American Standard: ANSI/MC 96.1. Temperature Measurement Thermocouples; ANSI: New York, NY, USA, 1982.
- [74] J. Andersson, G. P. Sjöberg, L. Viskari, and M. Chaturvedi. Effect of different heat treatments on the hot ductility of superalloys; part 1 Alloy 718. *Materials Science and Technology* 29:1(2013).
- [75] M. Sadowski, L. Ladani, W. Brindley, and J. Romano, Optimizing quality of additively manufactured Inconel 718 using powder bed laser melting process. *Additive Manufacturing* 11(2016), 60-70.
- [76] V.S. Sufiiarov, E.V. Borisov and I.A. Polozov, Selective Laser Melting of the Inconel 718 Nickel Superalloy, *Applied Mechanics and Materials* 698 (2014), 333-338.
- [77] Y. Lu, S. Wu, Y. Gan, T. Huang, C. Yang, and L. Junjie, Study on the microstructure, mechanical property and residual stress of SLM Inconel-718 alloy manufactured by differing island scanning strategy, *Optics & Laser Technology*, 75:12 (2015), 197-206.

- [78] P. Hanzl, M. Zetek, T. Bakšá, and T. Kroupa, The influence of processing parameters on the mechanical properties of SLM parts, *Procedia Engineering* 100 (2015) 1405-1413.
- [79] C.A. Biffi, J. Fiocchi, P. Bassani and A. Tuissi, Continuous wave vs pulsed wave laser emission in selective laser melting of AlSi10Mg parts with industrial optimized process parameters: Microstructure and mechanical behaviour, *Additive Manufacturing* 24 (2018).
- [80] E. Assuncao and S. Williams, Comparison of continuous wave and pulsed wave laser welding effects, *Optics and Lasers in Engineering* 51 (2013) 674-680.
- [81] A.G. Demir, P. Colombo and B. Previtali, From pulsed to continuous wave emission in SLM with contemporary fiber laser sources: effect of temporal and spatial pulse overlap in part quality, *International Journal of Advanced Manufacturing Technology* 91:5 (2017) 2701-2714.
- [82] S. Kou, *Welding Metallurgy*, 2nd edition, New York: John Wiley, 2003.
- [83] Y. Tian, D. McAllister, H. Colijn, M. Mills, D. Farson, M. Nordin and S. Babu, Rationalization of microstructure heterogeneity in Inconel 718 builds made by the direct laser additive manufacturing process, *Metallurgical and Materials Transactions A* 45 (2014), 4470-4483.
- [84] P. Nie, O.A. Ojo and Z. Li, Numerical modeling of microstructure evolution during laser additive manufacturing of a nickel-based superalloy, *Acta Materialia* 77 (2014), 85-95.
- [85] L.L. Parimi, G.A. Ravi, D. Clark and M.M. Attallah, Microstructural and texture development in direct laser fabricated IN718, *Materials Characterization* 89 (2014), 102-111.
- [86] Y.N. Zhang, X. Cao, P. Wanjara and M. Medraj, Oxide films in laser additive manufactured Inconel 718, *Acta Materialia* 61 (2013) 6562-6576.
- [87] P.L. Blackwell, The mechanical and microstructural characteristics of laser-deposited IN718. *Journal of Materials Processing Technology* 170 (2005), 240-246.
- [88] V.P. Sabelkin, R.C. Gregory, T.E. Shelton, M.N. Hartsfield, D.J. Newell, R.P.O, Hara and R.A. Kemnitz, Mitigation of anisotropic fatigue in nickel alloy

718 manufactured via selective laser melting, *Materials and Design* 182 (2019) 108095.

[89] J.F. Radavich, The physical metallurgy of cast and wrought alloy 718, In *Superalloy 718 - Metallurgy and Applications*, Minerals, Metals & Materials Society (1989), 229-240.

[90] H.V. Atkinson and S. Davies, Fundamental aspects of hot isostatic pressing: an overview, *Metallurgical and Materials Transactions A* 31:12 (2000) 2981-3000.

[91] H. Song, Multi-scale microstructure characterization for improved understanding of microstructure-property relationship in additive manufacturing, Doctoral dissertation, The Ohio State University, 2016.

[92] J.J. Schirra, R.H. Caless and R.W. Hatala, The effect of Laves phase on the mechanical properties of wrought and cast + HIP Inconel 718, In *Superalloys 718, 625 and various derivatives. The minerals, metals & materials society* (1991), 375-388.

[93] R.C. Hall, The metallurgy of Alloy 718, *Journal of basic engineering* 89:3 (1967), 511-516.

[94] W. Huang, J. Yang, H. Yang, G. Jing, Z. Wang and X. Zeng. Heat treatment of Inconel 718 produced by selective laser melting: Microstructure and mechanical properties. *Materials Science & Engineering A* 750 (2019) 98-107.

[95] S. Singh and J. Andersson, Hot cracking in cast alloy 718, *Science and Technology of Welding and Joining* 23 (2018), 568-574.

[96] X. Huang, N.L. Richards and M.C. Chaturvedi, Effect of Grain Size on the Weldability of Cast Alloy 718, *Materials and Manufacturing Processes* 19 (2004), 285-311.

[97] A. Lingenfelter, Welding of Inconel alloy 718: a historical overview, In *Superalloy 718 Metallurgy and Applications*; The Minerals, Metals and Materials Society: Pittsburgh, PA, USA, 1989, 673-683.

- [98] X. Huang, M.C. Chaturvedi, N.L. Richards and J. Jackman, The effect of grain boundary segregation of boron in cast alloy 718 on HAZ microfissuring - A SIMS analysis), *Acta Materialia* 45:8 (1997), 3095-3107.
- [99] A. Segerstark, Laser Metal Deposition using Alloy 718 Powder: Influence of Process Parameters on Material Characteristics. Doctoral dissertation, University West, Trollhättan, Sweden, December 2017.
- [100] N.J. Harrison, I. Todd and K. Mumtaz, Reduction of micro-cracking in nickel superalloys processed by selective laser melting: a fundamental alloy design approach. *Acta Materialia* 94 (2015), 59-68.
- [101] J. Andersson, G. Sjöberg, L. Viskari and A. Bredeholm, Hot cracking of Allvac® 718Plus™, Alloy 718 and Waspaloy at Vareststraint testing. Proceedings of the 47th Conference of Metallurgists. Winnipeg: Aug 2008; 401-413.
- [102] J. Andersson, G. Sjöberg, A. Brederholm and H. Hänninen, Solidification cracking of Alloy Allvac 718Plus and Alloy 718 at transvareststraint testing. Proceedings of the 137th annual meeting of the minerals, metals and materials society. New Orleans: Mar 2008; 157-169.
- [103] H. Guo, M.C. Chaturvedi, N.L. Richards, and G.S. McMahon, Interdependence of Character of Grain Boundaries, Intergranular Segregation of Boron and Grain Boundary Liquation in Simulated Weld Heat-Affected Zone in Inconel 718, *Scripta Materialia* 40 (1999), 383.
- [104] O.A. Ojo and N. L. Richards, Heat affected zone cracking in welded Nickel superalloys, In *Welding and Joining of Aerospace Materials*, 2012.
- [105] M. Ni, C. Chen, X. Wang, P. Wang, R. Li, X. Zhang and K. Zhou, Anisotropic tensile behavior of in situ precipitation strengthened Inconel 718 fabricated by additive manufacturing, *Materials Science & Engineering A* 701 (2017) 344-351.
- [106] S.T. Mandziej, Testing for susceptibility to hot cracking on Gleeble™ physical simulator, In: Böllinghaus, Th.; Herold, H. (Eds.): *Hot cracking phenomena in welds*. Springer-Verlag, Berlin Heidelberg, 2005.
- [107] C.D. Lundin, C.Y.P. Qiao, T.P.S. Gill, and G.M. Goodwin, Hot ductility and hot cracking behavior of modified 316 stainless steels designed for high-temperature service, *Welding Journal*, 72 (1993) 189-200.

Appended Papers

Paper B

Varestraint weldability testing of additive manufactured alloy 718

B

Tahira Raza, Joel Andersson, Lars-Erik Svensson

**Published: Science and Technology of Welding and
Joining, 2018, vol. 23:7, pp. 606-611**

Printed with permission



Varestraint weldability testing of additive manufactured alloy 718

Tahira Raza, Joel Andersson & Lars-Erik Svensson

To cite this article: Tahira Raza, Joel Andersson & Lars-Erik Svensson (2018): Varestraint weldability testing of additive manufactured alloy 718, Science and Technology of Welding and Joining, DOI: [10.1080/13621718.2018.1437338](https://doi.org/10.1080/13621718.2018.1437338)

To link to this article: <https://doi.org/10.1080/13621718.2018.1437338>



Published online: 12 Feb 2018.



Submit your article to this journal [↗](#)



View related articles [↗](#)



View Crossmark data [↗](#)



Varestraint weldability testing of additive manufactured alloy 718

Tahira Raza , Joel Andersson  and Lars-Erik Svensson 

Department of Engineering Science, University West, Trollhättan, Sweden

ABSTRACT

The weldability in terms of susceptibility towards hot cracking of selective laser melted (SLM) Alloy 718 was investigated and wrought Alloy 718 was used as reference material. Varestraint testing was carried out by means of investigating the weldability in three conditions; (1) SLM as-built, (2) hot isostatic pressing at 1160°C at 105 MPa for 3 h and (3) wrought Alloy 718 in the mill-annealed condition. The material exhibited intergranular cracking in all three conditions; however, the SLM HIPed condition had an increased magnitude of crack susceptibility at all strain levels. The increased sensitivity of the HIPed material was due to the significantly larger grain size in comparison. The SLM as-built condition showed the same degree of cracking as the wrought material.

ARTICLE HISTORY

Received 20 December 2017
Accepted 1 February 2018

KEYWORDS

Weldability; selective laser melting; alloy 718

Introduction

Selective laser melting (SLM) is an additive manufacturing (AM) process for fabricating metallic parts by selectively melting fine powder particles using the laser. Production of near-net-shape complex geometries, minimum material wastage, and weight optimisation are some of the advantages of the technology. However, one drawback of the technology is that the dimensions of the SLM-manufactured objects are often quite limited due to the nature of the process and size of the production chamber. To be able to fully utilise the SLM process as a commercial production process, joining of small parts to build larger-sized or complex shaped components will be an issue. Since welding is the main joining method for metallic materials, the behaviour of SLM-manufactured material during welding is an important concern that needs to be investigated.

Alloy 718, in wrought and cast forms, is one of the most utilised superalloys in the aerospace industry and has been so for many years. Alloy 718 is an iron–nickel–base precipitation hardening superalloy that originally was developed to overcome issues with regard to strain age cracking during post-weld heat treatments, which at the time were faced in other alloys such as Waspaloy. On the other hand, the alloy suffers in terms of hot cracking during welding. These intergranular hot cracks form when liquid is present simultaneously with thermal contraction stresses. The source of the liquid in the heat-affected zone (HAZ) of Alloy 718 apart from melting point depressant elements is the constitutional liquation of Nb carbides in wrought and Nb carbides and Laves phase in cast form. Welding of cast Alloy 718 is more difficult than the wrought material because

of the inhomogeneous structure due to extensive interdendritic segregation of primarily Nb. In Alloy 718, the Nb is added to promote strengthening by gamma double prime (γ'') precipitation. Segregation of Nb leads to precipitation of Nb carbides and γ /Laves phase eutectic that resides in the interdendritic areas during solidification in processes such as casting, welding and AM [1–5].

SLM-manufactured Alloy 718 microstructure is similar to cast or welded microstructure but at a significantly smaller scale. According to previous studies [2,3], γ /Laves phase eutectic and fine MC carbides rich in Nb and Ti were detected in the interdendritic regions in SLM as-built Alloy 718. The microstructure of SLM parts that have been further processed by hot isostatic pressing (HIP) disclosed a change from columnar to equiaxed grain structure with Nb and Ti carbide precipitates homogeneously distributed within the matrix. Furthermore, it was also claimed that SLM as-built and SLM-HIPed Alloy 718 contained γ'' precipitates which contributed to a high hardness value in the material [3,4].

Since Alloy 718 accounts for a significant portion of all superalloy production and usage, an advanced production technology such as SLM is of high interest. Producing small parts and complex geometrical parts, using SLM and joining them to each other or to sheet or cast parts to fabricate larger structures can be a possibility to save weight and cost. However, the major challenge with this strategy will be to join the parts by welding and not least to deal with the concern related to hot cracking. Varestraint testing [6] is a weldability testing method, which enables studies on the materials

susceptibility towards hot cracking. Vareststraint testing is accomplished by applying a bending strain to produce cracking during actual welding [7]. In the present study, Vareststraint weldability testing has been utilised to investigate the hot cracking susceptibility of SLM as-built and SLM HIPed Alloy 718. Wrought Alloy 718 is used as reference material to compare the hot cracking susceptibility of SLM Alloy 718.

Experimental procedure

Test plates manufactured by the SLM process were 3.4 mm thick with dimensions 50×100 mm. They were present in two conditions, As-built and HIPed at 1160°C at 105 MPa for 3 h. The HIPed plates had an oxide layer on the surface. Therefore, they were machined before testing and were 3.3 mm thick. Reference plates made from wrought Alloy 718 sheet material with a thickness of 3.2 mm with dimensions 60×150 mm were used in the mill-annealed condition ($982^\circ\text{C} - 4.5$ min). The chemical composition for the gas-atomised (GA) powder used in the SLM of Alloy 718 and the wrought Alloy 718 are presented in Table 1.

The Vareststraint tests were conducted using the gas tungsten arc welding process with a welding current of 70 A, welding speed of 1 mm s^{-1} , and an arc length of 2 mm. The plates were bent with a stroke rate of 10 mm s^{-1} . The die mandrel radii used were 40, 60, 100, 200 and 300 mm, which led to augmented strains between 4 and 0.5%. The material thickness has been taken in account while calculating the augmented strain for each specimen. Three repetitions were made at each strain level. The SLM-manufactured samples were welded parallel to the building direction (Figure 1(a)). Total crack length (TCL), the length of all visible cracks in both HAZ and fusion zone (FZ), was used as the criteria for evaluating the cracking susceptibility.

The TCL was measured using a stereomicroscope. Cracks were not easily visible due to the oxidation after welding and therefore manual polishing (3- μm

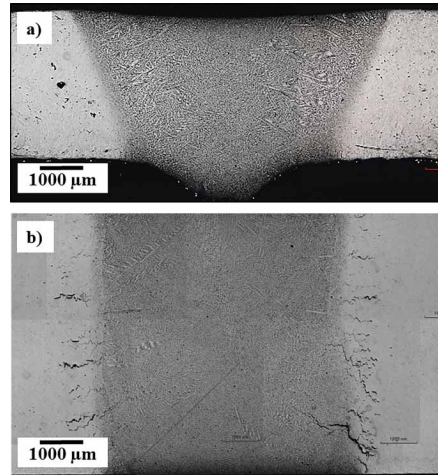


Figure 1. (a) Weld cross-section of SLM as-built and (b) weld top surface of SLM HIPed Alloy 718 tested at 4% augmented strain.

diamond suspension) was needed, followed by electrolytic etching with Oxalic acid according to standard methods. After measuring the TCL, samples were cut out from the plates for more in-depth microscopic investigations. Samples from weld cross-sections (Figure 1(a)), as well as specimens showing the top surface (Figure 1(b)) along the weld, were mounted, ground, polished and electrolytically etched with oxalic acid.

The grain size was measured according to ASTM E112-12. An optical microscope and a scanning electron microscope (SEM), equipped with a backscatter electron detector, was used for microstructural characterisation together with an Energy Dispersive Spectrometer (EDS) to analyse the chemical composition of the phases.

Results

The SLM as-built Alloy 718 exhibited columnar dendritic grain structure (Figure 2(a)). After HIP processing, the columnar microstructure was transformed into an equiaxed grain structure with enlarged grain size (Figure 2(b)). The wrought Alloy 718 showed an equiaxed grain structure (Figure 2(c)).

The SLM as-built specimen had an average grain length of $80 \mu\text{m}$ and width of $20 \mu\text{m}$ (Figure 2(a)). Grain size measurement of the SLM as-built specimens by the intercept method according to the ASTM standard resulted in an average grain size of $26 \mu\text{m}$. The SLM HIPed specimen had an average grain size of $60 \mu\text{m}$ (Figure 2(b)). The wrought Alloy 718 had an average grain size of $25 \mu\text{m}$ (Figure 2(c)). The microstructure

Table 1. Chemical composition of the GA Alloy 718 powder and wrought Alloy 718.

Element (Wt-%)	GA powder	Wrought
Ni	Bal.	Bal.
Cr	18.9	18.4
Fe	18.2	20.4
Nb	5.11	5.18
Mo	3.03	2.92
Ti	0.9	1.04
Mn	0.04	0.05
C	0.05	0.05
Al	0.48	0.38
Co	0.08	0.06
Si	0.04	0.07
Cu	0.02	0.01
B	< 0.006	0.003
Ca	< 0.01	—
Mg	< 0.01	—
P	< 0.015	0.008
S	< 0.01	0.0004

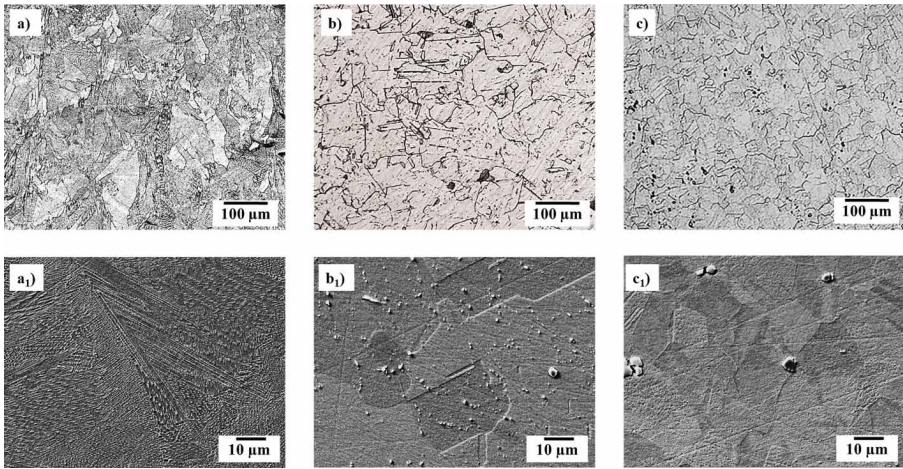


Figure 2. OM and SEM images of Alloy 718 plates used in the study; (a and a₁) SLM as-built, (b and b₁) SLM HIPed and (c and c₁) wrought.

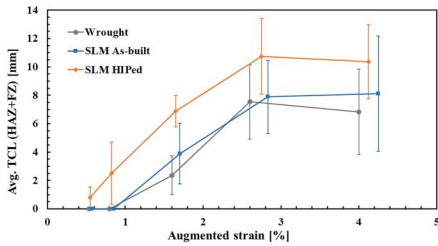


Figure 3. Average TCL in HAZ and FZ versus augmented strain of Alloy 718. Note the significant higher cracking susceptibility of the HIPed material.

of all three conditions contained various types of phases. In the SLM as-built (Figure 2(a₁)), the interdendritic regions were Nb-enriched. In SLM HIPed (Figure 2(b₁)) and wrought (Figure 2(c₁)), the MC type carbides were homogeneously distributed within the matrix. The size of carbides was smaller in SLM HIPed in comparison to the carbides in the wrought condition. EDS analysis showed that most of the phases mainly consisted of Nb and Ti.

The TCL versus augmented strain of the SLM as-built, SLM HIPed and wrought Alloy 718 in Varestraint testing is shown in Figure 3. The graph shows the susceptibility to form hot cracks, both in HAZ and FZ,

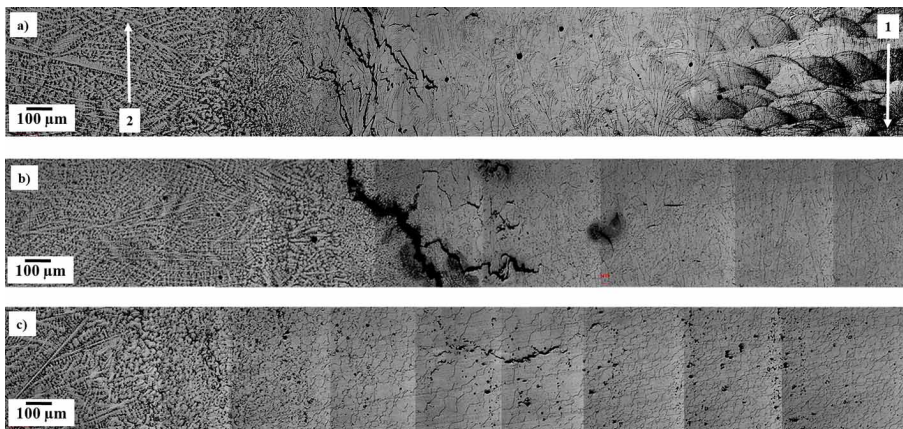


Figure 4. OM images of FZ, HAZ and base metal microstructure of (a) SLM as-built, showing (1) building direction of SLM-manufactured plates and (2) welding direction during Varestraint tests, (b) SLM HIPed and (c) wrought Alloy 718.

during welding. The magnitude of TCL is larger at every strain level in the HIPed condition. The threshold strain, i.e. the strain to initiate cracking was between 0.8 and 1.6% strain for the SLM as-built and wrought. A linear extrapolation of the curve showing results for HIPed condition predicts a threshold strain between ~ 0.4 and 0.6% for crack initiation. The saturated strain, i.e. the level of strain above that TCL does not change, was at 2.6% strain for all three conditions.

The crack appearances after the Vareststraint testing are shown in Figures 4 and 5 for all three material conditions. The cracks in the SLM as-built and HIPed material occurred in the HAZ and continued into the FZ. The hot cracking occurred in an intergranular manner and irregularly shaped constituents surrounded the cracks. EDS analysis of these constituents showed them to be Nb-rich. It was also seen that the width of

the cracks, in general, was larger in the HIPed condition in comparison to the as-built condition. Five cracks from each condition, tested at the largest augmented strain, were measured at the largest width for each crack (Figure 7(a)) and averaged together with the standard deviation to confirm this observation. As can be seen, the HIPed condition disclose a larger averaged crack width, $\sim 70\ \mu\text{m}$ (standard deviation of $37\ \mu\text{m}$), in comparison to the as-built condition having a crack width of $\sim 30\ \mu\text{m}$ (standard deviation of $9\ \mu\text{m}$).

The solidification structure of the weld FZ of SLM as-built Alloy 718 revealed γ /Laves phase eutectic and MC carbides as shown in Figure 6(a). Figure 6(b) shows HAZ of the material with liquated grain boundaries.

Figure 7 disclose the crack appearance in the HAZ of SLM as-built and HIPed conditions showing a mushy

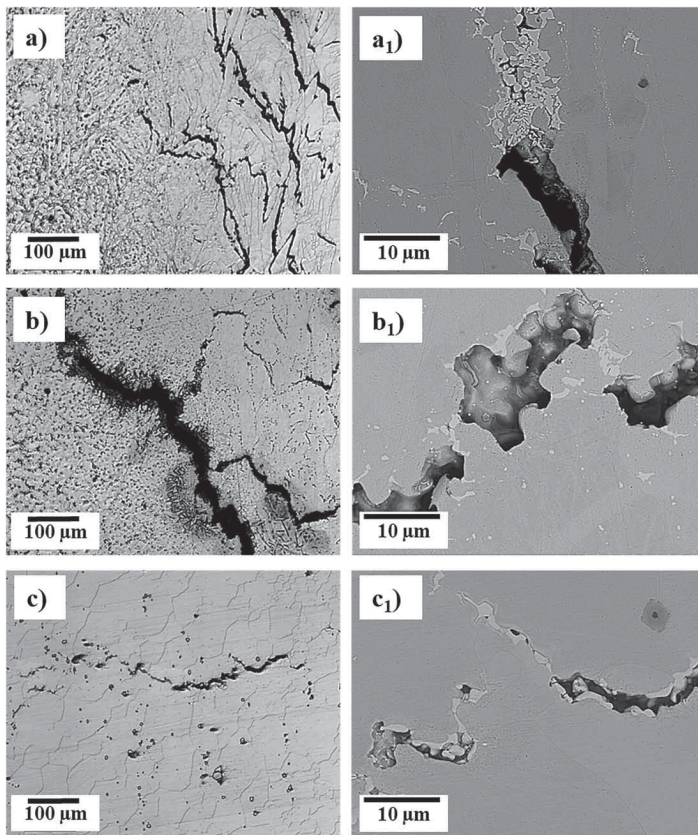


Figure 5. HAZ cracking in specimens tested at 4% augmented strain; (a and a₁) SLM as-built, (b and b₁) SLM HIPed and (c and c₁) wrought Alloy 718.

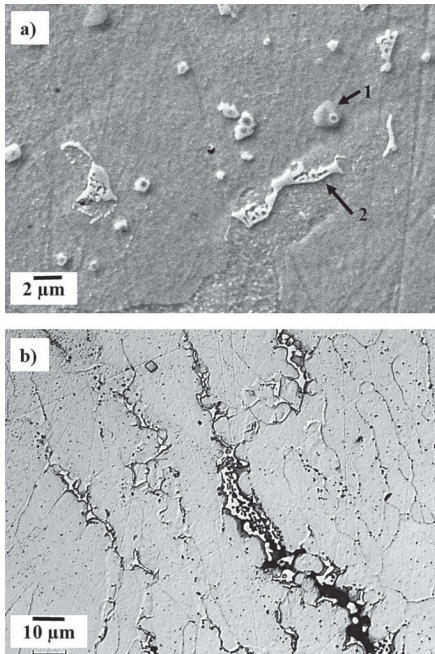


Figure 6. (a) SEM image of weld FZ showing (1) MC carbide, (2) γ /Laves phase eutectic and (b) OM image of HAZ showing liquated grain boundaries of the SLM as-built Alloy 718.

eutectic (presumably γ /Laves) constituent surrounding the intergranular cracks.

Discussion

The main parameter evaluated in this paper was the hot cracking susceptibility of SLM-manufactured Alloy 718 using the Varestraint testing. The SLM HIPed condition

had an increased degree of hot cracking at all the strain levels. This was further strengthened by the observation that the average crack width was larger in the HIPed material, as seen in Figures 4 and 5. The increased sensitivity was due to the larger grain size of the HIPed material. The grain boundaries of coarse grain size material are more prone to cracking because they have to accommodate larger localised strains compared to the material with smaller grain size [8,9]. This in turn increases the grain boundary sliding. Furthermore, less grain boundary area associated with coarse grain size results in more stress concentration applied to grain boundary triple points in which crack initiation is most likely to occur [8]. However, it should be pointed out that from the present work it is not possible to judge where crack initiation had taken place.

From the results in Figure 3, it seems like the SLM as-built specimens have the same cracking sensitivity as the reference wrought material and they also seem to have the same grain size. However, the as-built specimen had a columnar dendritic structure while the wrought material had equiaxed grains. Consequently, the grain size of the as-built material is quite small perpendicular to the growth direction. Thus, it would be expected that the as-built specimens should show even better crack resistance than the wrought material, but this was not confirmed by the measurements. On the other hand, by looking at Figures 4(a) and 5(a) it seems that the cracks to a large extent were following the vertical grain boundaries in the as-built sample. In the wrought material, the cracks followed horizontal grain boundaries (Figures 4(c) and 5(c)). Cracking in all three conditions occurred due to liquation mechanism [8] with irregularly shaped constituents surrounding the cracks. These constituents were Nb-rich and thus could be Nb carbides or γ /Laves phase eutectic [10]. The weld FZ of the SLM as-built condition revealed γ /Laves phase eutectic and MC carbides (Figure 6(a)), similar to that reported in the previous studies regarding weld

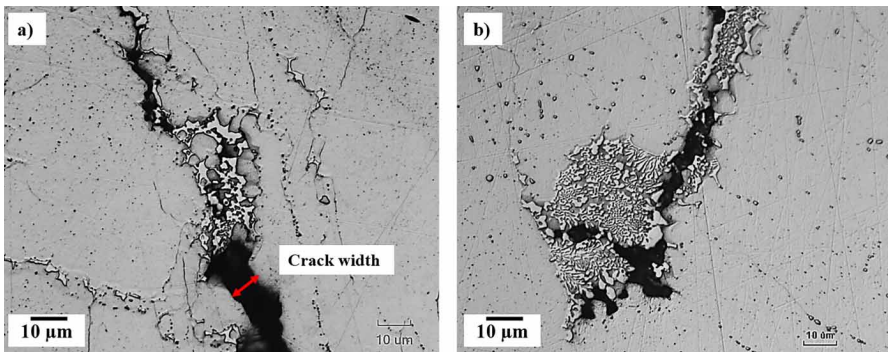


Figure 7. OM images of crack appearance in the HAZ of (a) SLM as-built and (b) HIPed Alloy 718. Arrow shows an exemplary sketch of crack width measurement.

FZ of wrought Alloy 718 [1,11]. In the HIPed material, cracks followed both vertical and horizontal directions (Figures 4(b) and 5(b)).

Conclusions

- Vareststraint testing was carried out by means of investigating the weldability in three conditions of Alloy 718; (1) SLM as-built, (2) HIP and (3) Wrought.
- The material exhibited intergranular cracking in all three conditions; however, the SLM HIPed condition had an increased magnitude of crack susceptibility at all strain levels.
- The increased susceptibility towards hot cracking of the SLM HIPed Alloy 718 was due to the larger grain size.
- The as-built SLM Alloy 718 showed the same degree of cracking as wrought Alloy 718.

Acknowledgements

We also acknowledge the support and input from GKN Aerospace Sweden AB. Special thanks to Kjell Hurtig and Kenneth Andersson at University West for their help in Vareststraint testing and SEM micrograph analysis.

Disclosure statement

No potential conflict of interest was reported by the authors.

Funding

The authors gratefully acknowledge the financial support from The Swedish National Space Board and VINNOVA (National Space Research Program and National Aerospace Research Program).

ORCID

Tahira Raza  <http://orcid.org/0000-0002-4598-4790>

Joel Andersson  <http://orcid.org/0000-0001-9065-0741>

Lars-Erik Svensson  <http://orcid.org/0000-0003-2560-0531>

References

- [1] Knorovsky GA, Cieslak MJ, Headley TJ, et al. Inconel 718: a solidification diagram. *Metall Trans A*. 1989 Oct;20A:2149–2158.
- [2] Chlebus E, Gruber K, Kuznicka B, et al. Effect of heat treatment on the microstructure and mechanical properties of Inconel 718 processed by selective laser melting. *Mater Sci Eng A*. 2015;639:647–655.
- [3] Mostafa A, Picazo Rubio I, Brailovski V, et al. Structure, texture and phases in 3D printed IN718 alloy subjected to homogenization and HIP treatments. *Metals (Basel)*. 2017;7:196.
- [4] Amato KN, Gaytan SM, Murr LE, et al. Microstructures and mechanical behavior of Inconel 718 fabricated by selective laser melting. *Acta Mater*. 2012;60:2229–2239.
- [5] Sims CT, Stoloff NS, Hagel WC. *Superalloys II*. New York (NY): John Wiley and Sons; 1987.
- [6] Savage WF, Lundin CD. The Vareststraint test. *Weld J*. 1965;44:433–442.
- [7] Andersson J, Jacobsson J, Lundin C. A historical perspective on Vareststraint testing and the importance of testing parameters. 4th International Hot Cracking Workshop, Berlin, Germany, 2014.
- [8] DuPont JN, Lippold JC, Kiser SD. *Welding metallurgy and weldability of nickel-base alloys*. Hoboken (NJ): John Wiley and Sons; 2009.
- [9] Thompson RG, Cassimus JJ, Mayo DE, et al. The relationship between grain size and microfissuring in Alloy 718. *WELD J*. 1985;64:91–96.
- [10] Andersson J, Sjöberg G, Viskari L, et al. Hot cracking of Allvac® 718Plus™, Alloy 718 and Waspaloy at Vareststraint testing. Proceedings of the Conference of Metallurgists. Winnipeg; Aug 2008; 401–413.
- [11] Andersson J, Sjöberg G, Brederholm A, et al. Solidification cracking of Alloy Allvac 718Plus and Alloy 718 at transvareststraint testing. Proceedings of the 137th annual meeting of the minerals, metals and materials society. New Orleans; Mar 2008; 157–169.

Paper D

Influence of Heat Treatments on Heat Affected Zone Cracking of Gas Tungsten Arc Welded Additive Manufactured Alloy 718

D




**Tahira Raza, Kjell Hurtig, Gbenga Asala, Joel Andersson, Lars-
Erik Svensson and Olanrewaju Akanbi Ojo**

Published: Metals, 2019, vol. 248:9, pp. 881

Printed with permission

Article

Influence of Heat Treatments on Heat Affected Zone Cracking of Gas Tungsten Arc Welded Additive Manufactured Alloy 718

Tahira Raza ^{1,*}, Kjell Hurtig ¹ , Gbenga Asala ², Joel Andersson ¹ , Lars-Erik Svensson ¹  and Olanrewaju Akanbi Ojo ²

¹ Department of Engineering Science, University West, 461 32 Trollhättan, Sweden

² Department of Mechanical Engineering, University of Manitoba, Winnipeg, MB R3T 5V6, Canada

* Correspondence: tahira.raza@hv.se; Tel.: +46-520-223334

Received: 28 June 2019; Accepted: 3 August 2019; Published: 10 August 2019



Abstract: The weldability of additive manufactured Alloy 718 was investigated in various heat-treated conditions. The microstructure of the base metal was examined in detail in order to understand the effect of different pre-weld heat treatments; i.e., solution, solution and aging, and hot isostatic pressing. After welding, the variation in total crack lengths, maximum crack length and the total number of cracks in the heat affected zone (HAZ) were used as criteria for the cracking susceptibility of each material condition where wrought Alloy 718 was used as the reference material. Selective laser melting (SLM) manufactured Alloy 718 was susceptible to HAZ cracking in all material conditions. Total crack lengths in HAZ were highest in the SLM as-built condition and lowest in the SLM hot isostatic pressed condition. The cracks that were found in the HAZ of the welded materials consisted of liquation cracks, with eutectic product surrounding the cracks, as well as cracks from which liquation products were absent.

Keywords: selective laser melting; Alloy 718; heat treatments; gas tungsten arc welding; heat affected zone cracking

1. Introduction

Selective laser melting (SLM) is an additive manufacturing (AM) process for fabricating near net shape parts using fine metal powders. SLM systems utilize a laser to selectively melt a bed of metallic powder layer by layer to build the physical part. The SLM process shows potential to produce functional metallic parts with complex geometries that cannot easily be produced by conventional processes [1]. However, the production of parts with SLM is limited by the size of the production chamber. Hence, production of large components, such as turbine structures for aero engines, will require joining different small SLM-manufactured parts together by welding. Furthermore, the SLM process can also be used to produce replacements of damaged or worn-out parts, which can subsequently be welded to the components.

Alloy 718 is an iron–nickel base precipitation hardening superalloy that is used in hot structural parts of gas turbine engines due to its combination of high strength and corrosion resistance at elevated temperature. The alloy exhibits resistance to strain-age cracking (SAC) during post-weld heat treatment (PWHT) and can therefore be used in applications that require welding. The microstructure of the alloy consists of a γ -matrix dispersed with precipitates including γ'' (Ni₃Nb), γ' [Ni₃(Al, Ti)], δ -phase (Ni₃Nb), Laves phase [(Ni, Fe, Cr)₂(Nb, Mo, Ti)], and various metal carbides and nitrides, such as NbC, TiC, and TiN. The main strengthening phase in the alloy is γ'' that is formed due to the addition of about 5 wt. % niobium (Nb) [2]. As has been long-known, the presence of NbC and Laves phase in Alloy

718 can contribute to hot cracking in the heat-affected zone (HAZ) during welding [3–6]. The overall microstructure of a material, including existing phases, their morphology, and distribution is directly related to the manufacturing process and subsequent post-processing conditions. Typically, Alloy 718 is utilized in either wrought or cast condition followed by post-processing to generate the optimized microstructure for the specific use or application. Previous studies regarding the weldability of Alloy 718 in cast and wrought forms, have shown that the extent of HAZ liquation cracking can be influenced by the pre-weld heat treatment. Researchers have concluded that solution heat treatment can reduce cracking susceptibility [7] in Alloy 718 and age hardening can increase it [8]. That is why the usual procedure within industry is to weld the alloy in the solution-annealed condition and then subject it to solution and aging heat treatment after welding. The solution heat treatment relieves the residual stresses after the welding process and the aging heat treatment develops the strengthening phases. However, in some cases, such as repair welding, the alloy needs to be welded in aged condition.

The microstructure of SLM-manufactured Alloy 718 in the as-built condition is more similar to cast material (although on a much finer scale) or the fusion zone (FZ) of welded Alloy 718 than to wrought material. The grains have a dendritic structure and are mostly oriented in the building direction of the component. The microstructure contains NbC carbides and low melting Laves phase in the interdendritic regions and along the grain boundaries.

In an early study from 1966 regarding HAZ cracking in the nickel-based superalloys, Owczarski et al. [9] reported that constitutional liquation was initiated in the vicinity of MC-type carbides (where M is principally Nb but can also contain Ti). They suggested that the abrupt decomposition of these particles occurred during rapid heating, leading to constitutional liquation, grain boundary wetting, and subsequent cracking. They also found that, during rapid heating, a partially melted zone (PMZ) was formed in the welded alloy by constitutional liquation reactions involving the decomposition of MC-type carbide particles. The PMZ is the area immediately outside the weld metal FZ [9,10], and the main characteristic of this area is the presence of a liquid fraction that forms when the temperature exceeds the solidus temperature during heating. The formation of stresses in the PMZ, during subsequent weld cooling, can cause crack formation. Baeslack and Nelson [3] studied the HAZ liquation cracking in cast Alloy 718 and concluded that melting of the Laves phase in the interdendritic regions promoted liquation cracking in the HAZ. The Laves phase forms during the terminal solidification of casting, and simply re-melts in the HAZ during welding. On the other hand, NbC decompose during rapid heating and promote constitutional liquation cracking in both wrought and cast Alloy 718 [4,8]. Due to the high-volume fraction of Laves phase present in cast Alloy 718, liquation can be extensive, resulting in increased cracking sensitivity relative to the wrought counterparts.

The physical and chemical reactions in the HAZ of the welded samples are related to the thermal process that occurs during welding. Metallurgical reactions, phase transformations, and recrystallization of grains are closely related to this thermal process. The thermal cycle imposed on the HAZ greatly influences the degree of constitutional liquation, precipitate dissolution, and grain boundary segregation that can occur. All these factors influence the amount of liquid that forms along the PMZ grain boundaries. By measuring the temperature distribution and cooling rate in the HAZ using implanted thermocouples, it is possible to determine the thermal crack susceptible region surrounding the weld within which HAZ liquation cracking is possible.

In the present investigation, the susceptibility towards hot cracking during gas tungsten arc welding (GTAW) of SLM-manufactured Alloy 718 was investigated in various heat-treated conditions. Wrought Alloy 718 was used as the reference material. The temperature distribution in the HAZ was also measured in order to obtain increased insight into the type of cracking occurring in the material. Additionally, possible reasons for HAZ cracking in welded SLM manufactured material are discussed.

2. Materials and Methods

2.1. Material and Heat Treatments

The SLM-manufactured plates were built with a Realizer SLM125 system with a build chamber of $125 \times 125 \times 180 \text{ mm}^3$ and a 200 W SPI Ytterbium fiber laser (Realizer GmbH, Borchten, Germany) with laser beam spot diameter of 20 μm . Powder with a particle size distribution from 15 to 45 μm , supplied by LPW Technology UK, was utilized for the processing of the samples. The thickness of the deposited powder layer was set to 60 μm in this study. The fabrication was conducted in a chamber that was filled with argon gas to maintain the oxygen level below <1000 ppm.

Test plates manufactured by the SLM process were 3.4 mm thick with dimensions of 50 mm in width and 100 mm in length. The plates had a rough surface and were therefore machined to 3.3 mm thickness before welding. Reference plates made from wrought Alloy 718 sheet material had a thickness of 3.2 mm with dimensions of 60 mm in width and 150 mm in length and were tested in the mill-annealed condition (mill annealing is a heat treatment given to all mill products to increase material ductility, reduce hardness, and make them workable). The chemical composition, in weight % (wt. %), for the gas-atomized (GA) powder used in the SLM of Alloy 718 is presented in Table 1, together with the chemical composition for wrought Alloy 718. The SLM-manufactured plates were tested in four different conditions: as-built, solution heat-treated (SHT), solution heat-treated and aged (SHT + AGE), and hot isostatic pressed (HIP). The heat treatments performed on the specimens are specified in Table 2. The mill-annealed condition refers to the wrought alloy.

Table 1. Chemical composition of the gas-atomized (GA) Alloy 718 powder and wrought Alloy 718. (wt. %).

Element	GA Powder	Wrought
Ni	Bal.	Bal.
Cr	18.9	18.4
Fe	18.2	20.4
Nb	5.11	5.18
Mo	3.03	2.92
Ti	0.9	1.04
Mn	0.04	0.05
C	0.05	0.05
Al	0.48	0.38
Co	0.08	0.06
Si	0.04	0.07
Cu	0.02	0.01
B	<0.006	0.003
Ca	<0.01	-
Mg	<0.01	-
P	<0.015	0.008
S	<0.01	0.0004

Table 2. Test plate conditions.

Heat Treatment/Condition	Specification
As-built	SLM manufactured without any heat treatment
SHT	954 °C–1 h
SHT + Aging	954 °C–1 h + 760 °C–5 h + 649 °C–1 h
HIP	1160 °C–105 MPa–4 h
Mill-annealed	982 °C–4.5 min

2.2. Temperature Distribution Tests

In the present study, the temperature measurement was implemented using K-type thermocouples with 0.2 mm wire diameter. Type-K thermocouples have a measuring range from $-200\text{ }^{\circ}\text{C}$ to $1250\text{ }^{\circ}\text{C}$ [11]. They have an accuracy of $\pm 0.75\%$ which translates to around $\pm 9.5\text{ }^{\circ}\text{C}$ at $1250\text{ }^{\circ}\text{C}$. However, the melting temperature of the thermocouple is $1300\text{ }^{\circ}\text{C}$ which is fairly close to the melting temperature of Alloy 718 which is $\sim 1335\text{ }^{\circ}\text{C}$ [12].

The weld piece had a thickness of 3.2 mm with dimensions of 60 mm in width and 150 mm in length. Thermocouples were positioned and affixed by electrical spot welding. Figure 1 shows the thermocouple locations on the test piece. The GTAW method was used for welding one bead-on-plate pass. Temperatures were measured at different distances from both sides of the weld line. To record the measured temperatures, the collected signals were transferred to a data logger and a computer. LabVIEW 2015 32 bit (NXG, National Instruments Sverige AB, Kista, Sweden) was used to display the thermal curves.

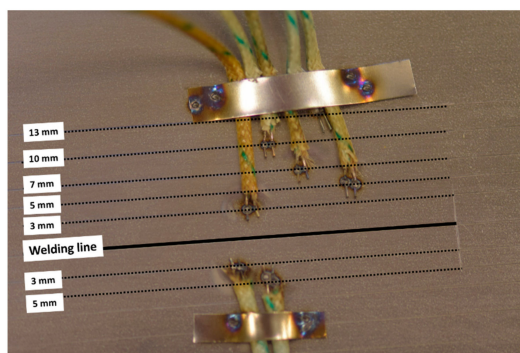


Figure 1. Position of thermocouples regarding the distance from the welding bead. Thermocouples were spot welded on the sample at distances of 3, 5, 7, 10, and 13 mm from the weld line.

2.3. Welding Conditions, Sample Preparation, and Microscopic Examination

Bead on plate welding was carried out on the materials using an automatic GTAW process. Argon was used as a shielding gas, with a flow rate of 15 L/min. The welding parameters used were welding speed of 1 mm/s, welding current of 70 A, and arc voltage of 10 V. The welding parameters are based on a DOE (Design of Experiments) study which produced the lowest average total crack length and lowest standard deviation among different settings [13].

Five cross sections from each condition of the welded plates were excised for the measurements of total crack length (TCL), maximum crack length (MCL), total number of cracks, and in-depth microscopic investigations. Samples from weld cross sections were mounted, ground, and polished. TCL were first measured by taking images of all the cracks in the cross-sections with a Hitachi TM3000 tabletop scanning electron microscope (SEM) (Hitachi, Ltd., Tokyo, Japan) and then by measuring the cracks with a Lumenera Infinity Analyze 6.5 software (Version 6.5, Lumenera Corporation, Ottawa, ON, Canada). For further microscopic examination of cracks, the samples were electrolytically etched with oxalic acid. Additional SEM examination of the material and HAZ microstructure was performed on a Zeiss SEM EVO 50 (Carl Zeiss AB, Oberkochen, Germany) and a FEI Nova NanoSEM 450 (FEI Company, Hillsboro, OR, USA), equipped with a high-resolution field emission gun. To be able to see the precipitation hardening phases in the base metal, particularly in the SHT + AGE condition, the samples were electrolytically etched with phosphoric acid. Semi-quantitative SEM/EDS analyses were also performed to obtain approximations of elemental composition and concentrations.

Transmission electron microscopy (TEM) was performed on a FEI Talos F200X TEM (FEI Company, Hillsboro, OR, USA) equipped with a Super-X EDS system. Thin foils of base metal for TEM study were ground, polished to about 100 μm , and punched out in 3 mm coupons before subjecting them to dimpling and electro-polishing. The electro-polishing was performed using a Struers TenuPol-2 Twin-jet polisher (Struers Inc., Cleveland, OH, USA) in a solution of 10% perchloric acid and 90% methyl alcohol, at a temperature of around $-40\text{ }^{\circ}\text{C}$, a voltage of 1.5 V, and 1.0 A DC current.

Microhardness, HV1 (9.807 N) 15 s, was measured for each of the five material conditions using a Shimadzu HMV-2 microhardness tester (Shimadzu Scientific Instruments, Kyoto, Japan). Ten readings were recorded for each material condition and the average was determined as the hardness value.

3. Results

3.1. Base Metal Microstructure

The microstructure of all five conditions of the base metal are presented in Figures 2–6. The secondary phases observed in the microstructure were examined by SEM and TEM. The chemical composition of the phases present was determined by EDS analyses and these are summarized in Table 3. The chemical compositions included in the table are the average of five measurements. Phases were tentatively identified by their unique characteristic morphologies and by their chemical compositions.

In the as-built condition in Figure 2a, a dendritic solidification structure with particles along the interdendritic region can be seen. As shown in the SEM image in Figure 2b, the as-built condition disclosed significant segregation, with the lighter regions being the interdendritic area. The TEM/EDS analyses (Table 3) suggested that the lamellar and the irregular-shaped particles were associated with Laves phase and MC-type carbides, respectively. More in-depth analyses by TEM were performed to confirm the nature of the particles. The bright field (BF) image in Figure 2c shows Laves phase and NbC carbide along the interdendritic regions. The inset shows the diffraction pattern (DP) of Laves phase in the γ -matrix.

After solution heat treatment (SHT) at $954\text{ }^{\circ}\text{C}$ for 1 h, the dendritic structures within the grains were still present (Figure 3a), along with MC-type carbides, remnants of Laves phase, and plate-like δ -phase (Ni3Nb) (Figure 3b) present in the microstructure.

After the SHT followed by a two-step aging treatment (5 h at $760\text{ }^{\circ}\text{C}$ and 1 h at $649\text{ }^{\circ}\text{C}$), δ -phase and carbides still remained in the microstructure, along with the precipitated strengthening phases of γ' and γ'' in the matrix (Figure 4a,b). The TEM BF image and DP in Figure 4c show the presence of strengthening precipitates γ'' . The dark field image in Figure 4d is the same area as in Figure 4c, and DP confirms the presence of γ' precipitates in the γ -matrix. In Figure 4e, δ -phase forming from the Laves phase can be seen. In Figure 4f, δ -phase and carbide residing on the grain boundaries can be seen. TEM/EDS analyses also confirmed the presence of these phases.

After HIP treatment of the as-built specimens, the dendritic structure from the SLM processing disappeared and the grains grew into a coarser and equiaxed grain structure (Figure 5). The Laves phase was totally dissolved but residual NbC carbides were observable in the microstructure. The TEM BF image and DP confirm the presence of carbides in the matrix.

The microstructure of wrought Alloy 718 consisted of equiaxed grains, with NbC carbides mostly residing on the grain boundaries (Figure 6).

Table 3 presents the values from the EDS analyses determining the chemical composition of the different phases from the as-built, SHT, SHT + AGE, and HIP conditions.

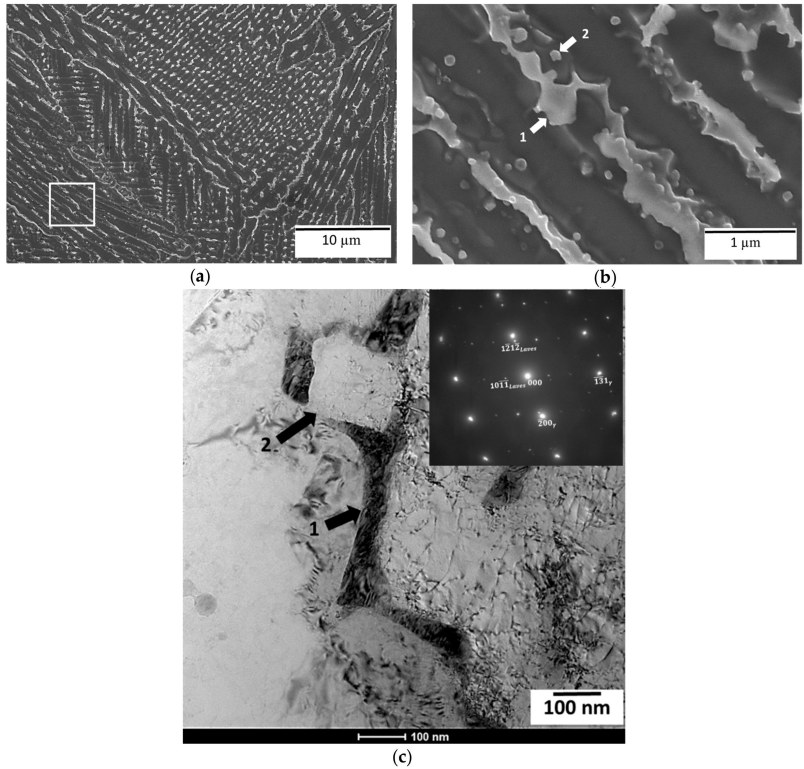


Figure 2. (a) Microstructure of as-built condition (electrolytically etched with phosphoric acid); (b) interdendritic regions in as-built condition showing (1) Laves phase and (2) MC-type carbide; and (c) bright field image of (1) Laves phase and (2) NbC carbide. The inset shows the diffraction pattern of Laves phase in γ -matrix.

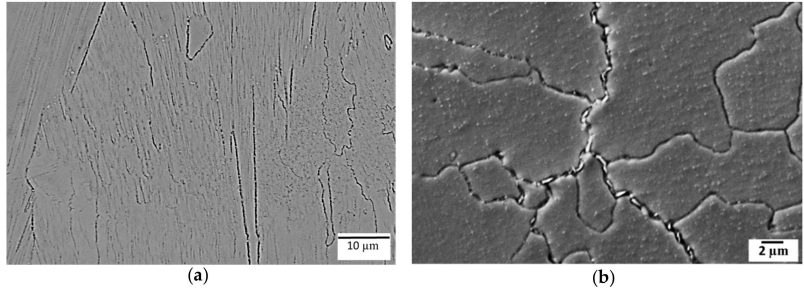


Figure 3. (a) Microstructure of solution heat-treated (SHT) condition (electrolytically etched with oxalic acid), showing (b) precipitates residing in the grain boundaries and matrix.

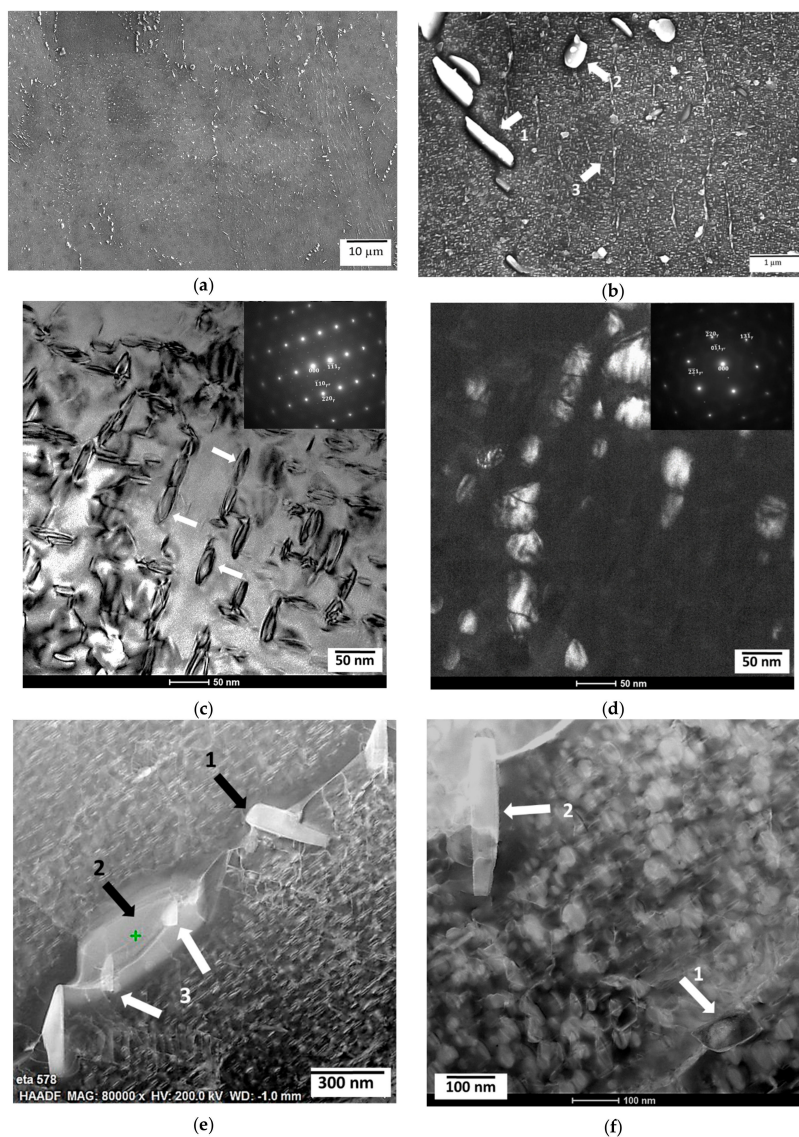


Figure 4. (a) Microstructure of solution and aged heat treated (SHT + AGE) condition showing (b) (1) delta phase, (2) MC-type carbide, and (3) matrix with strengthening phases γ' and γ'' (electrolytically etched with phosphoric acid); (c) bright field image of γ'' (marked with white arrows), the inset shows the diffraction pattern of γ'' in γ -matrix; (d) dark field image of same area as (c), showing γ' (white particles), the inset shows the diffraction pattern of γ' in γ -matrix; (e) TEM HAADF image showing (1) δ -phase residing on the grain boundary; (2) Laves phase, and (3) δ -phase forming from the Laves phase; and (f) TEM HAADF image of (1) NbC and (2) δ -phase residing on the grain boundary.

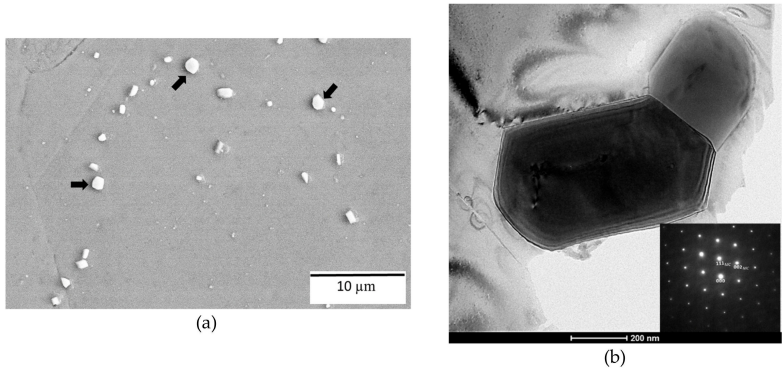


Figure 5. (a) Microstructure of HIP condition disclosing equiaxed grain structure and NbC carbides marked with arrows (electrolytically etched with oxalic acid), and (b) bright field image of carbide in HIP condition; the inset shows the diffraction pattern of carbide.

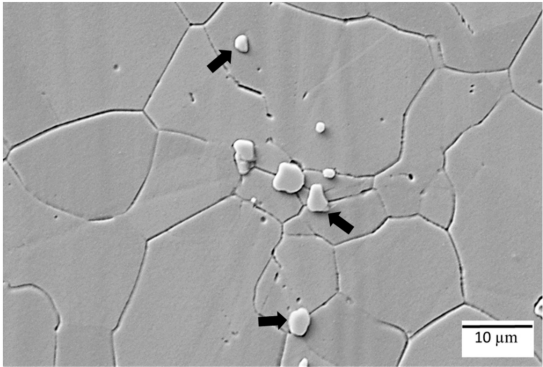


Figure 6. Microstructure of wrought Alloy 718 showing equiaxed grain structure and NbC carbides marked with arrows (electrolytically etched with oxalic acid).

Table 3. Chemical composition of the phases, detected in all selective laser melting (SLM) conditions, determined by the Transmission electron microscopy (TEM/EDS) and Scanning electron microscope (SEM/EDS) analyses.

Material Condition	Phases	Elements (wt. %)						
		Ni	Fe	Cr	Nb	Mo	Ti	Al
SLM-As-Built (TEM/EDS)	Laves	41	12	14	23	5	1	0.3
	Carbide	2	1	1	84	5	8	0.1
SLM-SHT (SEM/EDS)	Laves	43	15	17	19	3	2	0.5
SLM-SHT + AGE (TEM/EDS)	Laves	58	15	15	11	4	1	0.5
	δ-phase	68	3	3	24	3	2	0.6
	Carbide	2	0.4	1	82	5	12	0.1
SLM-HIP (TEM/EDS)	Carbide	2	1	1	81	5	10	0.5

3.2. Hardness Measurements

Table 4 shows the measured hardness values in all conditions of base metal. The SLM as-built and SHT conditions had relatively higher hardness even though both are assumingly free from strengthening phases of γ'' and γ' . The SHT + AGE condition had the highest hardness of all due to the precipitation of the hardening phases, i.e., γ'' and γ' .

Table 4. Microhardness (HV1-15 s) values of different conditions of the material. Average of 10 indents.

As-Built	SHT	SHT + AGE	HIPed	Wrought
300 ± 5	280 ± 4	470 ± 7	280 ± 9	230 ± 6

3.3. Temperature Measurements

Figure 7a shows a weld cross section of a welded sample, and Figure 7b presents the peak temperatures recorded from the respective thermocouples in the material during the welding process as a function of distance from weld centre line. Figure 7c shows the FZ, PMZ, and HAZ of the welded sample, and the distance of these zones from the weld centre line.

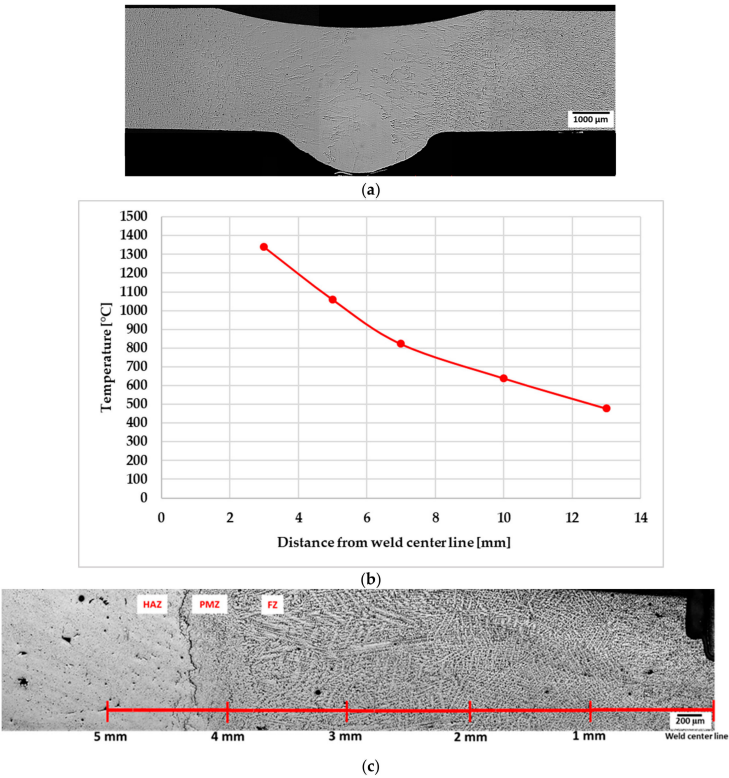


Figure 7. (a) Cross section of a welded sample; (b) peak temperatures as a function of distance from weld center line; and (c) fusion zone (FZ), partially melted zone (PMZ), and heat affected zone (HAZ) of the welded sample, and the distance of these zones from the weld center line.

3.4. HAZ Cracking Susceptibility

The concept of weldability in this study was considered as the ability to resist HAZ cracking during GTAW. The welded specimens were cut into sections perpendicular to the welding direction (Figure 7a). The cracking tendency after different heat treatments was evaluated using TCL, MCL, and total number of cracks in the welded samples. TCL is the summation of all crack lengths and MCL is the length of the longest crack observed in the HAZ of welded samples. Averages of the TCL, MCL, and total number of cracks from five samples of each material condition were used as the criteria for cracking susceptibility in the HAZ (Figure 8). SLM-manufactured Alloy 718, in the as-built condition, was most susceptible to HAZ cracking. Cracking susceptibility, however, decreased after SHT, and decreased further in the SHT + AGE samples. In samples subjected to HIP directly after the SLM process, the cracking susceptibility was similar to that of wrought Alloy 718. The average MCL was highest in the SLM as-built condition and decreased with SHT. A further decrease was observed in the SHT + AGE condition. In the SLM-HIP condition, the MCL was similar to that of the MCL in the wrought condition. The total number of cracks was highest in the HIP and wrought conditions because there was a higher number of smaller cracks in these two conditions. Figures 9–13 show evidence of grain boundary liquation in the HAZ of all the material conditions used in the present study. Figure 11 also shows an example of a “clean” crack without any apparent liquation product.

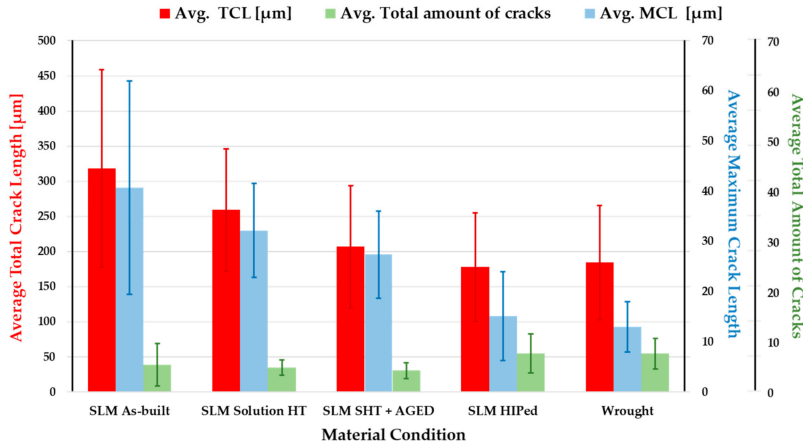


Figure 8. Heat affected zone (HAZ) cracking susceptibility of SLM-manufactured Alloy 718 in comparison with wrought Alloy 718, presented as the average of total crack length measurements, average of maximum crack length, and total number of cracks (for five observations, with standard deviations).

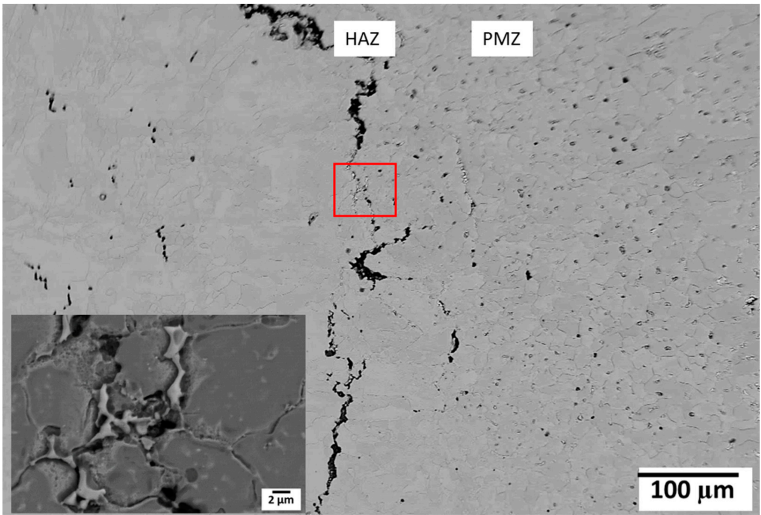


Figure 9. HAZ liquation cracking in SLM as-built condition; inset showing the marked area.

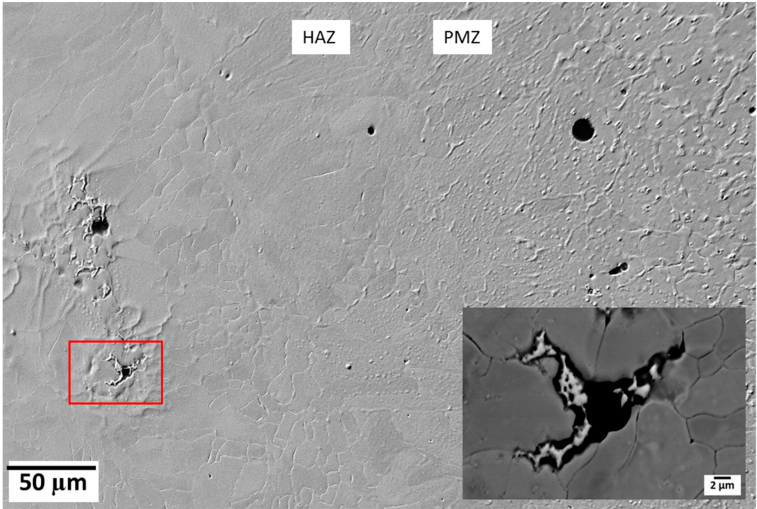


Figure 10. HAZ liquation cracking in SHT condition; inset showing the marked area.

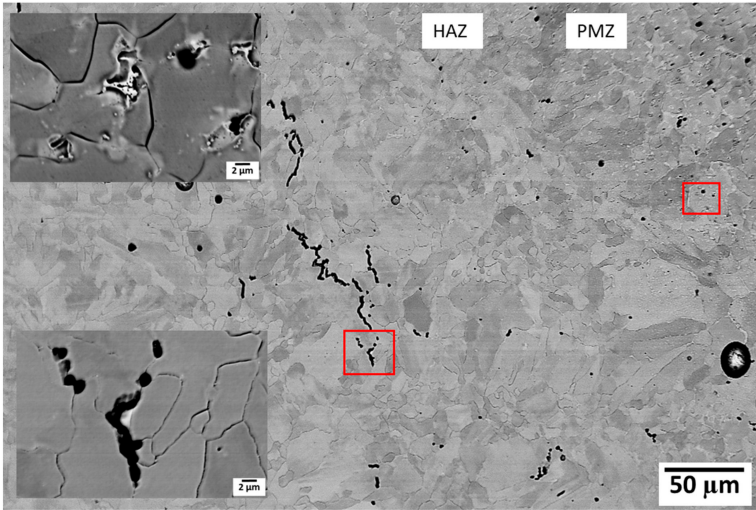


Figure 11. HAZ of welded SHT + AGE material showing microfissure with liquation product in PMZ, and an example of grain boundary cracking without any visible liquation in the HAZ; insets showing the marked areas.

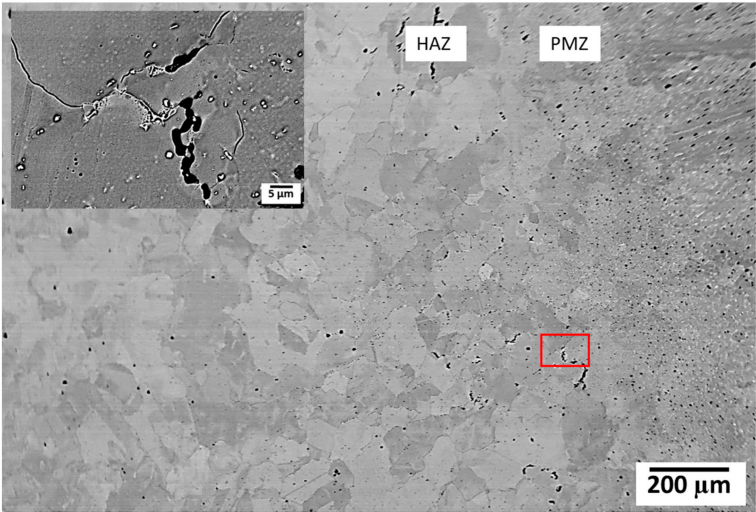


Figure 12. Liquation at grain boundaries causing cracking in HAZ of SLM-manufactured and HIP Alloy 718; inset showing the marked area.

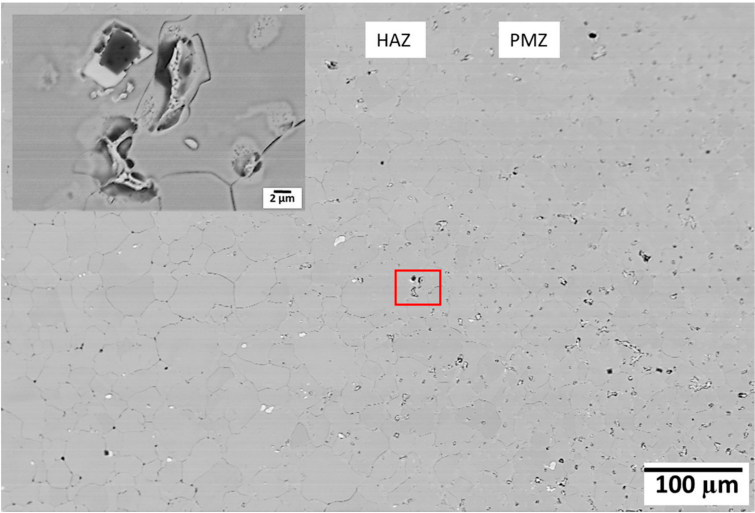


Figure 13. Liquation cracking in HAZ of wrought Alloy 718; inset showing the marked area.

4. Discussion

In the present study, the weldability of the SLM-manufactured Alloy 718 was investigated in different heat-treated conditions. The definition of weldability was here considered as the susceptibility towards hot cracking in the HAZ. The SLM-manufactured samples were mainly compared to wrought Alloy 718 of approximately the same thickness as the SLM samples. However, some comparisons to a cast Alloy 718 sample were also made. By comparing the microstructure of the different manufacturing techniques, it is obvious that SLM-manufactured Alloy 718 in the as-built condition (Figure 14a) is very different from the wrought form (Figure 14b), but somewhat more similar to the cast form (Figure 14c), however, on a much finer scale. The different scale bars in Figure 14 should be noted. The fine scale of the SLM microstructure is due to the rapid solidification of the molten pool during the SLM process (compare Figure 14a,c).

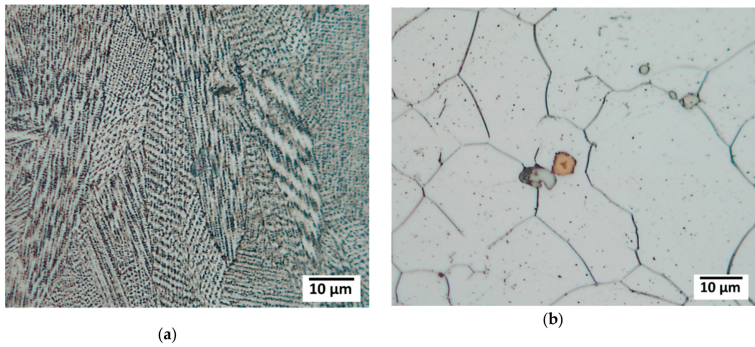
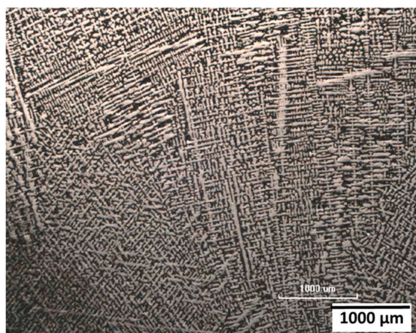


Figure 14. Cont.



(c)

Figure 14. Microstructure of (a) SLM as-built, (b) wrought, and (c) cast, Alloy 718.

Regarding weldability, all five material conditions examined in the present study appeared to experience the same process of HAZ liquation cracking. Presumably, the cause of the liquation could be different in different conditions. Microstructural examination suggested that in the SLM as-built, SHT, and SHT + AGE condition, incipient melting of Laves phase could be the cause of HAZ liquation cracking. This can be rationalized according to the literature regarding the HAZ liquation cracking in cast Alloy 718 that also contains Laves phase. On the other hand, by direct HIP of the SLM-manufactured Alloy 718 at 1160 °C for 4 h, the Laves phase was totally dissolved and carbides were apparently present in the microstructure. There were fewer cracks in the HAZ of the material and the average TCL was almost the same as in the wrought condition.

The argument proposed in the previous paragraph is reasonable due the fact that, in as-built condition, an extensive amount of Laves phase was present and the TCL was highest. The TCL decreased when the amount of Laves phase decreased in the SHT condition and a further decrease could be seen in the SHT + AGE condition where the amount of Laves was even lower than in the SHT condition. Direct HIP of the SLM-manufactured Alloy 718 dissolved all the Laves phase and carbides seemed to remain in the matrix. The average total number of cracks presented in Figure 8 also indicated the transition from fewer but longer cracks in the as-built condition, to shorter but more cracks in the HIP condition. This observation also supports the notion that less availability of low melting constituents in the matrix favors less cracking in the HAZ.

The grain size is another factor to be considered while discussing the weldability of the materials. It has generally been recognized that fine-grained materials are more resistant to HAZ liquation cracking than are coarse-grained versions of the same material [14]. Grains in the SLM-manufactured material were fine and elongated (Figure 14a). Grain size measurements performed in a previous study [15] showed that the SLM as-built specimen had an average grain length of 80 μm and width of 20 μm. The wrought Alloy 718 had an average grain size of around 25 μm. Grain size of the cast material is not clearly shown in Figure 14c, but another study [16] regarding hot cracking in cast Alloy 718, showed that the average grain size of as cast base metal was around 1700 μm. Thus, it could be expected that SLM-manufactured material in the as-built condition and wrought material would have similar cracking sensitivity, while as cast material would be much worse. However, this was not the case in the present study because the as-built condition had more cracks than the wrought.

In all SLM conditions in the present study, “clean” cracks, i.e., cracks without any eutectic formation, were also observed (for example, Figure 11). These cracks were in the HAZ where the temperature range during welding was between 1150 and 1200 °C (Figure 7a,b). The question is whether this has to do with any other cracking mechanism, for example segregation of elements such as B, P, C, or S in the grain boundaries [2,6,17]. According to the literature [18–20], B causes increased

HAZ cracking sensitivity if present much above 0.003 wt. %. B in the powder feedstock used for the manufacturing of Alloy 718 with SLM process in the present study, was around 0.006 wt. % and was 0.003 wt. % in wrought Alloy 718. This could also be a reason for the higher cracking susceptibility of SLM material. This phenomenon requires further study for SLM-manufactured Alloy 718.

Another possible reason for relatively high cracking susceptibility in SLM material could be that the microcracks have already been created during the SLM process. Several nickel-base superalloys have been documented as being particularly susceptible to microcracking when processed by laser additive manufacturing process [21,22]. These microcracks can act as crack initiating sites during the cooling process after welding due to the local stresses in the material. HIP can be used to consolidate cracks; however, surface cracks and open porosity remain [23]. Furthermore, HIP can cause grain coarsening in the material (Figure 5a) that can also be an issue while welding. Each production process introduces some amount of residual stress [24]. Laser-based processes, such as laser welding and SLM, are known to introduce a huge amount of residual stress due to the large thermal gradients [25]. These process-induced residual stresses in SLM material can also influence the cracking behaviour when combined with complex welding stresses. Post-process stress-relieving heat treatments and solution heat treatment can decrease the amount of residual stress in the SLM material [26], which subsequently can reduce the cracking susceptibility of the material.

5. Conclusions

The present study investigated the influence of different heat treatments on the microstructure and weldability of selective laser melted Alloy 718. The gas tungsten arc welding method was used for welding of the samples. The following conclusions were drawn from the study:

- SLM-manufactured Alloy 718 was susceptible to HAZ cracking in all material conditions, i.e., solution heat treated, solution and aging heat treated, and hot isostatic pressed.
- Cracks seen in the HAZ of the welded material were of two types; those with eutectic products surrounding the cracks and “clean” cracks without any apparent liquation product.
- Liquation cracks were due to the liquation of secondary constituents present in the SLM-manufactured material.
- Total crack lengths in HAZ were highest in the SLM as-built condition and decreased in samples that were solution heat treated before welding. Total crack lengths decreased further in the solution and aged samples and were lowest in hot isostatic pressed samples.
- As all heat treatment in the present study decreased the cracking susceptibility, it is recommended that the SLM material be welded in a heat-treated condition. However, the proper heat treatment must be designed to address fabricability challenges for the specific component at stake.

Author Contributions: Conceptualization, investigation, validation, and writing—original draft preparation, T.R.; Supervision, conceptualization, and editing, J.A. and L-E.S.; Supervision, O.A.O.; Experimental work, K.H. and G.A.

Funding: The authors gratefully acknowledge financial support from the Swedish National Space Board and VINNOVA (National Space Research Program and National Aerospace Research Program).

Acknowledgments: The authors acknowledge the support and input from GKN Aerospace Sweden AB. Special thanks to Abdul Khaliq Khan at the University of Manitoba, Canada for his help with TEM analyses.

Conflicts of Interest: The authors declare no conflict of interest.

References

1. DebRoy, T.; Wei, H.L.; Zuback, J.S.; Mukherjee, T.; Elmer, J.W.; Milewski, J.O.; Beese, A.M.; Wilson-Heid, A.; De, A.; Zhang, W. Additive manufacturing of metallic components – Process, structure and properties. *Prog. Mater. Sci.* **2018**, *92*, 112–224. [CrossRef]
2. Sims, C.T.; Stoloff, N.S.; Hagel, W.C. (Eds.) *Superalloys II*; Wiley-Inter Science: Hoboken, NJ, USA, 1987.

3. Baeslack, W.A.; Nelson, D.E. Morphology of Weld Heat-Affected Zone Liquation in Cast Alloy 718. *Metallography* **1986**, *19*, 371–379. [CrossRef]
4. Radhakrishnan, B.; Thompson, R.G. A phase diagram approach to study liquation cracking in Alloy 718. *Metall. Trans. A* **1991**, *22*, 887–902. [CrossRef]
5. Ahn, Y.; Yoon, B.; Kim, H.; Lee, C. Effect of dilution on the behavior of solidification cracking in PTAW overlay deposit on Ni-base superalloys. *Met. Mater. Int.* **2002**, *8*, 469–477. [CrossRef]
6. DuPont, J.N.; Lippold, J.C.; Kiser, S.D. *Welding Metallurgy and Weldability of Nickel-Base Alloys*; John Wiley and Sons: Hoboken, NJ, USA, 2009.
7. Oshobe, O.E. Fiber laser welding of nickel-based superalloy Inconel 718. Master Thesis, University of Manitoba, Winnipeg, MB, Canada, June 2012.
8. Thompson, R.G.; Radhakrishnan, B.; Mayo, D.E. Intergranular liquid formation, distribution, and cracking in the haz of alloy 718 welds. In Proceedings of the International Symposium on the Metallurgy and Applications of Superalloy 718, Pittsburgh, PA, USA, 12–14 June 1989.
9. Owczarski, W.A.; Duvall, D.S.; Sullivan, C.P. Model for Heat-Affected Zone Cracking in Nickel-Base Superalloys. *Weld J.* **1966**, *45*, 145–155.
10. Lippold, J.C. *Welding Metallurgy and Weldability*; John Wiley and Sons: Hoboken, NJ, USA, 2015.
11. American National Standard Institute. *ANSI Class 2 American Standard: ANSI/MC 96.1. Temperature Measurement Thermocouples*; ANSE: New York, NY, USA, 1982.
12. Donachie, M.J.; Donachie, S.J. *Superalloys: A Technical Guide*, 2nd ed.; ASM International: Materials Park, OH, USA, 2002.
13. Andersson, J.; Jacobsson, J.; Lundin, C. A historical perspective on Vareststraint testing and the importance of testing parameters. In *Cracking Phenomena in Welds IV*; Springer International Publishing: Basel, Switzerland, 2016; pp. 3–23.
14. Thompson, R.G.; Cassimus, J.J.; Mayo, D.E.; Dobbs, J.R. The Relationship between grain size and microfissuring in Alloy 718. *Weld. J.* **1985**, *64*, 91–96.
15. Raza, T.; Andersson, J.; Svensson, L.-E. Vareststraint weldability testing of additive manufactured alloy 718. *Sci. Technol. Weld. Join.* **2018**, *23*, 606–611. [CrossRef]
16. Singh, S.; Andersson, J. Hot cracking in cast alloy 718. *Sci. Technol. Weld. Join.* **2018**, *23*, 568–574. [CrossRef]
17. Huang, X.; Richards, N.L.; Chaturvedi, M.C. Effect of Grain Size on the Weldability of Cast Alloy 718. *Mater. Manuf. Process.* **2004**, *19*, 285–311. [CrossRef]
18. Lingenfelter, A. Welding of Inconel alloy 718: a historical overview. In *Superalloy 718 Metallurgy and Applications*; Loria, E.A., Ed.; The Minerals, Metals and Materials Society: Pittsburgh, PA, USA, 1989; pp. 673–683.
19. Kelly, T.J. Welding Metallurgy of Investment Cast Nickel-based Superalloys. In *Weldability of Materials*; ASM International: Materials Park, OH, USA, 1990; pp. 151–157.
20. Chen, W.; Chaturvedi, M.C.; Richards, N.L. Effect of boron segregation at grain boundaries on heat-affected zone cracking in wrought INCONEL 718. *Metall. Mater. Trans. A* **2001**, *32*, 931–939. [CrossRef]
21. Segerstark, A. Laser Metal Deposition using Alloy 718 Powder: Influence of Process Parameters on Material Characteristics. Ph.D. Thesis, University West, Trollhättan, Sweden, December 2017.
22. Harrison, N.J.; Todd, I.; Mumtaz, K. Reduction of micro-cracking in nickel superalloys processed by selective laser melting: a fundamental alloy design approach. *Acta Mater.* **2015**, *94*, 59–68. [CrossRef]
23. Tillmanna, W.; Schaak, C.; Nellesen, J.; Schaper, M.; Aydınöz, M.E.; Hoyer, K.-P. Hot isostatic pressing of IN718 components manufactured by selective laser melting. *Addit. Manuf.* **2017**, *13*, 93–102. [CrossRef]
24. Withers, P.J.; Bhadeshia, H.K.D.H. Residual stress. Part 2 – Nature and origins. *Mater. Sci. Technol.* **2001**, *17*, 366–375. [CrossRef]
25. Mercelis, P.; Kruth, J.P. Residual stresses in selective laser sintering and selective laser melting. *Rapid Prototyp. J.* **2006**, *12*, 254–265. [CrossRef]

26. ASTM International. *F3301-18. Standard for Additive Manufacturing—Post Processing Methods—Standard Specification for Thermal Post-Processing Metal Parts Made Via Powder Bed Fusion*; ASTM International: West Conshohocken, PA, USA, 2018.



© 2019 by the authors. Licensee MDPI, Basel, Switzerland. This article is an open access article distributed under the terms and conditions of the Creative Commons Attribution (CC BY) license (<http://creativecommons.org/licenses/by/4.0/>).

Paper E

Varestraint Testing of Selective Laser Additive Manufactured Alloy 718 - Influence of Grain Orientation

E

Tahira Raza, Joel Andersson, Lars-Erik Svensson

Published: Metals, 2019, vol. 9, pp. 1113

Printed with permission

Article

Varestraint Testing of Selective Laser Additive Manufactured Alloy 718—Influence of Grain Orientation

Tahira Raza *, Joel Andersson  and Lars-Erik Svensson 

Department of Engineering Science, University West, 461 32 Trollhättan, Sweden; joel.andersson@hv.se (J.A.); lars-erik.svensson@hv.se (L.-E.S.)

* Correspondence: tahira.raza@hv.se; Tel.: +46-520-223-334

Received: 6 September 2019; Accepted: 16 October 2019; Published: 18 October 2019



Abstract: The effect of grain orientation on hot cracking susceptibility of selective laser additive manufactured Alloy 718 was investigated by Varestraint testing. Electron backscattered diffraction showed that cracks in heat affected zone (HAZ) of the welded samples occurred in high angle grain boundaries. The extent of HAZ cracking was smaller in samples tested parallel to the elongated grain orientation and larger in samples transverse to the elongated grain orientation. However, for solidification cracking in the weld metal, no significant difference with respect to grain orientation in the base metal was found.

Keywords: selective laser melting; Alloy 718; grain orientation; Varestraint testing; hot cracking

1. Introduction

During the past decade, significant attention has been drawn to additive manufacturing (AM), which is a unique manufacturing process that allows for parts of various complexity to be built layer-by-layer [1]. Selective Laser Melting (SLM) is a conventional Laser-Powder Bed Fusion (L-PBF) process that involves melting of a thin layer of metallic powder on a substrate plate and then moving a focused laser in a specified pattern along the powder bed. The laser irradiated powder melts forming a micro-sized melt pool. The melt pool rapidly solidifies upon the removal of the laser and individual tracks of solid material forms. The sum of individual tracks within a plane forms a layer. A layer of powder is again applied on the solidified layer and the laser scans the powder to build the next layer. The process is repeated until the part is completed.

Some limitations with the SLM technology are the low rate of production and the limited part size due to the size of building chamber [1]. In order to evade these limitations, parts can be joined by welding technologies such as gas tungsten arc welding and laser beam welding. In this way, SLM manufactured parts can be joined with other SLM parts as well as with conventionally manufactured semi-finished products (i.e. cast and wrought material forms).

In this work, SLM manufactured Alloy 718 is investigated. Alloy 718 is the most widely used iron-nickel based superalloy in aero engines. It is a precipitation hardening superalloy that is commonly used in cast and wrought forms in manufacturing of hot structural components of gas turbine engines. This alloy has a Nb content of ~5 wt.% and is strengthened mainly by γ'' (Ni_3Nb) and slightly by γ' ($\text{Ni}_3(\text{Al}, \text{Ti})$) phases [2]. Interdendritic segregation of Nb is very common in conventionally cast [2], welded [2], and L-PBF manufactured Alloy 718 [3,4], which in turn result in the formation of the brittle Laves phase [$\text{Ni}, \text{Fe}, \text{Cr}_2(\text{Nb}, \text{Mo}, \text{Ti})$]. Other phases occurring in the alloy include δ -phase (Ni_3Nb), and various metal carbides and nitrides, such as NbC, TiC, Cr_{23}C_6 and TiN.

The weldability of Alloy 718 has been extensively studied since the alloy was developed. The main problem when welding this alloy is the hot cracking sensitivity. Many approaches have been used

to determine the hot cracking sensitivity of Alloy 718, one of them is Variable-Restraint (Varestraint) weldability test. Varestraint testing is a method of determining susceptibility to solidification and liquation cracking of the materials. The Varestraint test uses a controlled, externally applied bending strain to produce cracking during actual welding of the alloy. By varying the amount of strain, a threshold strain, i.e. the strain at which cracks start to form and a saturation strain, i.e. the strain at which crack length do not increase any further can be determined. After testing, the total and maximum crack lengths can be measured, usually on the upper surface of the specimen. These crack lengths, and the threshold and saturation strains are essential in determining the weldability of an alloy [5]. The sensitivity to hot cracking in the alloy can be aggravated due to constitutional liquation of carbides, liquation of Laves phase, or the segregation of trace elements like B, P, C or S in the grain boundaries [6–9]. Grain boundary segregation of these trace elements influences the formation and stability of the intergranular liquid that may form during the welding cycle by reducing the melting point of the grain boundary [6].

However, there are no or just a very limited amount of research publications that have investigated the influence of grain orientation on the susceptibility of hot cracking in Alloy 718. Investigations regarding the influence of grain orientation with regard to hot cracking susceptibility have been carried out in other types of alloys. Lippold et al. [10] studied liquation cracking in the partial melted zone (PMZ) of 5083 aluminum alloy plates and found that PMZ cracking was more severe in welds made transverse to the rolling direction in those made parallel to the rolling direction. The authors suggested that in the latter case the elongated grains produced by the rolling process were parallel to the weld, hence, it was more difficult for cracks to propagate into the base metal. Sidhu et al. [11] investigated the HAZ cracking susceptibility in directionally solidified (DS) IN738 alloy, laser welded in longitudinal and transverse directions (with regard to grain orientation). In this way they intersected different numbers of grain boundaries while welding. Their results showed a decrease in HAZ cracking with the reduction in number of high angle grain boundaries that intersected the weld bead. It is known from the literature that the grain boundary energy is inherently high for high angle grain boundaries and impurity atoms often preferentially segregate along these boundaries because of their higher energy state. Guo et al. [12] studied, by Gleeble testing, the correlation between grain boundary characteristics and intergranular liquation in Alloy 718 and reported that liquation mostly occurred at high angle grain boundaries when compared to low angle or special boundaries such as twin boundaries. An issue regarding the SLM manufactured parts, which has been widely investigated by researchers over the past few years, is the relationship between the sample building direction and grain orientation to tensile properties of SLM manufactured parts. Research regarding the influence of building direction on mechanical properties of Alloy 718 disclosed that the strength perpendicular to the building direction was generally higher than parallel to the building direction, while the ductility showed the opposite behavior [3]. In terms of welding of SLM manufactured Alloy 718, hot cracking is a concern, and have previously been investigated by the authors of the present study regarding different heat-treated conditions [4]. In that case, the welding was conducted parallel to the specimen building direction, i.e. parallel to the elongated grain orientation. The results showed that the cracks in HAZ were, to a large extent, following the vertical grain boundaries i.e. parallel to the building direction in the as-built welded samples. In the present study, the influence of grain orientation on hot cracking sensitivity was investigated by welding the specimen in both, parallel and transverse to the elongated grain orientation. Varestraint weldability testing with gas tungsten arc welding was used for conducting the experiments. Microstructures of the welded specimens were studied to understand the sensitivity towards hot cracking.

2. Materials and Methods

The test plates manufactured by the SLM process were 3.4 mm thick with dimensions 50 (width) mm × 100 (length) mm. All samples were manufactured using a powder layer thickness of 40 µm, a beam power of 285 W, a scan line speed of 960 mm/s, and a hatch spacing of 0.11 mm. They were

built in two different directions; vertical and horizontal (Figure 1) and were tested in the as-built condition. The plates had a rough surface and were therefore machined to approximately 3.3 mm of thickness prior to testing. The nominal chemical composition (wt.%) for the gas-atomized (GA) Alloy 718 powder is presented in Table 1.

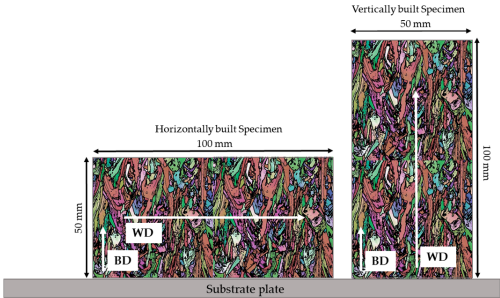


Figure 1. Schematic depicting the geometry and dimensions of the test specimens. Specimen building direction (BD), grain orientation, and welding direction (WD) are also illustrated in the image.

Table 1. Nominal chemical composition of the gas atomized Alloy 718 powder (wt.%).

Element	Ni	Cr	Fe	Nb	Mo	Ti	Al	C
wt.%	50–55	17–21	Bal.	4.75–5.50	2.80–3.30	0.65–1.15	0.20–0.80	<0.08
Element	Mn	Co	Si	Cu	B	Mg	P	S
wt.%	<0.35	<1.0	<0.35	<0.30	<0.006	<0.01	<0.015	<0.0015

The Vastrestraint tests were conducted by making a gas tungsten arc welding with a welding current of 70 A, welding speed of 1.1 mm s^{−1}, and an arc length of 2 mm along the plate and bending the plate at the end of the welding process. Thus, the weld is made as “bead on plate”, with no joint involved. The Vastrestraint test method has been used for many years and details about the equipment can for example be found in [5]. The plates were bent with a stroke rate of 10 mm s^{−1}. The die mandrel radii used were 40, 60, 100, 200 and 300 mm, which led to augmented strains ranging from 0.5 to 4%. The material thickness has been taken into account while calculating the augmented strain for each specimen. Three repetitions were used for each strain level due to data scatter and an average value together with the respective standard deviation was used to express the test results. Total crack length (TCL), the length of all visible cracks in both HAZ and fusion zone (FZ), was used as the criteria for evaluating the cracking susceptibility.

The TCL was measured using a stereomicroscope Olympus-SZX9 (Olympus Corporation, Tokyo, Japan). Cracks were not easily visible due to the oxidation after welding so manual polishing (3-μm diamond suspension) was conducted, followed by electrolytic etching with Oxalic acid. TCL was measured by following the crack path. After measuring the TCL, samples were cut out from the plates for more in-depth microscopic investigations. Samples from weld cross-sections, as well as specimens showing the top surface along the weld, were mounted, ground, polished and electrolytically etched with oxalic acid.

An optical microscope Olympus-BX60M (Olympus Corporation, Tokyo, Japan) was used for microstructural characterization of the welded samples. A Tescan GAIA3 FEG SEM (Scanning electron microscope; Tescan Corporation, Brno, The Czech Republic) with Channel 5 software (Oxford Instruments, Abingdon, UK) was used for the EBSD (Electron back scatter diffraction) analysis.

3. Results and Discussion

3.1. Evolution of Structure and Texture of the Base Metal

The grains in SLM manufactured parts have a dendritic structure and are mainly oriented in the building direction of the part being built (Figure 1). EBSD mapping was used to determine the grain structure and texture of the parts. These maps reveal, inter alia, grain shape and crystallographic texture of the material. Figure 2a is a SEM image of the unetched microstructure showing grain orientation parallel to the building direction (BD). Figure 2b is EBSD inverse pole figure (IPF) coloring mapping of the same image as 2a. The color key representing the crystal orientation and IPF is given on the right side of the Figure 2b. The IPF color map was plotted with regard to Y (BD) direction. Thick black lines represent high angle grain boundaries with $\theta > 15^\circ$ misorientation, while the thin black lines represent low angle grain boundaries ($5\text{--}15^\circ$) misorientation. The microstructure observed in the sample consisted of columnar grain structure with a preferential grain growth in $\langle 001 \rangle$ orientation parallel to the building direction.

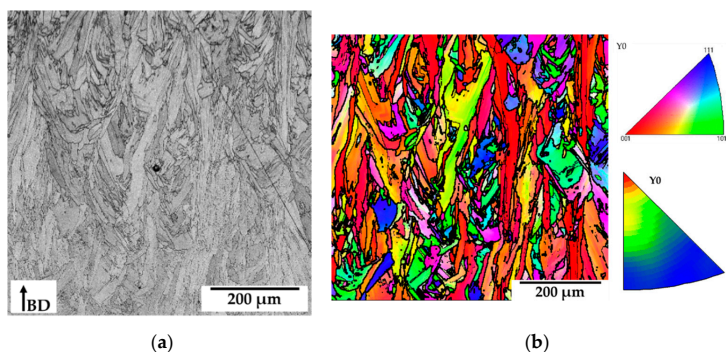


Figure 2. (a) Scanning electron microscope (SEM) micrograph showing the unetched microstructure of the SLM-manufactured Alloy 718 cross section parallel to the building direction (BD). (b) Electron back scatter diffraction (EBSD) inverse pole figure (IPF) colored and grain boundary map of the same image as (a). The color key representing the crystal orientation is given in the upper right corner and IPF in the lower right corner of the image (b).

3.2. Evaluation of Weldability and Microstructural Analysis of Welds

The hot cracking susceptibility of the welds was evaluated by crack measurements on each welded sample after a Varestraint test. The average of total crack length versus augmented strain of the samples welded parallel and transverse to the elongated grain orientation is shown in Figure 3. Figure 3a shows the susceptibility to form hot cracks, both in HAZ and FZ. The magnitude of TCL is larger at higher strain levels (3% and 4% strain) in the specimens welded transverse to the elongated grain orientation. The threshold strain, i.e. the strain to initiate cracking was between 0.8 and 1.6% strain for both types of samples. Although, the saturated strain, i.e. the level of strain above that TCL does not change, could not be found for any type of specimen in the present study. Figure 3b shows solidification cracks occurring in FZ of the samples, while Figure 3c shows the magnitude of liquation cracks occurring in the HAZ. It can be seen from these figures that a significantly higher degree of hot cracking occurred in the samples welded transverse to the elongated grains, as compared to the ones which were welded parallel to the elongated grains (Figure 3a). Cracking in the FZs (Figure 3b) of both types of the samples had no significant differences in amount but in the HAZ (Figure 3c), it was almost twice as much in the samples welded transverse to the elongated grain orientation, compared to the samples welded parallel to the elongated grains.

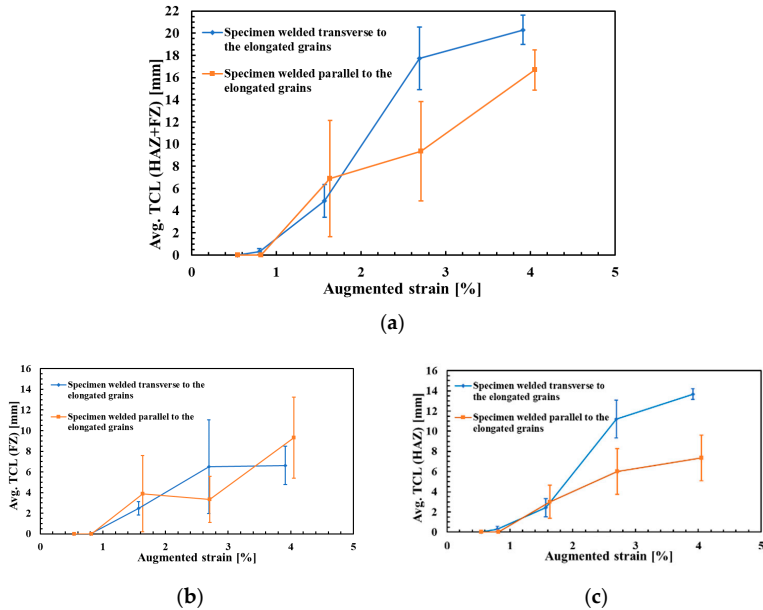


Figure 3. (a) Average of total crack length in both HAZ and FZ, (b) in just FZ, and (c) in just HAZ, versus augmented strain, in specimen welded parallel and transverse to the elongated grains.

Three types of solidification cracks in FZ were observed in this investigation; (i) open cracks exhibiting little or no backfilling, (ii) partially backfilled cracks of moderate size, and (iii) completely backfilled cracks. The crack in Figure 4a is an example of an “open” crack since there is a little or no apparent evidence of backfilling by the eutectic material. Figure 4b is showing a completely backfilled crack and partially backfilled crack.

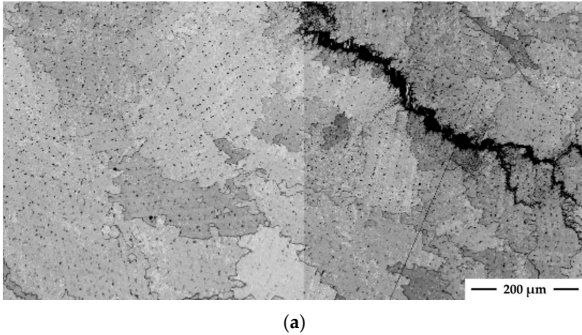
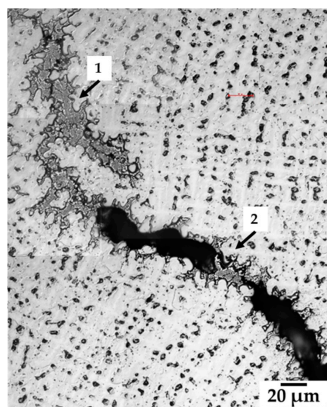


Figure 4. *Cont.*

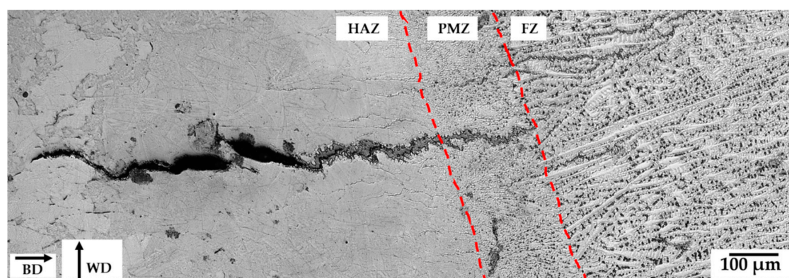


(b)

Figure 4. SEM micrograph showing the unetched microstructure of the fusion zone of the welded sample; (a) showing an “open” crack and (b) showing completely backfilled crack (arrow 1) and partially backfilled crack (arrow 2).

In the present study, all welded specimens exhibited similar cracking morphology in FZ. Cracks in FZ appeared in a roughly semicircular array outlining the location at the trailing edge of the weld pool on the spot where the augmented strain during Vareststraint test was applied. Closer investigation showed that all the FZ cracks were located in the boundaries between individual grains (Figure 4). It is a well-known fact from the welding literature that during solidification the grains at the solid-liquid interface tend to grow in the direction of the maximum temperature gradient [13]. Consequently, cracks propagating in these grain boundaries were oriented perpendicular to the trailing edge of the weld pool.

Most of the cracks in the samples were initiated in the PMZ and were extended away from the fusion line into the HAZ along the grain boundary paths. PMZ is shown in the Figures 5a and 6a with red dashed lines. Some cracks initiated in HAZ too. The EBSD analysis of both specimens demonstrated that crack propagation in PMZ and HAZ always occurred along high angle grain boundaries (Figures 5c and 6c). This cracking behavior was similar in both types of welded samples. According to the literature [12], the high angle grain boundaries are more susceptible to HAZ cracking during welding due to their ability to accommodate a large number of segregated elements, in comparison with low angle grain boundaries, leading to their liquation.



(a)

Figure 5. Cont.

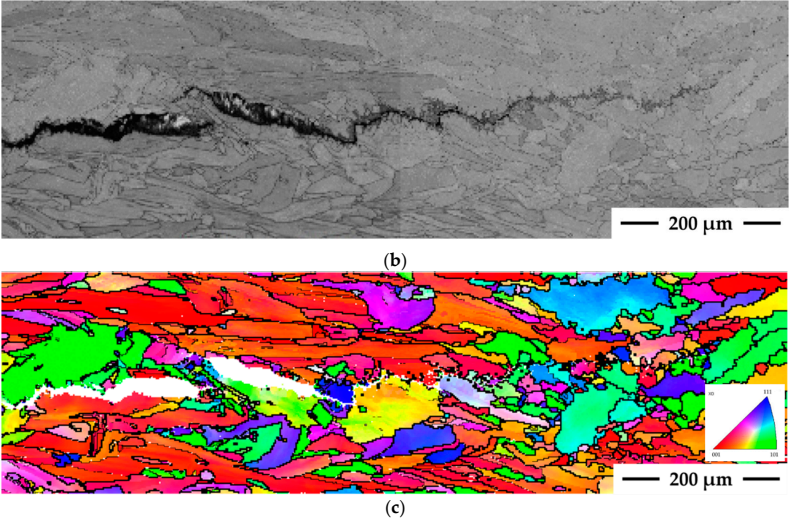


Figure 5. (a) Optical micrograph showing base metal (BM), heat affected zone (HAZ), partially melted zone (PMZ), and fusion zone (FZ) of the specimen welded transverse to the sample building direction (BD) (Note: the welding direction (WD) is transverse to the grain orientation). (b) SEM micrograph showing the unetched microstructure of the welded sample. (c) EBSD inverse pole figure (IPF) coloring mapping of the same image as (b).

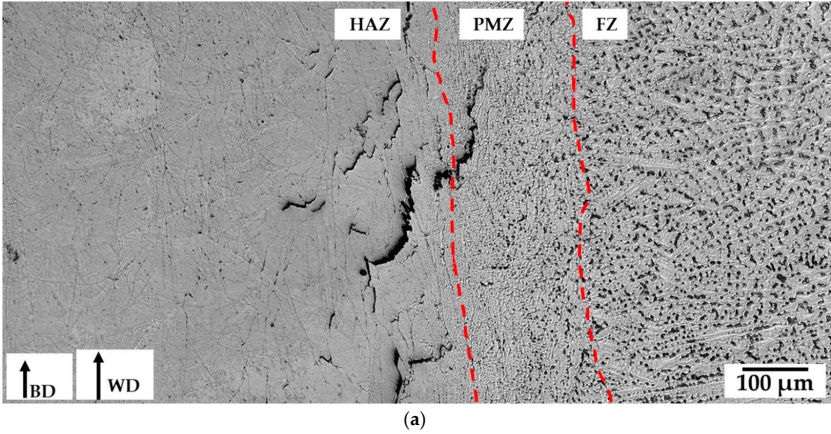


Figure 6. *Cont.*

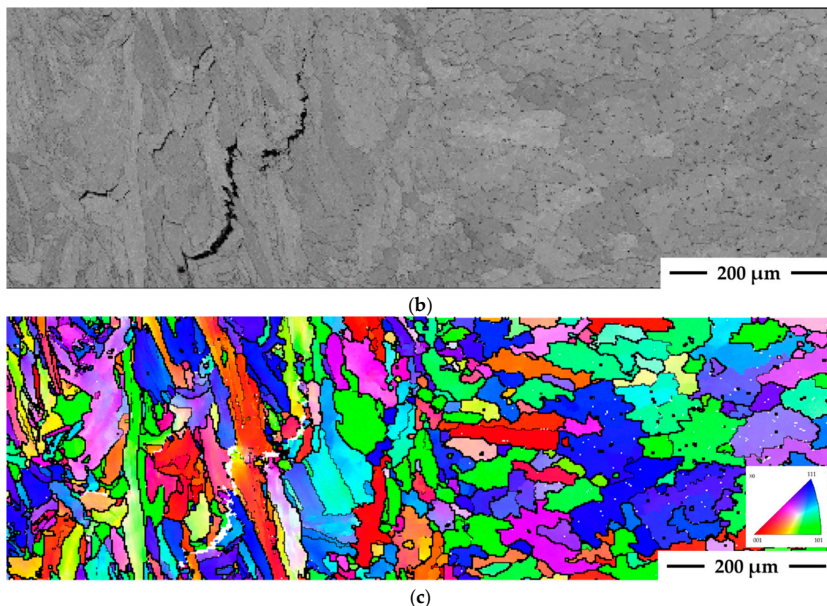


Figure 6. (a) Optical micrograph showing base metal (BM), heat affected zone (HAZ), partially melted zone (PMZ), and fusion zone (FZ) of the specimen welded parallel to the sample building direction (BD) (Note: the welding direction (WD) is parallel to the grain orientation). (b) SEM micrograph showing the unetched microstructure of the welded sample. (c) EBSD inverse pole figure (IPF) coloring mapping of the same image as (b).

Direction of the grains in HAZ was also found to play an important role for the cracking susceptibility of the material. In the sample welded transverse to the grain orientation (Figure 5) the cracks were longer, widely opened and uninterruptedly occurring along the favorably oriented grain boundaries perpendicular to the FZ. On the other hand, the cracks in sample welded parallel to the elongated grain orientation (Figure 6) were observed to run parallel to the fusion line, and they only occasionally extended farther away into the HAZ. The small number of favorably oriented grain boundaries in the HAZ made crack propagation difficult into the HAZ.

Cracks in the present study were caused by the combination of two main factors; mechanically induced strain due to Varestreint test method and a crack susceptible microstructure. It was observed in the welded samples that cracks initiated in the PMZ which is the region adjacent to the fusion line and where the temperatures are sufficiently high to produce melting along the grain boundaries. During re-solidification in this partially melted region liquation of precipitates, residually existed in the SLM as-built microstructure, occurs [4]. This allows the formation of the liquid on the grain boundaries that become susceptible to hot crack formation upon application of the strain during the Varestreint test.

Thus, it is possible to have less HAZ cracking if the SLM-manufactured material is welded parallel to the building direction and along the elongated grain orientation to avoid high angle grain boundaries favorably oriented transversely in the HAZ.

4. Conclusions

Selective laser melted Alloy 718, manufactured in two different building directions, has been investigated by Varestraint weldability testing method in order to understand the influence of grain orientation on hot cracking susceptibility.

- The extent of heat affected zone cracking was observed to be smaller in samples welded parallel to the elongated grain orientation than when welding was done transverse to the elongated grain orientation.
- There was no significant difference relative to the solidification cracking susceptibility in fusion zones of the two orientations.
- EBSD analysis showed that cracking occurred along high angle grain boundaries in both types of samples.

Author Contributions: Conceptualization, investigation, validation and writing—original draft preparation, T.R.; supervision, conceptualization, and editing, J.A. and L.-E.S.

Funding: The authors gratefully acknowledge the financial support from The Swedish National Space Board and VINNOVA (National Space Research Program and National Aerospace Research Program).

Acknowledgments: The authors gratefully acknowledge the financial support from The Swedish National Space Board and VINNOVA (National Space Research Program and National Aerospace Research Program). We also acknowledge GKN Aerospace Filton, United Kingdom for providing us selective laser melted Alloy 718 specimens for the present study. The support and input from GKN Aerospace Sweden AB is also acknowledged. Special thanks to Kjell Hurtig at University West for his help in Varestraint testing and to Nitesh Raj Jaladurgam at Chalmers University of Technology, Sweden for his help in EBSD analysis.

Conflicts of Interest: The authors declare no conflict of interest.

References

1. DebRoy, T.; Wei, H.L.; Zuback, J.S.; Mukherjee, T.; Elmer, J.W.; Milewski, J.O.; Beese, A.M.; Wilson-Heid, A.; De, A.; Zhang, W. Additive manufacturing of metallic components—Process, structure and properties. *Prog. Mater. Sci.* **2018**, *92*, 112–224. [CrossRef]
2. Sims, C.T.; Stoloff, N.S.; Hagel, W.C. *Superalloys II*; Wiley-Inter Science: New York, NY, USA, 1987.
3. Deng, D.; Peng, R.L.; Brodin, H.; Moverare, J. Microstructure and mechanical properties of Inconel 718 produced by selective laser melting: Sample orientation dependence and effects of post heat treatments. *Mater. Sci. Eng. A* **2018**, *713*, 294–306. [CrossRef]
4. Raza, T.; Hurtig, K.; Asala, G.; Andersson, J.; Svensson, L.-E.; Ojo, O.A. Influence of heat treatments on heat affected zone cracking of gas tungsten arc welded additive manufactured alloy 718. *Metals* **2019**, *9*, 881. [CrossRef]
5. Andersson, J.; Jacobsson, J.; Lundin, C. A Historical Perspective on Varestraint Testing and the Importance of Testing Parameters. In *Cracking Phenomena in Welds IV*; Springer International Publishing: Berlin, Germany, 2016; pp. 3–23.
6. Owczarski, W.A.; Duvall, D.S.; Sullivan, C.P. A model for heat affected zone cracking in nickel-base superalloys. *Weld. J.* **1966**, *45*, 145–155.
7. Baeslack, W.A.; Nelson, D.E. Morphology of weld heat-affected zone liquation in cast alloy 718. *Metallography* **1986**, *19*, 371–379. [CrossRef]
8. Kelly, T.J. Elemental effects on cast 718 weldability. *Weld. J.* **1989**, *68*, 44-s.
9. Chen, W.; Chaturvedi, M.C.; Richards, N.L. Effect of boron segregation at grain boundaries on heat-affected zone cracking in wrought INCONEL 718. *Metall. Mater. Trans. A* **2001**, *32*, 931–939. [CrossRef]
10. Lippold, J.C.; Nippes, E.F.; Savage, W.F. An investigation of hot cracking in 5083-O Aluminum alloy weldments. *Weld. J.* **1977**, *56*, 171–178.
11. Sidhu, R.K.; Ojo, O.A.; Chaturvedi, M.C. Weld cracking in directionally solidified Inconel 738 superalloy. *Can. Metall. Q.* **2007**, *46*, 415–424. [CrossRef]

12. Guo, Z.; Chaturvedi, M.C.; Richards, N.L. Effect of nature of grain boundaries on intergranular liquation during weld thermal cycling of nickel base alloy. *Sci. Technol. Weld. Joining* **1998**, *3*, 257–259. [CrossRef]
13. Chalmers, B. Principles of Solidification. In *Applied Solid State Physics*; Springer International Publishing: Berlin, Germany, 1964.



© 2019 by the authors. Licensee MDPI, Basel, Switzerland. This article is an open access article distributed under the terms and conditions of the Creative Commons Attribution (CC BY) license (<http://creativecommons.org/licenses/by/4.0/>).

Tidigare avhandlingar – Produktionsteknik

PEIGANG LI Cold Lap Formation in Gas Metal Arc Welding of Steel An Experimental Study of Micro-lack of Fusion Defects, 2013:2.

NICHOLAS CURRY Design of Thermal Barrier Coatings, 2014:3.

JEROEN DE BACKER Feedback Control of Robotic Friction Stir Welding, 2014:4.

MOHIT KUMAR GUPTA Design of Thermal Barrier Coatings A modelling approach, 2014:5.

PER LINDSTRÖM Improved CWM Platform for Modelling Welding Procedures and their Effects on Structural Behavior, 2015:6.

ERIK ÅSTRAND A Framework for Optimised Welding of Fatigue Loaded Structures Applied to Gas Metal Arc Welding of Fillet Welds, 2016:7.

EMILE GLORIEUX Multi-Robot Motion Planning Optimisation for Handling Sheet Metal Parts, 2017:10.

EBRAHIM HARATI Improving fatigue properties of welded high strength steels, 2017:11.

ANDREAS SEGERSTARK Laser Metal Deposition using Alloy 718 Powder Influence of Process Parameters on Material Characteristics, 2017:12.

ANA ESTHER BONILLA HERNÁNDEZ On Cutting Tool Resource Management, 2018:16.

SATYAPAL MAHADE Functional Performance of Gadolinium Zirconate/YSZ Multi-layered Thermal Barrier Coatings, 2018:18.

ASHISH GANVIR Design of suspension plasma sprayed thermal barrier coatings, 2018:20.

AMIR PARSIAN Regenerative Chatter Vibrations in Indexable Drills: Modeling and Simulation, 2018:21.

ESMAEIL SADEGHIMERESHT High Temperature Corrosion of Ni-based Coatings, 2018:23.

VAHID HOSSEINI Super Duplex Stainless Steels. Microstructure and Properties of Physically Simulated Base and Weld Metal, 2018:24.

MORGAN NILSEN Monitoring and control of laser beam butt joint welding, 2019:27.

ARBAB REHAN Effect of heat treatment on microstructure and mechanical properties of a 5 wt.% Cr cold work tool steel, 2019:28.

KARL FAHLSTRÖM Laser welding of ultra-high strength steel and a cast magnesium alloy for light-weight design, 2019:29.

EDVARD SVENMAN An inductive gap measurement method for square butt joints, 2019:30.

NAGESWARAN TAMIL ALAGAN Enhanced heat transfer and tool wear in high-pressure coolant assisted turning of alloy 718, 2019:31.

ADNAN AGIC [Forthcoming], Edge Geometry Effects on Entry Phase by Forces and Vibrations, 2020:32.

ANA CATARINA FERREIRA MAGALHÃES [Forthcoming], Thermoelectric Measurements for Temperature Control of Robotic Friction Stir Welding, 2020:33

ASHWIN DEVOTTA [Forthcoming], 2020:34

Process Understanding and Weldability of Laser-Powder Bed Fusion Manufactured Alloy 718

Laser-powder bed fusion (L-PBF) is an additive manufacturing (AM) process that builds components by fusing fine metal powders using laser. Production of near-net-shape objects is possible with L-PBF, however it is not an issue-free process and parts produced can face high amount of residual stresses, cracking, porosities and lack of fusion defects. The quality of the final part is highly dependent on the process parameters and there is no universal set of parameters that can yield optimum results for all the different materials, geometries and L-PBF machines. Therefore, investigation regarding the influence of different process parameters on the specific material was performed in the present research.

Another matter that can be of importance with L-PBF-manufactured parts is that the size of the L-PBF-manufactured objects is often quite limited due to the nature of the process and size of the production chamber. Since welding is the most important joining technique for metallic materials, the investigation of welding regarding L-PBF-manufactured materials has become an important issue to study. The microstructure of L-PBF-manufactured superalloy 718, which was the material investigated in this research, contains precipitating elements that can make the material sensitive to hot cracking in heat affected zone during welding. Therefore, the alloy in the present study was heat treated in various ways to study the effect of heat treatments on the microstructure and further on the weldability of the material. The L-PBF-manufactured Alloy 718 was then compared to wrought Alloy 718 which is the material extensively used in aerospace industry nowadays.



Tahira Raza

Obtained her B.Sc. degree in Industrial Engineering and Management in 2012 and earned her M.Sc. degree in Manufacturing Engineering in 2013, at University West. She then worked two years at University West as a research engineer and started her PhD studies in 2015. Her research interest includes additive manufacturing, welding and weldability testing, heat treatments and material characterization.